Doctoral Thesis

Influence of various auxiliary activators on CaO-activated cementless binder

Woo Sung Yum

Department of Urban and Environmental Engineering
(Urban Infrastructure Engineering)

Graduate School of UNIST

2019

Influence of various auxiliary activators on CaO-activated cementless binder

Woo Sung Yum

Department of Urban and Environmental Engineering
(Urban Infrastructure Engineering)

Graduate School of UNIST

Influence of various auxiliary activators on CaO-activated cementless binder

A thesis/dissertation
submitted to the Graduate School of UNIST
in partial fulfillment of the
requirements for the degree of
Doctor of Philosophy

Woo Sung Yum

11. 21. 2018
Approved by

_____

Advisor
Jae Eun Oh

Influence of various auxiliary activators on CaO-activated cementless binder

Woo Sung Yum

This certifies that the dissertation of Woo Sung Yum is approved.

11. 21. 2018.

Jae Eun Oh
Associate Professor of Urban and Environmental Engineering
Ulsan National Institute of Science and Technology
Committee Chairperson

Myoungsu Shin
Associate Professor of Urban and Environmental Engineering
Ulsan National Institute of Science and Technology
Committee Member

Seyoon Yoon
Associate Professor of Civil Engineering
Kyonggi University at Suwon
Committee Member

Sungchul Bae
Associate Professor of Architectural Engineering
Hanyang University at Seoul
Committee Member

Juhyuk Moon
Associate Professor of Civil and Environmental Engineering
Seoul National University
Committee Member

ABSTRACT

Influence of various auxiliary activators on
CaO-activated cementless binder

by

Woo Sung Yum

Doctor of Philosophy in Engineering

Ulsan National Institute of Science and Technology

Portland cement is the most commonly used construction material in the world, but it is being regarded as a major cause of global warming due to the carbon dioxide generation during the production process. Therefore, in this study, eco-friendly cementless binder was developed to replace Portland cement. The developed cementless binders are based on the ground granulated blast furnace slag (GGBFS) and fly ash, which are industrial byproduct, and CaO is used as the main activator.

The CaO-activator has various advantages compared to the conventional alkali-activators (i.e., NaOH, KOH, and Na-silicate), but it has problems such as low early compressive strength and variation of physical properties depending on the source of raw materials. Therefore, in this study, various types of auxiliary activators were applied to CaO-activator and four different cementless binders were developed. To verify the mechanical properties and microstructural characteristics of the developed binders, X-ray fluorescence spectroscopy, X-ray diffraction, compressive strength, thermogravimetric, mercury intrusion porosimetry, isothermal calorimetry, pH meter, electrical resistivity measurement, and scanning electron microscopy with energy dispersive spectroscopy analysis were performed.

To investigate the effect of $CaCl_2$ on CaO-activated GGBFS/fly ash binder, various amounts of $CaCl_2$ were incorporated. The samples with $CaCl_2$ generated much higher compressive strength than the sample without $CaCl_2$ at all curing period. In terms of compressive strength, substitution of 2wt% $CaCl_2$ was considered to be the best mixture proportion. Interestingly, despite having no cement compound in this binder, $CaCl_2$ had a very similar acceleration effect on the cementless binder.

The reactions of binders generated significantly lower cumulative heats up to 72 h, although their initial heats up to 10 h were notably higher, compared to the cumulative and initial heats of Portland cement hydration. These high initial heats of binder might be advantageous in activating raw materials.

XRD and TG/DTG results showed that the amorphous phase of the raw material was dissolved more by the addition of $CaCl_2$, and which seemed to generate more quantity of reaction product, resulting in the denser cementitious matrix. The most distinct mineralogical changes due to $CaCl_2$ addition were the formation of hydrocalumite and the removal of hydrotalcite and strätlingite.

From MIP results, the addition of $CaCl_2$ induced pore-size refinement effect from the early stage of curing. In addition overall total porosity was reduced as more amount of $CaCl_2$ substituted, resulting in higher early and final compressive strength.

In the BSE images, the particle size of raw materials became smaller as $CaCl_2$ was replaced, which seems to be due to the $CaCl_2$ dissolving raw materials actively. As a result of EDS analysis, much higher Ca/Al and Na/Al ratios were measured as $CaCl_2$ was added, which indicates that Ca and Na ions were produced more by dissolving the raw materials.

As mentioned earlier, $CaCl_2$ is used as an accelerator in Portland cement. However, the used of $CaCl_2$ can cause the steel corrosion, ACI regulated the maximum dosage of $CaCl_2$ varying with the structures. Therefore, in this study, the electrical resistivity of the binder was measured using four Wenner method to verify the possibility of steel corrosion. The higher electrical resistivity was measured as $CaCl_2$ was added, which indicates that the possibility of corrosion of the steel bar is low even with the addition of $CaCl_2$. The reason for this result seems to be that a denser matrix was generated as $CaCl_2$ was added.

When $CaCl_2$ was applied to CaO-activated GGBFS/fly ash binder, satisfactory levels of mechanical properties were measured, but further experiment is required for commercialization due to concerns about steel corrosion. Therefore, other types of accelerator such as $Ca(NO_3)_2$ and $NaNO_3$ was applied to CaO- activated GGBFS binder.

In the compressive strength, the addition of each nitrate salt ($Ca(NO_3)_2$ and $NaNO_3$) was clearly beneficial in developing strength during the early days of curing. The results showed that on day 3 of curing, the strengths were almost doubled for all samples, regardless of the cation type of the nitrate salts. However, a difference between the nitrate salts was seen on day 28 of curing, where the added

$Ca(NO_3)_2$ was still effective in increasing the cementless binder's strength compared to the control (without any nitrate salts), the added $NaNO_3$ was not anymore.

A pH meter measurement was conducted to verify the cation effect of each nitrate salts. In the presence of $NaNO_3$, which generally increases the solubility of $Ca(OH)_2$ in aqueous salt solutions, the higher pH of $NaNO_3$ containing samples was obtained due to the increased amount of dissolving the $Ca(OH)_2$. These higher pH seems to generate more reaction products and higher early strength measurements. In the samples with $Ca(NO_3)_2$, an additional supply Ca ion from $Ca(NO_3)_2$ resulted in a common ion effect, which seems to have a relatively low pH measured by lowering the solubility of $Ca(OH)_2$. Although a lower pH was measured, higher compressive strength seem to be measured due to the supply of stable Ca ions.

The type of reaction products analyzed with the XRD was very similar between the $Ca(NO_3)_2$ and $NaNO_3$ group when the same weight of salts was used, although their compressive strength were significantly different. C-S-H and akermanite were identified in all samples. An Al_2O_3-Fe_2O_3-mono (AFm) phase was clearly identified in the samples containing any type of nitrate salts with more than 3wt%. This seemed to occur mainly when the quantity of salts was at 5wt%, causing the XRD peaks of this phase to increase significantly. AFm phase in our study was NO_3 AFm or NO_2 AFm or a mixture of NO_3-and NO_2 AFm phases. In the samples with $Ca(NO_3)_2$, weaker peaks of portlandite were identified and portlandite was not identified in the 3wt% $Ca(NO_3)_2$ and 5wt% $Ca(NO_3)_2$ samples. However, portlandite was clearly identified in the samples with $NaNO_3$.

The more amount of nitrate salts were substituted, the more total weight loss until 1,000C occurred. This weight loss indirectly suggests that more nitrates salts resulted in more GGBFS due to an increase of it dissolving. Overall TG results were consistent with XRD results. At 3 days of curing, the use of nitrate salts was clearly beneficial to produce C-S-H, regardless of the cation type in the salts. However, at 28 days of curing, the samples with $NaNO_3$ clearly displayed a reduction of C-S-H when weight of the salt increased. The NO_3-and/or NO_2-AFm phase were significantly generated when nitrate salts replaced 3-5wt% of the total mixture.

The pore size distribution was significantly dependent on the cation type of nitrate salts. The shape of the distribution curves of the samples with $Ca(NO_3)_2$ were roughly grouped in two curve shapes depending on the quantity of $Ca(NO_3)_2$, while those of the $NaNO_3$ samples were not significantly changed by the dosage of $NaNO_3$.

In order to develop a cementless binder with satisfactory mechanical properties without concern about steel corrosion, calcium formate ($Ca(HCOO_2)$ was applied as an auxiliary activator to CaO-activated GGBFS binder and its effect was verified using various experiments.

The addition of $Ca(HCOO_2)$, such as $CaCl_2$, $Ca(NO_3)_2$, and $NaNO_3$, acted as an accelerator and 1.3-2 times higher compressive strength was measured at 3 days of curing and 1.1-1.4 times higher compressive strength measured at 28 days of curing compared to samples without $Ca(HCOO_2)$. The extent of $Ca(HCOO_2)$`s strength enhancement was comparable to that of samples with $CaCl_2$. The highest compressive strength was achieved at 3wt% of $Ca(HCOO_2)$.

As a result of MIP measurement, the pore-size refinement effect occurred as $Ca(HCOO_2)$ was replaced, and which seemed to be the main reason of increasing the compressive strength of the binder. Interestingly, in all other samples except samples with 3wt% $Ca(HCOO_2)$, a greater amount of total porosity was measured at 28 days compared to 3 days, suggesting the possibility of nanometer-sized pores. However, all samples with $Ca(HCOO_2)$ did not show any strength reduction during curing days, the influential degree of the pore formation on the strength seemed not to be significant in this study.

The XRD patterns of samples can be divided into two groups; samples with 0-1wt% $Ca(HCOO_2)$ demonstrated relatively strong peaks of $Ca(OH)_2$ without C_2AH_8, while samples with 3-5wt% CF showed strength C_2AH_8 peaks but no $Ca(OH)_2$. This suggests that at least more than 3wt% of $Ca(HCOO_2)$ is necessary to significantly change the types of reaction products for the CaO-activated GGBFS system. C_2AH_8 is one of main reaction products of calcium alumina cement, and it is strength-contribution phase. As a greater quantity of $Ca(HCOO_2)$ was substituted, a greater amount of C_2AH_8 was produced, the presence of $Ca(HCOO_2)$ was likely the main cause of the C_2AH_8 generation. Thus, the formation of C_2AH_8 might have contributed to the enhanced strength. However, it is well known that C_2AH_8 is a metastable phase that can easily converted over time, and this conversion accompanies a significantly increase in porosity that results in strength reduction. In this study, the intensities of C_2AH_8 peaks also decreased at 28 days, compared to 3 days, and thus a portion of C_2AH_8 was removed.

In the TG/DTG results, as the $Ca(HCOO_2)$ wt% and curing days increased, the more mass reduction was observed. This indicates that more reaction products were generated and more weight of GGBFS was dissolved because GGBFS was the only source of Si and Al in the formation of the reaction products (e.g., C-S-H, C_2AH_8). The second peaks of C_2AH_8 at ~200°C showed that more amount of $Ca(HCOO_2)$ replacement generated more amount of C_2AH_8. The DTG peaks of AH gel significantly grew in 1 and 5wt% contained samples from 3 days to 28 days, while those in 3wt% contained sample barely increased. The formation of AH gel generally increases porosity and reduces strength in calcium alumina cement, the trend of AH gel formation in the TG results also seems to be in agreement with the testing results of strength and porosity in this study.

TABLE OF CONTENTS

ABSTRACT I
TABLE OF CONTENTS V
LIST OF FIGURES VII
LIST OF TABLES IX
LIST OF ABBREVIATIONS X
CEMENT CHEMISTRY NOTATIONS XI
1.INTRODUCTION 1
1.1. Global warming and problems of cement use 1
1.2. Alternative materials for Portland cement 3
1.2.1. Low carbon cement 3
1.2.2. Geopolymer 4
1.2.3. Alkali-activated GGBFS 4
1.2.4. Ca-based activation 4
1.3. Outline of Dissetation 5
2. EXPERIMENTAL TECHNIQUES AND BACKGROUND 7
2.1. Laser diffraction particle size analyzer 7
2.2. X-ray fluorescence 7
2.3. Hydration stop methods 8
2.4. X-ray diffraction 9
2.5. Thermalgravimetric analysis 10
2.6. Mercury intrusion porosimetry 11
2.7. Scanning electron microscopy 12
2.8. Isothermal calorimetry 13
2.9. Measurement of pH 14
2.10. Electrical resistivity of cementitious material 15
3. EFFECTS OF CALCIUM CHLORIDE ON HYDRATION AND PROPERTIES OF CAO-ACTIVATED GGBFS/FLY ASH BINDER 17
3.1. Introduction 17
3.2. Experiment 18
3.3. Results and discussion 23
3.3.1. Compressive strength tests 23
3.3.2 Heat of reaction 25

3.3.3 XRD 27
3.3.4 TG 29
3.3.5 MIP 33
3.3.6 Scanning electron microscopy 36
3.3.7 Electrical resistivity of prismatic mortar samples of CAS 4:4:2 39
3.3.8 Further discussion 41
3.4. Chapter summary 41
4. INFLUENCE OF CALCIUM AND SODIUM NITRATE ON THE STRENGTH AND REACTION PRODUCTS OF THE CAO-ACTIVATED GGBFS SYSTEM 43
4.1. Introduction 43
4.2. Experimental procedure 44
4.3. Results and discussion 47
4.3.1. Compressive strength 47
4.3.2. Measurement results of the pH levels 49
4.3.3. XRD analysis 50
4.3.4. TG/DTG 53
4.3.5. MIP 56
4.4. Chapter summary 58
5. STRENGTH ENHANCEMENT OF CAO-ACTIVATED GGBFS BINDER THROUGH ADDITION OF CALCIUM FORMATE AS A NEW AUXILIARY ACTIVATOR 60
5.1. Introduction 60
5.2. Experimental procedures 61
5.3. Results and discussions 64
5.3.1. Compressive strength 64
5.3.2. Mercury intrusion porosimetry (MIP) 64
5.3.3. X-ray diffraction (XRD) 67
5.3.4. Thermogravimetry (TG) 69
5.4. Chapter summary 75
6. SUMMARY 76
REFERENCES 80

LIST OF FIGURES

Figure 1.1 Globally averaged sea level change 1
Figure 1.2 Globally averaged greenhouse gas concentrations 1
Figure 1.3 World portland cement production 1990-2050 2
Figure 2.1 Procedure of laser diffraction particel size analyer 7
Figure 2.2 XRF mesurement process 8
Figure 2.3 Diagram of Bragg`s law 10
Figure 2.4 Schematic of scanning electron microscope 13
Figure 2.5 Schematic of isothermal conductivity method 14
Figure 2.6 Photo of pH meter experiment 15
Figure 2.7 Schematic of electric resistivity measurement 16
Figure 3.1 Particle size distributions of raw materials 19
Figure 3.2 XRD patterns of mixed raw material, fly ash, and GGBFS. The numbers in parentheses are ICDD PDF-2 or ICSD data numbers for identified phases. 20
Figure 3.3 Measuring electrical resistivity of the mortar samples (sand-to-binder ratio = 1:3 at w/b = 0.5): (a) prismatic sample and (b) front and back views of the prismatic sample. 23
Figure 3.4 Compressive strength testing results of CAS 4:4:2 binders: (a) w/b = 0.3, (b) w/b = 0.35, and (c) w/b = 0.4. 25
Figure 3.5 Isothermal conduction calorimetry curves over 72 h: (a) heat evolution rate and (b) cumulative curves. 26
Figure 3.6 XRD patterns of hardened paste samples of CAS 4:4:2 binders (Groups 1 and 3) at 3 and 28 days: (a) 0CSF, (b) 1CSF, (c) 2CSF, and (d) 3CSF. The numbers in parentheses are ICDD PDF-2 or ICSD data numbers for identified phases. 28
Figure 3.7 Overlaid XRD patterns of mixed raw material (GGBFS + fly ash) and hardened samples with w/b = 0.40 at 2θ = ~22-37° (a) at 3 days and (b) at 28 days. 29
Figure 3.8 TG and DTG curves of hardened pastes of CAS 4:4:2 mixture samples with different w/b values (i.e., w/b = 0.30 and 0.40, Groups 1 and 3, respectively) and curing days (i.e., 3 and 28 days): (a) 0CSF, (b) 1CSF, (c) 2CSF, and (d) 3CSF. 32
Figure 3.9 Pore-size distributions and total porosities of hardened pastes of CAS 4:4:2 binders: (a) w/b = 0.30 at 3 days, (b) w/b = 0.30 at 28 days, (c) w/b = 0.40 at 3 days, and (d) w/b = 0.40 at 28 days... 36
Figure 3.10 Back-scattered electron images of (a) 0CSF, (b) 1CSF, (c) 2CSF, and (d) 3CSF at w/b = 0.30 at 28 days. The solid circles indicate the locations of EDS spot analysis. 38
Figure 3.11 Electrical resistivity of hardened mortar samples of the CAS 4:4:2 mixture on (a) plane 1 and (b) plane 2. 40

Figure 4.1 Particle size distribution of GGBFS. 44
Figure 4.2 XRD pattern of GGBFS..... 45
Figure 4.3 Compressive strength analysis of various binder mixtures with $Ca(NO_3)_2$ and $NaNO_3$ additions. (a) Represents the $Ca(NO_3)_2$ (CN) group against the control one. (b) Represents the $NaNO_3$ (SN) group against the control one. 48
Figure 4.4 The change of pH of diluted paste samples during the first 3 days. 49
Figure 4.5 XRD patterns of hardened samples. The investigated samples were as follows: (a) the CN group on day 3, (b) the CN group on day 28, (c) the SN group on day 3, and (d) the SN group on day 28. The numbers in brackets indicate the reference numbers of identified phases in the ICDD PDF-2 database. Note that the reference pattern of C-S-H was obtained from [95] after removing the reflections of calcium hydroxide. 52
Figure 4.6 TG/DTG results of hardened samples during various curing days. The following conditions were investigated: (a) the CN group on day 3, (b) the CN group on day 28, (c) the SN group at day 3, and (d) the SN group that shows an enlarged window of the 0–350°C range on day 28..... 56
Figure 4.7 The MIP results of hardened during various curing days. The following conditions were investigated: (a) the CN group on day 3, (b) the CN group on day 28, (c) the SN group on day 3, and (d) the SN group on day 28. 58
Figure 5.1 Particle distribution of GGBFS..... 61
Figure 5.2 XRD pattern of GGBFS..... 62
Figure 5.3 Compressive strength results of the hardened paste samples. 64
Figure 5.4 Pore-size distributions of hardened samples: (a) at 3 days and (b) at 28 days. 66
Figure 5.5 XRD patterns of hardened samples: (a) at 3 days and (b) at 28 days. 69
Figure 5.6 TG/DTG results of hardened samples: (a) 3 days; (b) enlarged view of figure (a) up to 400°C; (c) 28 days; and (d) enlarged view of figure (c) up to 400°C. 72
Figure 5.7 Temporal change of AH gel in DTG from 3 days to 28 days: (a) 1CFCS; (b) 3CFCS; and (c) 5CFCS..... 74

LIST OF TABLES

Table 1.1 Major composition of CSA.....3
Table 2.1 Temperature ranges of the reaction products for TG,DTA, and DSC……11
Table 3.1 Chemical composition of raw materials……..18
Table 3.2 Mixutre proportions (wt%)……21
Table 3.3 Reference temperature ranges of weight loss in TG……33
Table 3.4 Averagere atomic ratios of raw materials from XRF and those from EDS results from the locations in **Figure 3.10**……..38
Table 4.1 Chemical oxide composistion of GGBFS……..……45
Table 4.2 The mixture proportions and replacement percentage of each additional chemical of the paste samples (wt%)……....46
Table 4.3 Total porosity and average pore size of hardened samples……..57
Table 5.1 Chemical composition of GGBFS……..62
Table 5.2 Mixture proportions (wt%)……63
Table 5.3 Total porosities and average pore diameters of hardened samples……..65

LIST OF ABBREVIATIONS

AAS	Alkali-Activated GGBFS
ACI	American Concrete Institute
ASTM	American Society for Testing and Materials
BSE	Backscattered Electrons
CAC	Calcium Aluminate Cement
CAS	CaO-activated GGBFS
COD	Crystallography Open Database
CSA cement	Calcium Sulfoaluminate Cement
DSC	Differential Scanning Calorimetry
DTA	Differential Thermal Analysis
DTG	Derivative of Thermalgravimetric Analysis
EDS	Energy Dispersive Spectroscopy
GGBFS	Ground Granulated Blast Furnace Slag
ICDD	International Center for Diffraction Data
ICSD	Inorganic Crystal Structure Database
IPA	Isopropyl Alcohol
KS	Korean Standard Association
LOI	Loss of Ignition
MIP	Mercury Intrusion Porosimetry
OPC	Ordinary Portland Cement
SCMs	Supplementary Cementitious Materials
SE	Secondary Electron Microscopy
The IPCC	The intergovernmental Panel on Climate Change
XRD	X-ray Diffraction
XRF	X-ray Fluorescence

CEMENT CHEMISTRY NOTATIONS

A	Al_2O_3
C	CaO
C_3A	$3CaO \cdot Al_2O_3$
C_3S	$3CaO \cdot SiO_2$
C_2S	$2CaO \cdot SiO_2$
F	Fe_2O_3
S	SiO_2
$\bar{S}$	SO_3
AFm	Al_2O_3-Fe_2O_3-mono
AFt	Al_2O_3-Fe_2O_3-tri
C-S-H	Calcium silicate hydroxide

1. INTRODUCTION

1.1. Global warming and problems of cement use

As global warming accelerates, the annual average temperature and sea level increase year by year (See **Figure 1.1**), and abnormal climate conditions are being seen all over the world. In Korea, due to the unusual climate caused by global warming, there are usually tropical nights and heavy rains in summer and long - term cold in winter.

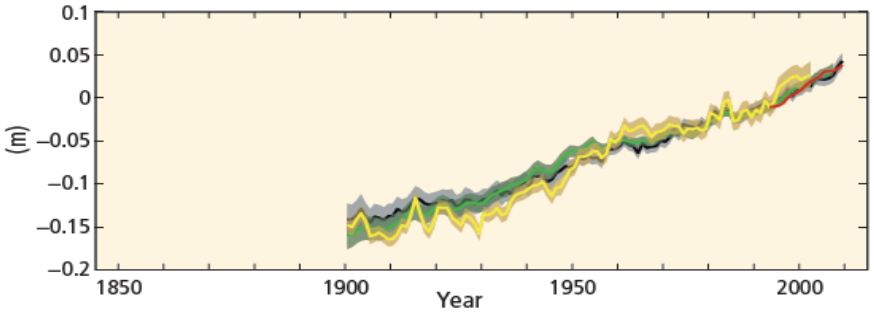

Figure 1.1 Globally averaged sea level change [2]

Global warming is caused by the emission of greenhouse gases. As annual greenhouse gas emissions are increasing every year (see **Figure 1.2)**, and global warming is rapidly accelerating. There are six types of greenhouse gas (i.e., carbon dioxide (CO_2), methane (CH_4), nitrous oxide (N_2O), carbon tetrachloride (CCl_4), chlorofluorocarbon (CFC), perfluorocarbon (PFCs), Sulphur hexafluoride (SF_6)) and emission of these gases causes global warming. Among these six types of greenhouse gas, carbon dioxide is pointed out as a major cause of global warming [3]. In order to reduce greenhouse gases, the leaders of each country are making efforts to reduce greenhouse gas emissions and prevent global warming through various agreements (e.g., The Kyoto protocol and Paris agreement), but a fundamental solution is needed.

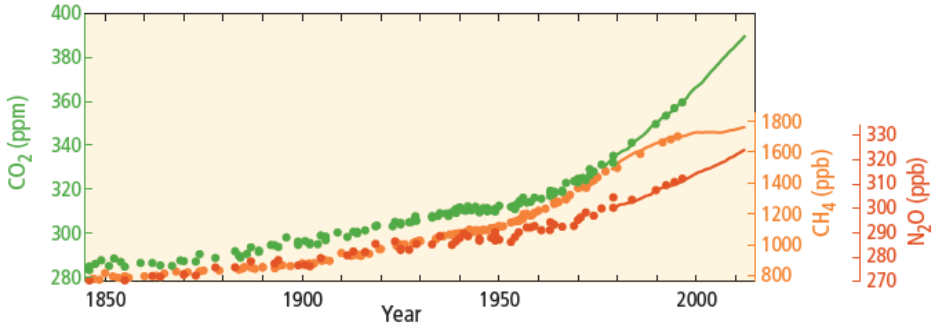

Figure 1.2 Globally averaged greenhouse gas concentrations [2]

Meanwhile, Portland cement is the most widely used construction material in the world and produces approximately 3 billion tons of Portland cement each year [1]. Portland cement is used in residential facilities, social infrastructure, and skyscrapers because it is the cheapest material among the construction materials, has excellent water resistance, and can be manufactured in any shape or size [4]. However, Portland cement is also a major cause of global warming. Researchers are thus trying to develop replacements. Considering that 0.9 tons of carbon dioxide are generated when producing one ton of cement, the amount of carbon dioxide generated by the cement industry is closely related to global warming. In addition, the Portland cement industry is accountable for approximately 7% of CO_2 emissions by worldwide, which is a significant amount of CO_2 emission from a single industry [5]. As shown in **Figure 1.3**, annual Portland cement production is expected to increase more, and the amount of carbon dioxide generated by the cement industry will increase further. Therefore, reducing the use of Portland cement and developing a material that can replace it is a way to reduce carbon dioxide emissions and prevent global warming.

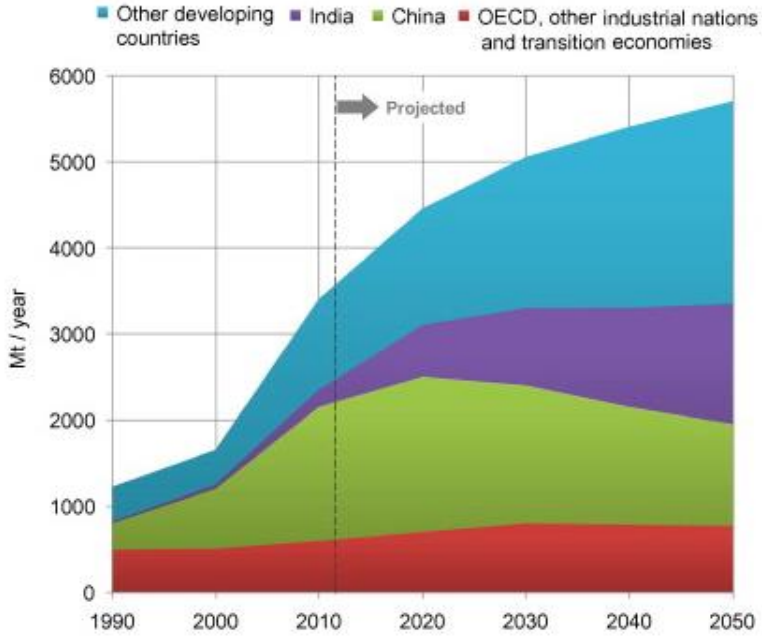

Figure 1.3 World portland cement production 1990-2050 [1]

1.2. Alternative materials for Portland cement

Many researchers are developing alternatives to replace Portland cement. Although various replacement materials have been developed, there are currently only three viable candidates. “Low carbon cement, geopolymer, and alkali-activated slag; each of which will be now be discussed in turn”

1.2.1 Low carbon cement

A typical low-carbon cement is calcium sulfoaluminate cement (CSA cement), which was developed in China [6]. CSA cement has the advantages of rapid strength development, rapid setting, and shrinkage compensation, and is used for bridges, airport runways, and concrete road-repair. [7] CSA cement has already been commercialized and used in China, but it is only used as a shrinkage-compensate in other countries. The main components of CSA cement are shown **Table 1.1** Its major component is Ye`elimite and the minor components are C_2S, C_3A, $C_5S_2\overline{S}$, C_4AF and C_2AS [8].

Table 1.1 Major composition of CSA

Phase	Cement notation	Chemical formula
Ye`elimite	$C_4A_3\overline{S}$	$Ca_4(AlO_2)_6SO_4$
Belite	C_2S	Ca_2SiO_4
Tricalcium aluminate	C_3A	$Ca_3Al_2O_6$
Ternesite	$C_5S_2\overline{S}$	$Ca_5(SiO_4)_2SO_4$
Al-rich ferrite	C_4AF	$Ca_2(Al,Fe)_2O_5$
Gehlenite	C_2AS	$Ca_2Al(AlSiO_7)$

Depending on the composition ratio of these components, they are classified into calcium-sulfoaluminate-belite cement (CSAB cement) [9], belite-rich cement and belite calcium-sulfoaluminate-ternesite cement [10]. The major reaction products of CSA cement are C-S-H and ettringite. The formation of ettringite plays an important role in the strength development of CSA cement. In Portland cement, ettringite is converted to monosulfate and AFm phases during the curing period, but in CSA cement, ettringite remains in a stable without conversion. CSA cement generates much less carbon dioxide than Portland cement and is therefore considered low carbon cement. In terms of raw materials, CSA cement produces less carbon dioxide because it consumes less calcium carbonate than Portland cement. In addition, in the case of Portland cement, the calcining temperature is about 1,450°C, but the calcining temperature of CSA cement is 1,250°C, so much less heat energy is required [11, 12]. Furthermore, less grinding energy is needed for CSA clinker because it is softer than that of Portland cement clinker.

1.2.2. Geopolymer

Another type of alternative cement material is geopolymer. The reason why the geopolymer is attracting attention as an alternative cement material is that geopolymer does not generate carbon dioxide because it does not have a calcination process. Jeseph Davidovits [13] estimated that geopolymer produces about 40% to 90% less carbon dioxide than Portland cement, and that if the geopolymer replaces Portland cement, a vast amount of carbon dioxide can be reduced. Geopolymer is made by mixing alkaline reagent (e.g., sodium hydroxide or potassium hydroxide) with aluminosilicate materials (e.g., metakaolin or fly ash). In Portland cement, C-S-H is the core material for the strength of cement, while the geopolymer is an aluminosilicate gel produced by geopolymerization. Because of the different types of reaction products, durability problems (e.g., alkali silica reaction (ASR) and sulfate attack), which occur in Portland cement, do not occur in geopolymer. Furthermore, geopolymer is also researched as high-fire resistance materials because it is known to have low thermal conductivity and high fire resistance. However, relatively high curing temperatures (e.g., 60°C or 90°C) are required to activate the geopolymer, which is unsuitable for field casting. Due to the that reason, geopolymer is primarily used for precast applications.

1.2.3. Alkali-activated GGBFS

The third alternative cement material is alkali-activated ground granulated blast furnace slag (GGBFS). Alkali-activated GGBFS is made by blending GGBFS with an alkali activator (e.g., NaOH, KOH, and Na-silicate), which has very similar physical properties to Portland cement. As with Portland cement, the main reaction product of alkali-activated GGBFS is C-S-H (I) [14]. Unlike geopolymer, alkali-activated GGBFS can be hardened at room temperature, so can be applied at actual construction sites like Portland cement, as is currently done in Russia [15]. However, despite these advantages, alkali activated GGBFS has several drawbacks: 1) it threatens the safety of users due to the high pH (over ~14); 2) it is more expensive than Portland cement due to the relatively high price of alkali activators (e.g., NaOH, 98% purity, domestic 830won/kg), and 3) NaOH absorbs moisture in the air and can only be used in solution form.

1.2.4. Ca-based activation

To overcome the disadvantages of alkali-activated GGBFS, a Ca-based activated GGBFS binder was developed using CaO (quick lime) or $Ca(OH)_2$ (calcium hydroxide) as an activator [16]. In terms of price, CaO-activated GGBFS is cheaper than alkali-activated GGBFS because the price of Ca-based activators (domestic 100-110 won/kg) is lower than alkali activators (e.g., NaOH). It can also be used in powder form instead of solution form, so it can be packaged like Portland cement. Furthermore, the pH of Ca-based activated GGBFS is about 12.5, which is similar to that of Portland cement, so it

does not threaten the safety of users. According to Kim et al [16], the use of CaO as an activator is reported to be more beneficial in terms of strength than $Ca(OH)_2$. However, despite these improvements, the strength of CaO-activated GGBFS varies greatly depending on the source of GGBFS, and the compressive strength for commercialization is relatively low.

1.3. Outline of Dissertation

As mentioned before, Portland cement is the most widely used construction material in the world, but it is considered to be a major contributor to global warming. To replace Portland cement, many researchers are developing cementless binders using various chemical activators. Many cementless binders activated with strong alkali solutions have been researched, but they have various disadvantages and are difficult to commercialize. For this reason, many researchers have recently developed Ca-based activated cementless binders. Ca-based activated cementless binders have more advantages than alkali-activated cementless binders, but still have the disadvantages of low early compressive strength and mechanical properties which vary depending on the source of raw materials. Therefore, in this study, to enhance the mechanical properties of Ca-based activated cementless binders, various auxiliary chemical activators were applied to the Ca-based cementless binder and its influence was verified using various experiment methods.

Chapter 2 summarizes the background of the experimental techniques used in this study. The background of the laser diffraction particle size analyzer, X-ray fluorescence, hydration stop methods, X-ray diffraction, thermogravimetric analysis, mercury intrusion porosimetry, scanning electron microscopy, isothermal calorimetry, measurement of pH and electrical resistivity of cementitious material are explained in each sub-section.

Chapter 3 verifies the effects of $CaCl_2$ on CaO-activated GGBFS/fly ash binder. Chapter 3.1 presents the background and purpose of the study. Chapter 3.2 explains experimental methods and samples preparation. Chapter 3.3 discusses compressive strength, heat of reaction, XRD, TG, MIP, scanning electron microscopy and electrical resistivity. Chapter 3.4 outlines the main findings in Chapter 3.

Chapter 4 investigates the influence of calcium and sodium nitrate on CaO-activated GGBFS binder. Chapter 4.1 and Chapter 4.2 explain the researcher background and experimental procedure, respectively. Chapter 4.3 discusses compressive strength, measurement results of the pH levels, XRD analysis, TG/DTG, and MIP. Chapter 4.4 summarizes the results of Chapter 4.

Chapter 5 explores the effect of calcium formate on CaO-activated GGBFS binder using various experimental methods. In Chapter 5.1, the research background is described. Chapter 5.2 explains the experimental procedures and samples preparation method. In Chapter 5.3, compressive

strength is explained, along with mercury intrusion porosimetry, x-ray diffraction, and thermogravimetry. Chapter 5.4 outlines of main findings in Chapter 5.

Chapter 6 summarizes the major conclusion of each Chapter achieved in this study. In addition, further research is suggested.

2. EXPERIMENTAL TECHNIQUES AND BACKGROUND

2.1. Laser diffraction particle size analyzer

Particle size is a very important factor in the chemical reaction of cementitious materials. The larger the size of cementitious particles, the less active the chemical reactions are, which affects degree of the hydration and compressive strength [4]. In particular, in the case of GGBFS or fly ash, which is an industrial by-product, which have no quality control process, raw materials should be confirmed whether it can be used as a construction material through the particle size distribution before an experiment. The laser diffraction particle size distribution method is the most common experiment for measuring particle size and distribution of cementitious materials. The experimental procedure of the laser diffraction particle size analyzer is shown in **Figure 2.1**.

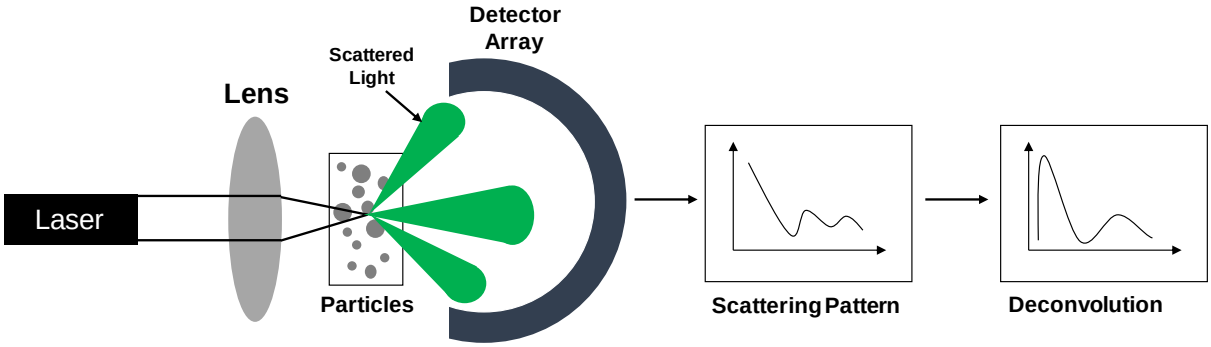

Figure 2.1 Procedure of laser diffraction particel size analyer

Laser diffraction measures particle size distribution of cementitious material using an angular variation in the intensity of light scattered as a laser beam passes through a dispersed particulate sample. Large particles scatter light at small angles with respect to the laser beam, and small particles scatter light at large angles. The scattering intensity data generated by this process can be analyzed to calculate the particle size of cementitious materials, and the scattering pattern cab be calculated using the Mie light scattering theory.

2.2. X-ray fluorescence

As shown in **Figure 2.2**, x-ray fluorescence (XRF) spectroscopy is a non-destructive testing technique that can be used to identify the chemical composition of raw material and is used in the fields of cement, glass, mining, minerals, iron, petroleum, polymers, pharmaceuticals and cosmetics. Fluorescence means that electrons in a material that absorbs light are excited and return to the ground

state to emit light. XRF is based on this principle and is used to qualitatively and quantitatively analyze unknown elements in a sample. The different energies of the characteristic radiation emitted from the sample can be diffracted in different directions by the analytical crystal or monochromator and the intensity of the X-ray of specific wavelength can be measured by positioning the detector at a certain angle.

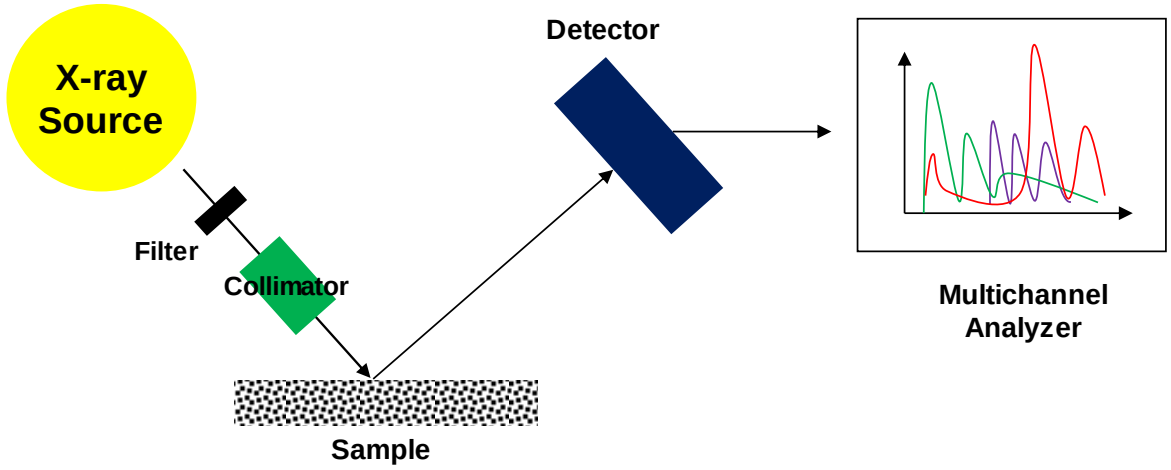

Figure 2.2 XRF mesurement process

2.3. Hydration stop methods

An effective hydration stop method is very important in accurately observing the microstructure of cementitious material on particular curing days. Many researchers have proposed various hydration stop methods (oven drying, D-drying, P-drying, vacuum drying, freezing drying and solvent exchange) [17-20]. However, depending on the characteristics of the sample, improper hydration stop methods may cause damage to the sample. Therefore, the selection of the appropriate hydration stop method is very important for accurate microstructure analysis of cementitious material [21].

Oven drying is a commonly used drying method, drying the sample between 60 and 105°C. The removal of CO_2 in the air is necessary to prevent carbonation, and if the mass of the sample does not change at a constant level, the drying of the sample is considered complete. Although oven drying is effective for the removal of evaporable water, there are many disadvantages. When a sample is stored at 105°C for 24 hours, unbound water disappears, which damages the microstructure. Galle et al [22] also reported that drying at 105°C affected ettringite and C-S-H due to the loss of non-evaporable water. Therefore, Detwiler et al [23] proposed oven drying at 35°C, which is also limited because heat can accelerate the chemical reaction and take a long period of time until there is no change in mass.

D-drying or dry ice drying is the method proposed by Copelande and Hayes [19], which uses a mixture of solid CO_2 and alcohol to maintain the desiccator at -79°C and 4Pa. Under these conditions, removal of the pore solution of the cementitious sample proceeds very slowly, and it takes a long time until the mass of the sample becomes constant. D-drying is an effective method to remove physically adsorbed water and to preserve the microstructure of samples, but is affected by factors such as vacuum level, the sample weight being evacuated, and sample size. D-drying is an effective hydration stop method, but it has been reported to remove interlayer water and has the disadvantage of a long samples preparation period.

Vacuum drying is a method of storing a sample in a chamber with a pressure of 0.1Pa or less. Zhang and Glasser [24] reported that the vacuum drying method decomposes ettringite and monosulphate to increase the volume of the pores and damages the pore structure of the sample. Diamond [22] reported that this method removed less water than oven drying, and Galle [22] reported that vacuum drying causes stress or microcracks in the sample.

The freeze drying method is known to cause less damage to a sample than oven drying, and a hydration stop is performed by immersing the sample in a container filled with liquid nitrogen. After the sample is frozen, the sample is stored at -78°C at a pressure of 4Pa. For smaller samples, the pore water instantaneously freezes and becomes an immediate hydration stop. Galle [22], however, argued that fast freezing creates large ice crystals. In addition, the freeze-drying method is reported to be limited because the sample is not fully dried when the density of the sample is high.

The solvent exchange method is an alternative drying technique for cementitious materials using organic solvents such as acetone, ethanol, isopropanol, and methanol. The sample is immersed into the solution for the hydration stop, and the solution-to-sample ratio, the sample size, and the solvent removal method are very important factors. Depending on the size of the sample, the period of immersion is different, and generally, if the sample size is large, it should be soaked for longer. Gran and Hanpsen [25] reported that a φ5.5 mm × 10 mm sample should be immersed in ethanol for 3 weeks. Beaudoin et al [26] and Zhang and Scherer [21] reported that the microstructure of the cementitious material can be stored with minimal damage when the sample is immersed in IPA and subjected to vacuum drying for 1 day. Therefore, this hydration stop method was used in this study.

2.4. X-ray diffraction

X-ray diffraction (XRD) is an experimental technique to investigate the reaction products of cementitious materials. As shown in **Figure 2.3**, when an X-ray having a wavelength of λ is irradiated at an incident angle of θ to the lattice plane A, B, and C having an atomic distance d of an arbitrary crystal, it is scattered in all directions by the X-ray atom. The scattered X-rays are strengthened by the interference effect, in which the path difference P`RP`` is an integral multiple of the incident X-ray

wavelength. This phenomenon is referred to as a diffraction phenomenon, and the X-ray generated is referred to as a diffracted X-ray. When a diffraction phenomenon occurs, the following equation (1.1) is established between wavelength λ if the incident X-ray and the incident angle θ and the lattice spacing d.

$$n\lambda = 2d\sin\theta \qquad \text{(Eq. 1.1)}$$

where n is an integer called the order of reflection, λ is the wavelength of the incident X-ray, d is the characteristic spacing of a given crystalline phase, and θ is the angle between the incident X-ray and the lattice plane. This equation is called a Bragg`s equation, and when the incidence angle theta represented by the diffraction X-ray is determined, the grating surface interval d is obtained. Generally, with respect to the X-ray diffraction method, a two-theta is used which reflects the geometrical arrangement of the measurement system more than the angle theta between the incident X-ray and the lattice plane. In cementitious materials, identification of crystalline phase, phase composition, and semi-quantitative analysis can be performed using XRD.

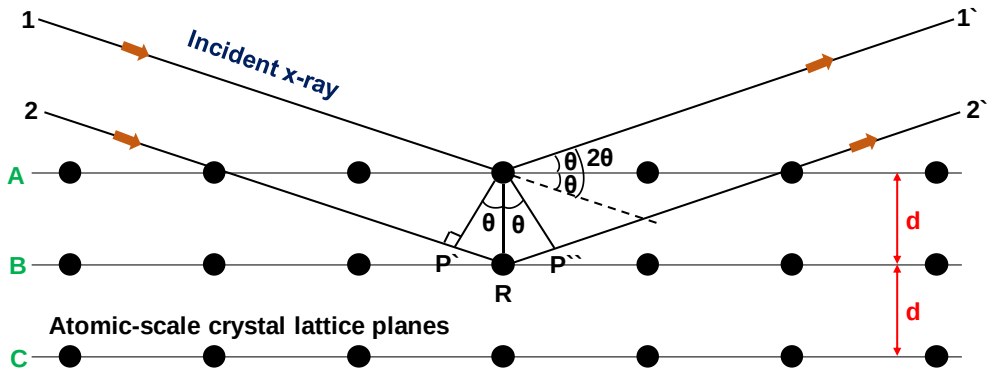

Figure 2.3 Diagram of Bragg`s law

2.5. Thermalgravimetric analysis

Various thermal analysis techniques (e.g., DTA, DSC, and TGA) are used to identify the reaction products of cementitious materials. In this study, TGA was used to analyze the reaction products of cementitious materials and TGA is a method performed by measuring the mass change of the sample as a function of time and temperature while increasing the temperature to 1,010°C. The mass loss of the sample is measured continuously by an electronic balance, which is mainly caused by the evaporation of water or by a chemical reaction. As the temperature of the sample is raised at a constant rate from 25°C to 1,010°C, the mass of the sample changes and is continuously measured by the

electronic balance. The mass change is mainly caused by water evaporation or chemical reaction. In the cementitious materials, mass change occurs by thermal decomposition of phase. The results of TG also can be expressed as DTG, phase identification can be performed according to the position of DTG peak, and the thermal decomposition temperature range of major chemical reactions in cementitious materials is shown in **Table 2.1**. However, Song et al [27] reported that the thermal decomposition range can vary due to the type of activator, source of raw materials, temperature and humidity.

Table 2.1 Temperature ranges of the reaction products for TG, DTA, and DSC

Phase	Temperature ranges of weight change
C-S-H	• 106 ± 4°C due to first loss of water [28] • 129 ± 4°C due to second loss of water [28] • 120°C [29] • 50-200°C [30] • 90-110°C [31]
Ettringite	• 110-150°C [32] • 80-130°C [28]
Monosulfate	• 200°C and 290°C [32]
Gypsum	• 80-220°C via transformation to anhydrite [33] • 100-200°C due to dehydration [34]
Hydrotalcite	• 285°C and 440°C [34] • 200°C and 300-400°C [31] • 230°C and 380°C [35]
Calcium hydroxide	• 400-460°C [36] • 450°C [29] • 390-470°C [35] • 450-490°C [37]
Strätlingite	• 180°C [28] • 180-200°C [38]
Calcite	• 665-800°C [34] • 750°C [29]

2.6. Mercury intrusion porosimetry

Pores are very important factors in cementitious materials because strength and pores are inversely related. Not only the amount of pores, but also the size of pores is also important because pores larger than 50nm are related to strength and impermeability, and pores less than 50nm are associated with drying shrinkage and creep [4]. In this study, MIP was conducted to measure the amount and size of pores in hardened cementitious paste. The MIP is based on the capillary phenomenon that the liquid penetrates into the micropores, and the porosity measurement is carried out by the penetration of mercury. Mercury is a non-wetting liquid and penetration occurs when pressure is applied from the

outside. The porosity can be measured by the principle that higher pressures are required to measure smaller pores. With this principle, not only the volume of the closed pore but also the pore size can be measured. The radius of pores can be calculated in equation (1.2),

$$r_p = \frac{-2\gamma_m cos\theta}{P} \quad \text{(Eq. 1.2)}$$

Where r_p is the radius of pore (m), γ_m is the surface tension of mercury (N/m), θ is the contact angle between mercury and measured material, and P is applied pressure (N/m^2).

2.7. Scanning electron microscopy

An electron microscope is a device that creates an enlarged image of an object using electron beams and electron lenses, and is used to analyze the microstructure of cementitious materials. Since an electron microscope uses an electron beam instead of a light beam, experiments are conducted in a vacuum to prevent energy loss and refraction due to collision of electrons and air. The electron microscope images the surface morphology by measuring secondary electrons, transmission electrons, and X-rays that are generated when the electron beam collides with the surface of the sample (See **Figure 2.4**). In the case of conductive samples, the absorbed electrons are removed through grounding to the stage, whereas non-conduction samples accumulate electrons of the surface of the sample. This phenomenon is called the charge-up phenomenon. Electron accumulation on the surface of the sample interacts with the electron beam to affect the generation and detection of secondary electrons. To prevent the charge-up phenomenon, the surface of the sample is pretreated with a metal such as gold, platinum, or palladium. The electron microscope has high resolution so that objects can be observed at a high magnification, and a magnified image can be obtained from 100,000 times to a maximum 1 million times. The electron microscope provides information such as topography, morphology, and composition. Secondary electron (SE) indicates that a free electron. When an electron beam impinges on the surface of a specimen above a certain energy, the electrons in the metal absorb most of the energy and release the working energy out of the metal. This phenomenon is called secondary emission, in which the electrons impinging on the sample are referred to as primary electrons and the electrons emitted while colliding are referred to as secondary electrons. Secondary electrons are measured by a detector, which is characterized by the ability to view information from the morphology as a three-dimensional image. Secondary electrons are used as basic detectors in SEM to provide detailed information on surface morphology while being relatively low in energy.

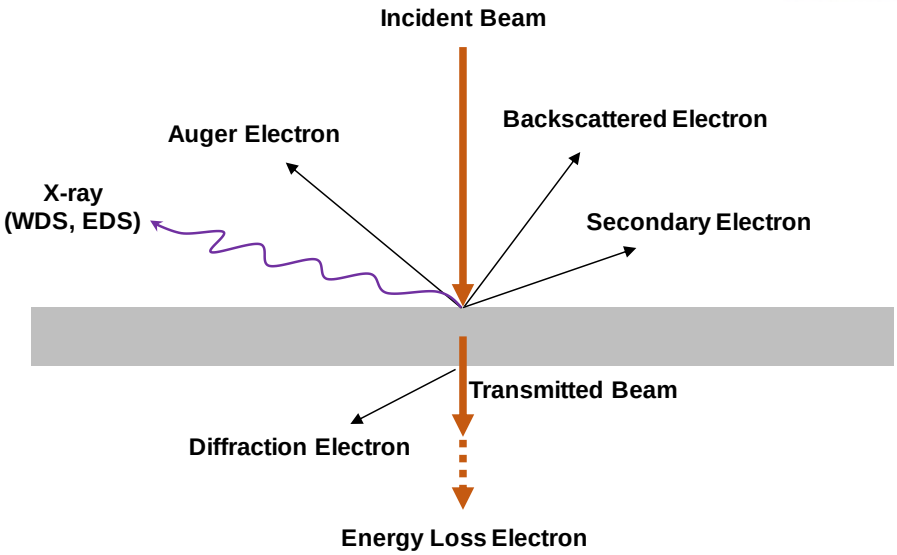

Figure 2.4 Schematic of scanning electron microscope

When electrons collide with the surface of the sample, electrons absorb most of the energy and some of them are reflected or scattered. However, unlike SE, electrons emitted outside the surface of the sample without decreasing the velocity after turning the nucleus are called BSE. Since all elements have different sizes of nuclei and larger nuclei, the number of BSE increases, so we can use these principles to distinguish the different elements on the sample.

An energy dispersive spectrometer (EDS) is a device for analyzing the components of a sample attached to an electron microscope. When an electron beam is injected into a specimen, it becomes exited by the energy in atom. When exited electrons are stabilized, they emit specific X-rays. Since the energy of the specific X-rays emitted for each material is different, this principle is used to analyze the component of the materials.

2.8. Isothermal calorimetry

Heat of hydration in cementitious materials is important because heat generated by cement affects the hydration reaction and hydration degree. In the case of mass concrete, thermal cracks can occur due to heat. The hydration heat is measured using the isothermal method and semi-adiabatic method[39]. In the case of paste and mortar, the former method is used for measuring the heat of hydration, and the latter method is used for concrete. In this study, the isothermal calorimetry method was used to measure the heat of hydration of cementitious materials. Prepare the reference material and sample as shown in **Figure 2.5**. As chemical reaction occurs, heat is generated in the sample. To balance the temperature between the reference material and the sample, subtracting the heat as much as the

sample generates (ΔT). The heat of hydration of the cementitious material is measured by the recorded ΔT during the experiment.

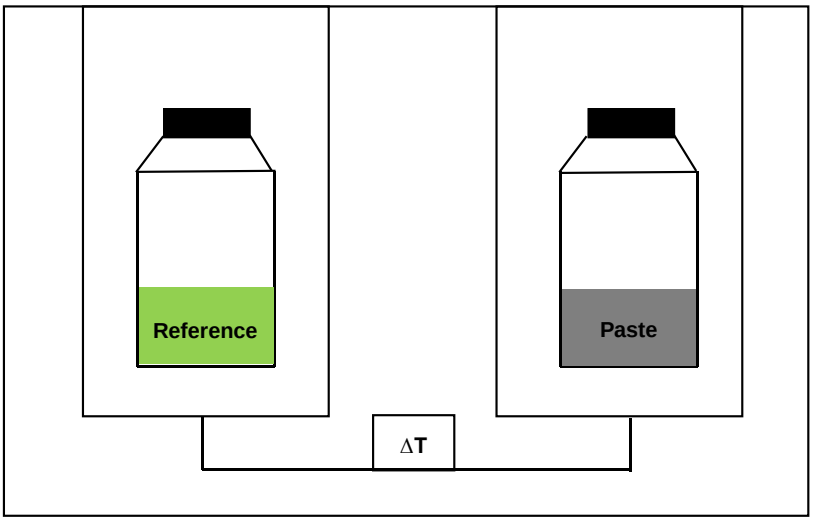

Figure 2.5 Schematic of isothermal conductivity method

2.9. Measurement of pH

The basic mechanism of alkali-activated GGBFS is to dissolve raw material due to high pH and to induce an active chemical reaction in the cementitious material. For that reason, in cementitious materials, particularly alkali-activated GGBFS, the pH of the paste is very significant. The paste of Portland cement has a pH of about 12.5, but NaOH or KOH activated alkali-activated GGBFS has a pH of 14 or higher. Depending on the pH, the dissolution of raw material , degree of hydration, compressive strength, durability and other important mechanical properties vary. The pH measurement technique of paste is usually used to explain the mechanism of strength development of cementitious material. However, in order to measure the pH of the cementitious paste, a different samples preparation procedure is required. If the water to binder ratio is the same as the mixture proportion, the cementitious paste could stuck in the electrode and cannot be tested. Therefore, the water to binder ratio should be 3 or more, and diluted pates should be stirred until the so that diluted the end of the experiment to prevent solidification. A pH meter is shown **Figure 2.6**, the pH meter consists of a reference electrode and indicator electrode. When these two electrodes are immersed in a solution, the current caused by the potential difference is amplified and measured. The intensity of the current is directly proportional to the pH of the solution.

Figure 2.6 Photo of pH meter experiment

2.10. Electrical resistivity of cementitious material

The use of $CaCl_2$ in the cementitious material can cause corrosion of steel bars. Therefore, American Concrete Institute (ACI) committee and other related institutes regulate the maximum amount of $CaCl_2$ in the cementitious materials. For plain concretes, the maximum $CaCl_2$ dosage is 2% of the weight [40]. In addition, for reinforced concrete, ACI 318 [41] limits the maximum chloride content up to 1.00% for reinforced concrete and 0.06% for prestressed concrete. There are many experiment methods (e.g., half-potential method, electrical resistivity, and linear polarization resistance method) to measure the possibility of steel corrosion. Using electrical resistivity the likelihood of corrosion, corrosion rate, and chloride diffusion rate can measured. In order to measure the electrical resistivity, a four-point Wenner probe method is used, which is shown in **Figure 2.7** and four electrodes are located in a straight line and equally spaced.

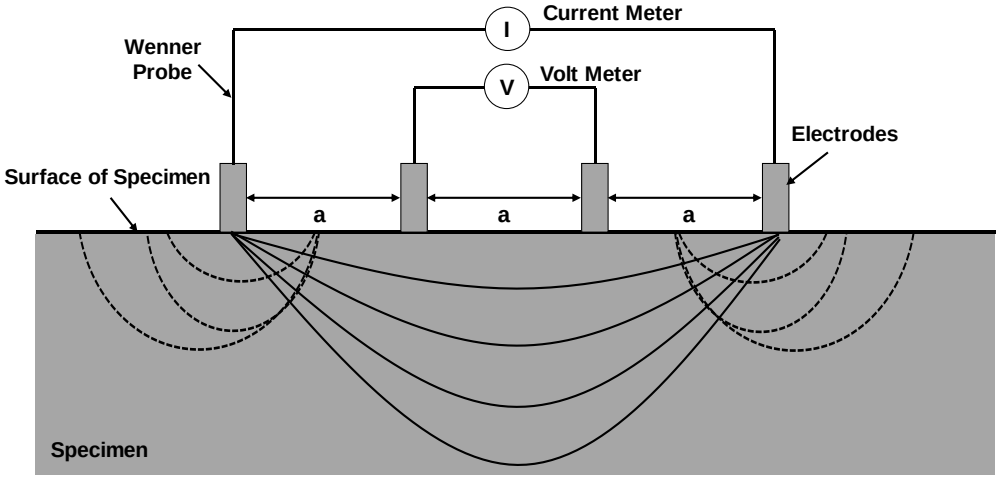

Figure 2.7 Schematic of electric resistivity measurement

When the current I generated by electrodes flows through the concrete, the current flows along the ions in the concrete pores, and the two inner electrodes measure the electrical potential V. The resistivity of cementitious material is measured as

$$\rho = \frac{2\pi V}{I}\ [k\Omega cm] \qquad \text{(Eq. 1.3)}$$

Electrical resistivity of concrete is known to be affected by pore size distribution and interconnection, degree of saturation, environmental temperature, relative humidity, and conductivity of pore fluid and size of specimen. Therefore, many researchers are studying measurement methods based on various conditions. However, if the effects of these factors are taken into account properly, any resistance measurement technique should provide the same resistance value [42].

3. EFFECTS OF CALCIUM CHLORIDE ON HYDRATION AND PROPERTIES OF CAO-ACTIVATED GGBFS/FLY ASH BINDER

3.1. Introduction

Portland cement (PC) is the most widely used construction material, with about 2.8 billion tons produced annually in the world. It is well known that producing one ton of PC releases approximately one ton of CO_2. In comparison, this CO_2 emission is less than other construction materials, such as aluminum [43]. However, the massive quantity of PC produced annually is responsible for 6~8% of global CO_2 emissions [5, 44]. Thus, in order to reduce the usage of PC, earlier studies have made extensive efforts to increase the fraction of supplementary cementitious materials (e.g., ground granulated blast furnace slag (GGBFS) or coal-fired fly ash) [4, 32, 45] or to develop new cementless structural binders [16, 46, 47] for structural concrete production.

In the Republic of Korea, since 1988, ternary blended cements that mainly consist of PC, GGBFS, and fly ash have been commercially used more often in concrete production than PC alone [48, 49]. Not only do blended cements generate lower hydration heats than PC [4] , but market prices of the blended cements are also considerably lower than that of PC, because supplementary cementitious materials are less expensive than PC. The typical weight ratio among PC, GGBFS, and fly ash is 4:4:2 (denoted PC 4:4:2), respectively, and the material cost of PC 4:4:2 is generally ~50 US$/ton.

Recently, CaO-activated GGBFS (CAS) was successfully developed as a new cementless binder to replace PC in concrete production. This binder not only produces comparable strength to PC (30–40 MPa at 28 days), but it is also strongly price competitive with PC, because the material cost of CAS (~50 US$/ton) is significantly lower than that of PC (~68 US$/ton) in Korea.

However, because commercial ternary blended cements (i.e., PC 4:4:2) are similarly inexpensive (or even less expensive) with respect to CAS, in order for CAS to compete with PC 4:4:2 in the concrete market, it also needs to be used in the form of a ternary blended mixture; this may consist of CAS, GGBFS, and fly ash with a weight ratio of 4:4:2 (denoted CAS 4:4:2), respectively, similar to that of PC 4:4:2. However, when PC is simply replaced with CAS in PC 4:4:2, the strength of CAS 4:4:2 could be considerably lower than that of PC 4:4:2, because (1) the increased quantities of GGBFS and fly ash may decrease the overall strength because the reactivity of supplementary cementitious materials (SCMs) is slower than that of PC [50, 51], and (2) even the strength of CAS is often surprisingly low, depending on the source of GGBFS.

$CaCl_2$ is a well-known accelerator for PC systems. The incorporation of $CaCl_2$ significantly shortens initial setting times and increases the early strength of PC systems [4, 32]. In previous research, the similar effects for $CaCl_2$ on GGBFS/fly ash systems have also been reported. Bellmann et al. [47] noted that the addition of $CaCl_2$ increased both early and ultimate compressive strengths in an alkali-

activated GGBFS system. Shi et al. [52] have investigated the effect of $CaCl_2$ on lime-slag blends and lime-fly ash pastes [53, 54]. They reported that $CaCl_2$ enhanced early and later compressive strength of Class F fly ash- and GGBFS-based binders but Class C fly ash-based binders displayed less significant effects than other binders. The main reason for the positive effects of $CaCl_2$ on strength was due to a rapid consumption of $Ca(OH)_2$ in the presence of $CaCl_2$ [55, 56].

The aim of this study was to explore a possible use of $CaCl_2$ to increase the early and final strengths of CAS 4:4:2 to develop a new price-competitive cementless binder for concrete production. To this end, various mixture proportions were designed for compressive strength testing. Conduction calorimetry was also conducted to estimate the possibility of excessive reaction heat generation, which might be induced by the addition of $CaCl_2$. Reaction products and the microstructure of hardened pastes of CAS 4:4:2 binders were characterized using powder X-ray diffraction (XRD), thermogravimetry (TG), mercury intrusion porosimetry (MIP), and a scanning electron microscope (SEM). Furthermore, the electrical resistivity measurements (based on Wenner four-probe resistivity measurement) were performed to evaluate corrosion resistances of the samples.

3.2. Experiment

Table 3.1 presents the chemical and oxide compositions of raw materials (i.e., GGFBS and fly ash), measured using X-ray fluorescence (XRF) (S8 Tiger wavelength dispersive WDXRF spectrometer, Bruker, Billerica, MA, USA), with their loss of ignition (LOI), estimated using TG (SDT Q600, TA Instruments, New Castle, DE, USA). Analytical grades of calcium chloride (Duksan Chemicals, Korea) and calcium oxide (Daejung Chemicals, Korea) were used as activators.

Table 3.1 Chemical compositions of raw materials

GGBFS		Fly ash	
Oxide (wt%)		Oxide (wt%)	
CaO	44.24	SiO_2	52.26
SiO_2	34.30	Al_2O_3	22.59
Al_2O_3	14.28	Fe_2O_3	9.06
MgO	3.26	CaO	6.21
SO_3	1.40	MgO	1.82
TiO_2	0.71	K_2O	1.79
K_2O	0.64	Na_2O	1.78
Fe_2O_3	0.54	TiO_2	1.27
Na_2O	0.27	P_2O_5	1.21
MnO	0.25	SO_3	1.21
SrO	0.07	SrO	0.34
ZrO_2	0.03	BaO	0.24
Y_2O_3	0.01	MnO	0.07

Particle size distributions (See **Figure 3.1)** of raw materials were measured using a laser diffraction particle-size analyzer (HELOS (HI199) and RODOS, Sympatec, Germany). The size distribution of GGBFS was similar to distributions in the literature [16, 45, 49], but fly ash had relatively larger particles of over 80 μm.

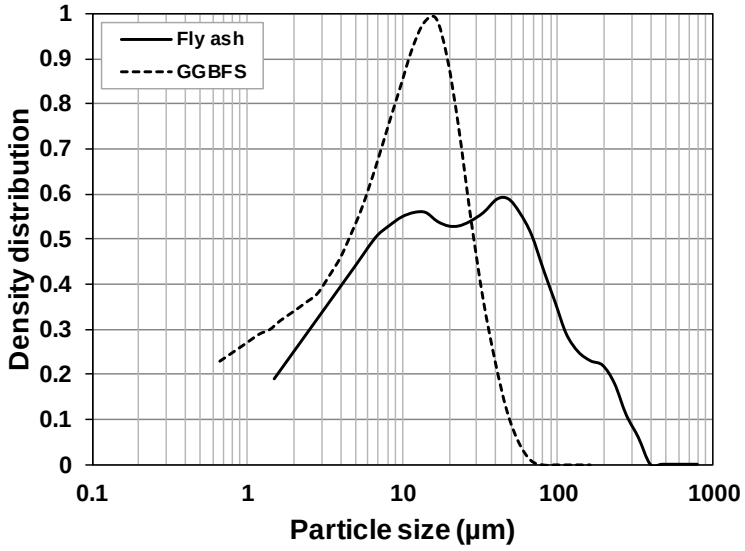

Figure 3.1 Particle size distributions of raw materials

Figure 3.2 presents the XRD patterns of fly ash, GGBFS, and their mixed raw material (74.65% GGBFS and 20.00% fly ash), which were obtained using a high-power X-ray diffractometer (D/MAX2500V/PC, Rigaku, Japan) with Cu-Kα radiation (λ = 1.5418Å). The XRD patterns were analyzed using X'pert HighScore Plus software [57] with the International Center for Diffraction Data (ICDD) PDF-2 database [58] and the Inorganic Crystal Structure Database (ICSD) [59] . Identified crystalline phases were quartz, mullite, and magnetite in fly ash, and akermanite in GGFBS. Amorphous humps were found in all materials. Particularly, the mixed raw material had a similar amorphous hump from GGBFS, because a relatively small fraction of fly ash was included in the mixed raw material, and the intensity of the amorphous hump of fly ash generally appeared much smaller than that of GGBFS in XRD.

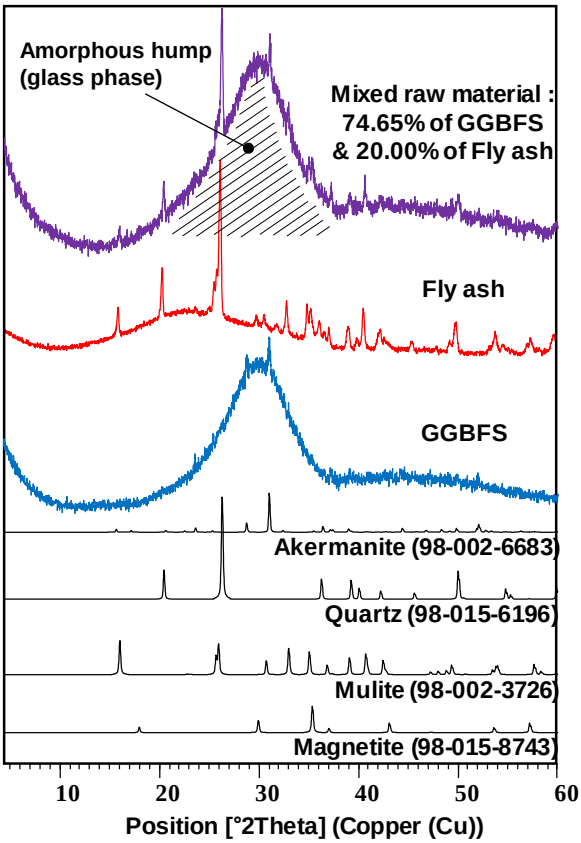

Figure 3.2 XRD patterns of mixed raw material, fly ash, and GGBFS. The numbers in parentheses are ICDD PDF-2 or ICSD data numbers for identified phases

All the mixture proportions shared the fixed weight proportion of 40% CAS binder, 40% GGBFS, and 20% fly ash (i.e., these components constitute CAS 4:4:2) to replicate the proportion among raw materials in PC 4:4:2, as shown in **Table 3.2.** Every CAS binder in each sample in **Table 3.2** had a fixed ratio of 1:9 between CaO and GGBFS, but the samples, denoted 0CSF, 1CSF, 2CSF, and 3CSF, contained different percentages of $CaCl_2$ of 0%, 1%, 2%, and 3%, respectively, to the total weight of CAS 4:4:2. The numbers behind the hyphens in the sample labels indicate water-to-binder (w/b) ratios.

It should be noted that two GGBFSs are seen in separate spaces in each row of **Table 3.2,** even though all the GGBFSs in this study were obtained from the same supply of GGBFS. Although this may lead to confusion in the readers' understanding, the notation of two separate GGBFSs was necessary to imitate a ternary blended mixture. Accordingly, the actual total contents in wt% of GGBFS in 0CSF, 1CSF, 2CSF, and 3CSF were 76.0, 75.1, 74.2, and 73.3, respectively. In addition, to investigate the effect of the w/b, three different ratios (w/b = 0.30, 0.35, and 0.40) were used.

Freshly mixed pastes were cast in cubic molds (5×5×5cm) for compressive strength testing. Cylindrical samples (ϕ2.54×2.54cm) were also prepared for MIP and SEM tests. The cast paste samples

were manually compacted to remove entrapped air voids, and they were demolded after 24 h. All the samples were cured at a constant temperature of 23 °C and at 99% humidity for 3, 7 and 28 days. After compressive strength tests, the fractured samples were gathered and were finely ground for TG and XRD measurements. Then hydration was stopped using solvent exchange with acetone [21] with vacuum drying.

Table 3.2 Mixture proportions (wt%)

Group	Sample label	CAS 4:4:2							w/b
		CAS (A)				GGBFS (B)	Fly ash (C)	Sum (A+B+C)	
		$CaCl_2$	CaO	GGBFS	Sum				
1	0CSF-0.30	0.0	4.0	36.0	40.0	40.0	20.0	100.0	0.30
	1CSF-0.30	1.0	3.9	35.1	40.0	40.0	20.0	100.0	
	2CSF-0.30	2.0	3.8	34.2	40.0	40.0	20.0	100.0	
	3CSF-0.30	3.0	3.7	33.3	40.0	40.0	20.0	100.0	
2	0CSF-0.35	0.0	4.0	36.0	40.0	40.0	20.0	100.0	0.35
	1CSF-0.35	1.0	3.9	35.1	40.0	40.0	20.0	100.0	
	2CSF-0.35	2.0	3.8	34.2	40.0	40.0	20.0	100.0	
	3CSF-0.35	3.0	3.7	33.3	40.0	40.0	20.0	100.0	
3	0CSF-0.40	0.0	4.0	36.0	40.0	40.0	20.0	100.0	0.40
	1CSF-0.40	1.0	3.9	35.1	40.0	40.0	20.0	100.0	
	2CSF-0.40	2.0	3.8	34.2	40.0	40.0	20.0	100.0	
	3CSF-0.40	3.0	3.7	33.3	40.0	40.0	20.0	100.0	

As the presence of $CaCl_2$ in the mixtures might produce an excessive heat of reaction. Isothermal calorimetry was conducted to measure the hydration kinetics of CAS 4:4:2. The hydration heat of CAS 4:4:2 was examined for the samples with w/b = 0.3 (i.e., samples in Group 1) using the three-point multipurpose conduction calorimeter (Tokyo-Riko Co., Ltd., Japan) for the first 72 h at an initial operation temperature of 25 °C. To compare the heat generation with that of PC, the hydration heat of PC was also measured using the same instrument. In this study, PC was selected for testing rather than PC 4:4:2, because a comparison with the hydration heat of PC is more easily understandable for readers.

Powder XRD patterns were recorded for hardened samples from Groups 1 and 3 using a high-power X-ray diffractometer (D/MAX2500V/PC, Rigaku, Japan) with Cu-Kα radiation (λ = 1.5418Å) within a range of 5 to 60°. All the XRD patterns were analyzed using X'pert HighScore Plus software with the International Center for Diffraction Data (ICDD) PDF-2 database and the Inorganic Crystal Structure Database (ICSD).

TG measurements were performed to analyze the reaction products of each mixture in Groups 1 and 3 using a simultaneous thermal analyzer (SDT Q600, TA Instruments, USA) with a heating rate of 30 °C/min from 30 to 1,010 °C in a nitrogen atmosphere in an alumina pan.

To measure the pore-size distribution of each mixture in Groups 1 and 3, MIP (Auto pore IV, Micrometrics, USA) was used. To increase the reliability of the test results, five identical cubic MIP samples for each mixture proportion were prepared and tested. A sample volume of 125 mm^3 (5 mm × 5 mm × 5 mm) was used, and it was kept immersed in isopropanol to cease any further hydration before the testing day.

At 28 days, microstructures of hardened samples were observed on the samples from Group 1, using a high-resolution field emission SEM (S-4800, Hitachi, Tokyo, Japan) with energy dispersive X-ray spectroscopy (EDS). To this end, specimens with a thickness of 2 mm along the length of the cylindrical samples were made using a precision saw. The sliced specimens were immersed in isopropanol to stop hydration. Back-scattered electron (BSE) images and element compositions were obtained from polished surfaces of the sliced samples, prepared using a grinder-polisher (EcoMet 250, Buehler, USA) with a final grit of 1/4 μm of diamond polishing compounds.

Since, in the presence of $CaCl_2$, steel corrosion may be a serious problem when CAS 4:4:2 binders are applied to reinforced concrete structures, electrical resistivity was measured to evaluate the possibility of steel corrosion using Wenner four-probe electrical resistivity measurements [60]. According to KS L ISO 679 [61], CAS 4:4:2 binders (i.e., 0CSF, 1CSF, 2CSF, and 3CSF) were prepared with prismatic mortars (binder-to-sand weight ratio = 1:3). Here, an increased w/b ratio (i.e., 0.5) was used in accordance with KS standard requirements. **Figure 3.3** describes the prismatic sample with dimensions of 20.0×20.0×17.5cm with a single reinforcing steel bar (rebar) embedded in the center. To prevent any possible corrosion on the exposed surfaces of each rebar, its two end surfaces were sealed using epoxy [62]. The electrical resistivity measurements of the hardened samples were taken at 3, 7, 14, 21, 28, and 56 days. Wenner array probes were placed on the top (plane 1) and side (plane 2) surfaces.

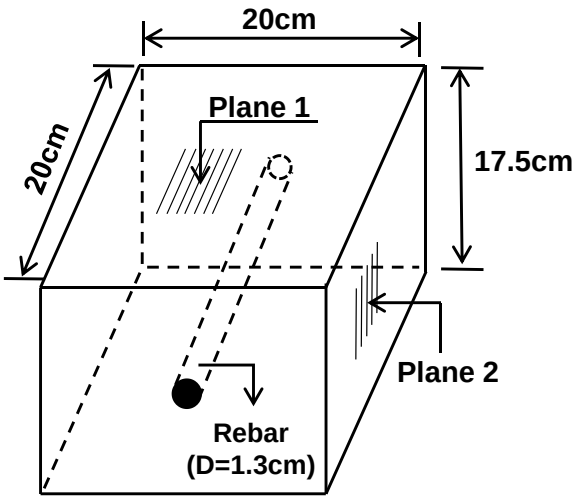

(a)

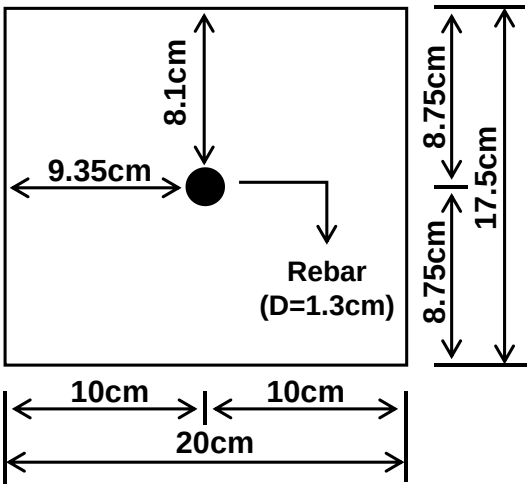

(b)

Figure 3.3 Measuring electrical resistivity of the mortar samples (sand-to-binder ratio = 1:3 at w/b = 0.5): (a) prismatic sample and (b) front and back views of the prismatic sample

3.3. Results and discussion

3.3.1. Compressive strength tests

Figure 3.4 shows the compressive strength testing results of the hardened pastes. The overall strength decreased with the increase of w/b, and it was also largely affected by $CaCl_2$ addition.

In general, $CaCl_2$ is used for cement concrete to accelerate cement hydration, and it particularly influences stiffening, setting, and early compressive strength [4, 63]. However, there is still controversy

about the detailed mechanism of $CaCl_2$'s role in PC systems [56, 64]. Earlier studies suggested that $CaCl_2$ reacted with cement clinkers (i.e. C_3S, C_2S, and C_3A), resulting in a decreased setting time, and increased rates of strength development and hydration process [65, 66].

However, interestingly, despite having no cement compound in this study (see **Table 3.2)**, $CaCl_2$ had a very similar acceleration effect on the CAS 4:4:2 binders. Furthermore, comparing to PC systems, the samples with $CaCl_2$ showed much greater strengths up to 28 days than the samples without $CaCl_2$. In particular, 3-day strengths of the samples with $CaCl_2$ were four to five times higher than those of the samples without $CaCl_2$ at all w/b ratios. Shi et al. [54, 67] also observed a similar strength improvement when $CaCl_2$ was incorporated in a fly ash-based binder.

The increase of $CaCl_2$ up to 2% had a positive effect on strength increase. However, when $CaCl_2$ content was used at 3%, no distinct strength increase (or even a slight strength decrease) was obtained regardless of the w/b ratios, compared to that at 2%, as shown in **Figure 3.4**. Thus, 2% $CaCl_2$ was the best content in this study for strength enhancement.

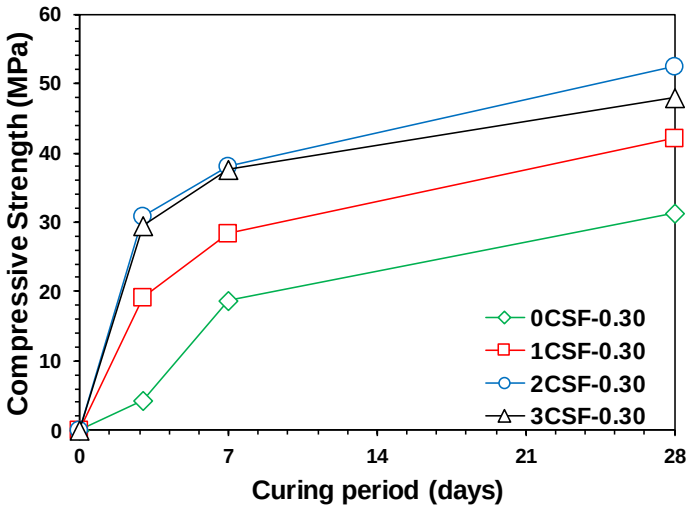

(a)

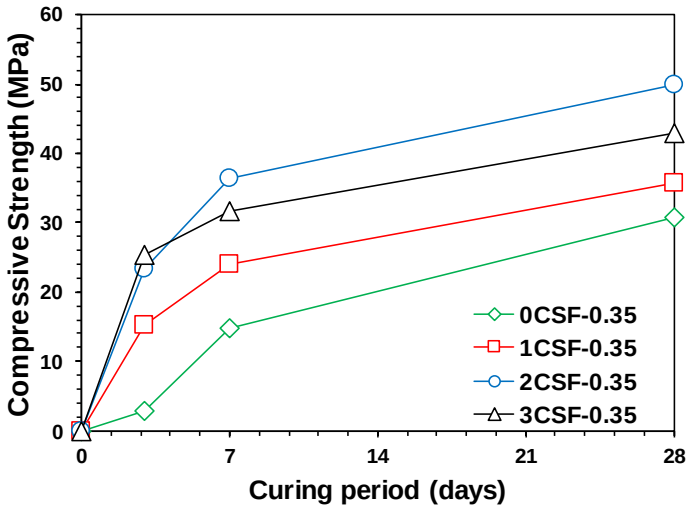

(b)

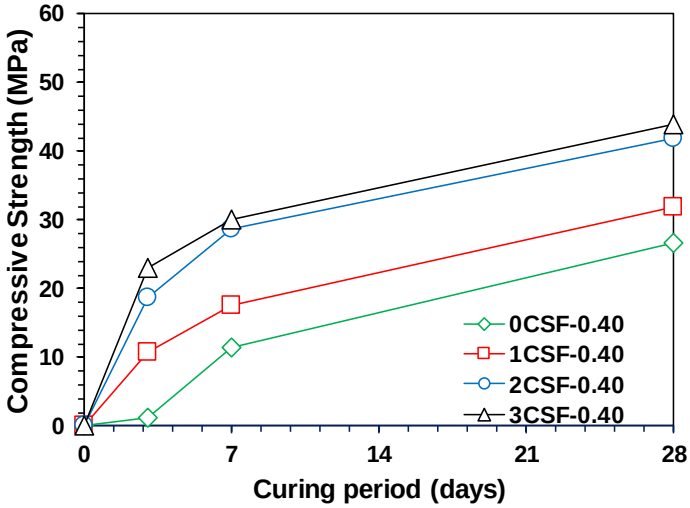

(c)

Figure 3.4 Compressive strength testing results of CAS 4:4:2 binders: (a) w/b = 0.3, (b) w/b = 0.35, and (c) w/b = 0.4

3.3.2 Heat of reaction

Figure 3.5 shows the heat evolution curves for the pastes of CAS 4:4:2 and PC under isothermal conditions at 25 °C for the first 72 h of reaction. Overall, CAS 4:4:2 binders generated significantly lower reaction heats than did PC up to 72 h. The initial sharp peaks instantly occurred after mixing with water. The initial heats of CAS 4:4:2 might be primarily attributed to the wetting and dissolution of CaO and $CaCl_2$. As the dosage of $CaCl_2$ was increased, the intensity of the initial peak also increased. Up to 10 h, in particular, the cumulative heat of the samples with $CaCl_2$ was noticeably

higher than that of PC, which might accelerate the reactivity of CAS 4:4:2 binders from the early time of curing. However, after 10 h, CAS 4:4:2 mixture binders produced much lower cumulative heats of reaction up to 72 h compared to the heat generation of PC paste, mainly because the second peaks of the CAS 4:4:2 binders were much lower than that of PC paste. This lower cumulative heat generation of the CAS 4:4:2 binders after 10 h was likely due to the fact that the chemical reactivity of GGBFS was lower than that of clinker [68].

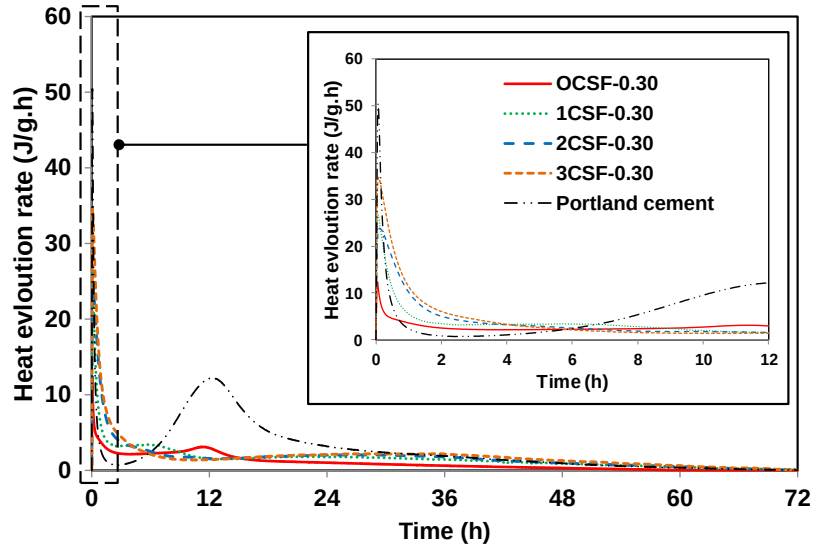

(a)

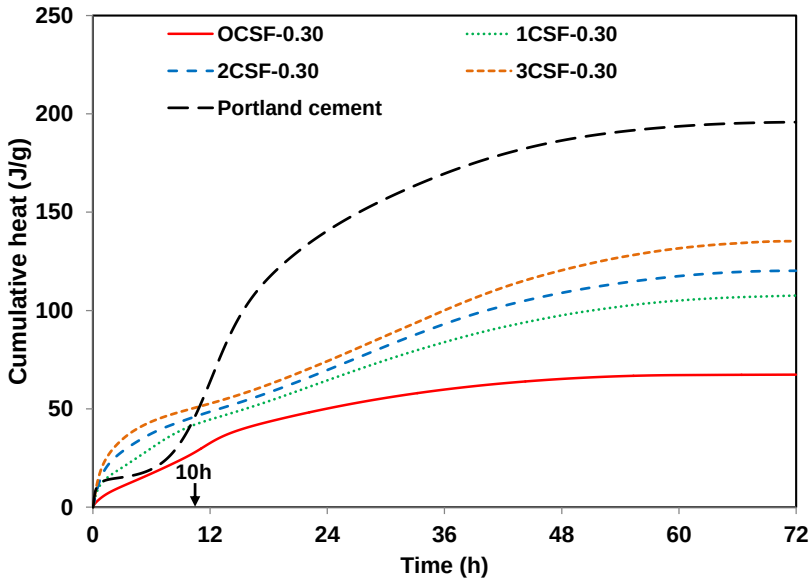

(b)

Figure 3.5 Isothermal conduction calorimetry curves over 72 h: (a) heat evolution rate and (b) cumulative curves

3.3.3 XRD

Figure 3.6 shows the results of the phase analysis of the XRD patterns for hardened pastes of CAS 4:4:2, presented with different w/b values (0.3 and 0.4), dosages of $CaCl_2$ (0–3%), and curing days (3 and 28 days).

In the 0CSF samples (i.e., no $CaCl_2$), regardless of w/b ratio, calcium silicate hydrate (C-S-H), quartz (SiO_2), portlandite ($Ca(OH)_2$), calcite ($CaCO_3$), mullite ($3Al_2O_3{\cdot}2SiO_2$), and hydrotalcite ($Mg_6Al_2(CO_3)(OH)_{16}{\cdot}4(H_2O)$) were commonly identified after 3 days, and strätlingite ($Ca_2Al_2(SiO_2)(OH)_{10}{\cdot}2.5(H_2O)$) was newly produced at 28 days.

In the 1CSF samples, C-S-H, quartz, portlandite, and mullite also similarly identified. However, hydrocalumite ($Ca_2Al(OH)_6(Cl_{1-x}(OH)_x){\cdot}3(H_2O)$, x=0-1) was newly formed and was found in all the samples containing $CaCl_2$ (i.e., 1CSF, 2CSF, and 3CSF). The formation of hydrocalumite might be related to the increased compressive strength after $CaCl_2$ addition.

In the 2CSF and 3CSF samples, C-S-H, quartz, hydrocalumite, and mullite were also found; however, portlandite was no longer present. In these samples, the XRD peaks of hydrocalumite were much stronger than that of 1CSF, and thus, the absence of portlandite in these samples was probably because the addition of $CaCl_2$ increased the reactivity of portlandite [52, 55, 56, 67] and then Ca released from portlandite could contribute to the formations of other reaction products, such as hydrocalumite.

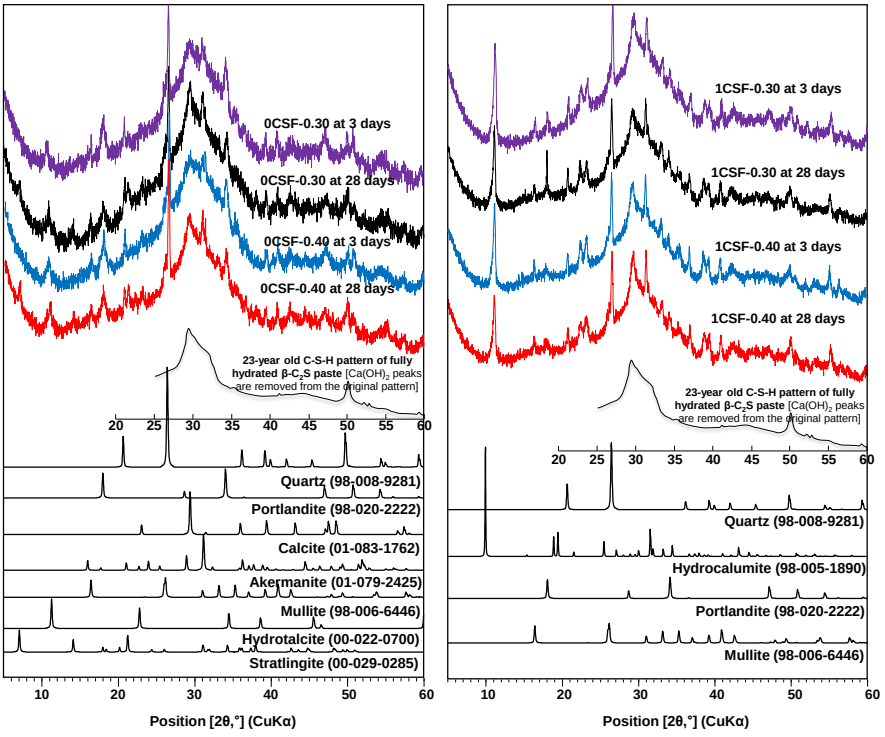

(a) (b)

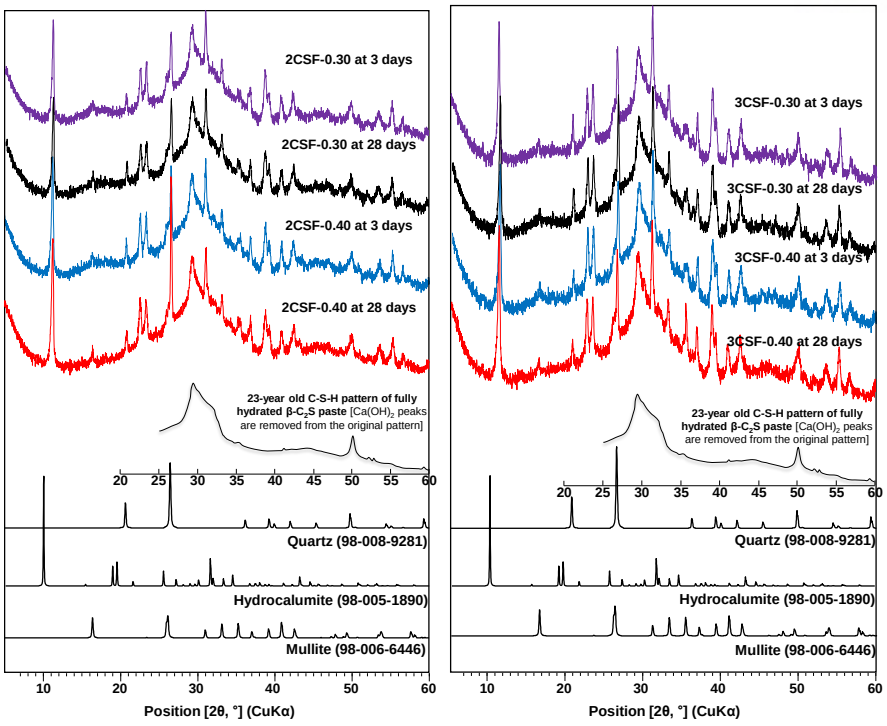

(c) (d)

Figure 3.6 XRD patterns of hardened paste samples of CAS 4:4:2 binders (Groups 1 and 3) at 3 and 28 days: (a) 0CSF, (b) 1CSF, (c) 2CSF, and (d) 3CSF. The numbers in parentheses are ICDD PDF-2 or ICSD data numbers for identified phases

Figure 3.7 presents the change of amorphous humps near 2θ = ~22–37° from 3 to 28 days using overlaid XRD patterns of mixed raw material (74.65% GGBFS + 20.00% fly ash) and hardened pastes. As mentioned earlier, due to the low weight fraction of fly ash, the amorphous humps mainly originated from the GGBFS, but some portion was taken from the fly ash.

The influence of the $CaCl_2$ addition on the reactivity of GGBFS and fly ash during CaO activation may be estimated using **Figure 3.7,** because the greater decrease of the amorphous hump generally indicates a higher degree of dissolution of the glass phase of GGBFS and fly ash [67, 69]. At 3 days, as in **Figure 3.7 (a),** the amorphous humps in the samples with $CaCl_2$ (i.e., 1CSF to 3CSF) were more clearly reduced than that of the sample without $CaCl_2$ (i.e., 0CSF). However, at 28 days, as in **Figure 3.7 (b)**, the amorphous hump of 0CSF was also largely reduced. Interestingly, the 1–3CSF samples had very similar XRD profiles at 3 days, except for the peak intensities of hydrocalumite, which increased as the content of $CaCl_2$ was increased; after 3 days, these samples showed no change in their XRD profiles as the curing time progressed. These observations indicate that the presence of $CaCl_2$ largely accelerated the dissolution of the glass phase of GGBFS and fly ash in the early days, regardless of the $CaCl_2$ dosage, when the content of $CaCl_2$ was incorporated above 1.0 wt. %.

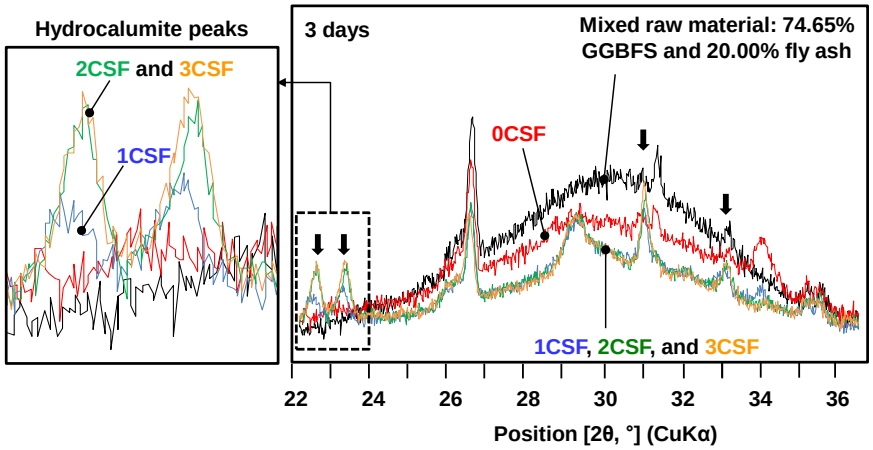

(a)

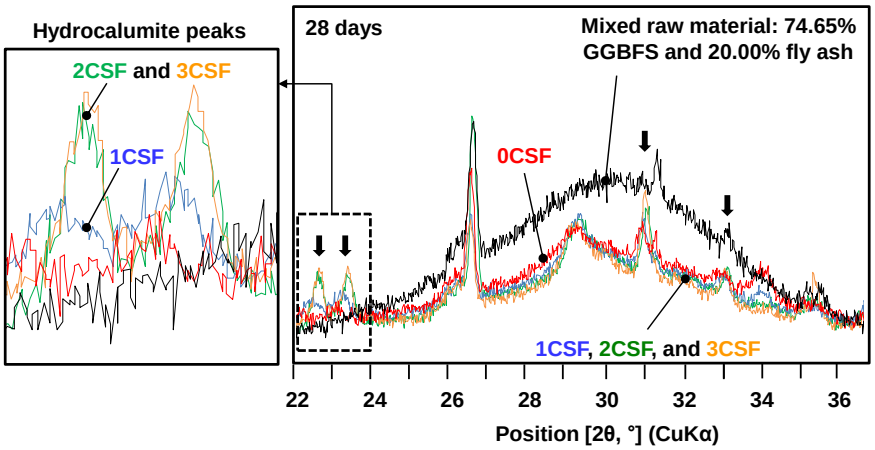

(b)

Figure 3.7 Overlaid XRD patterns of mixed raw material (GGBFS + fly ash) and hardened samples with w/b = 0.40 at 2θ = ~22-37° (a) at 3 days and (b) at 28 days

3.3.4 TG

Figure 3.8 shows the TG/DTG results of the hardened pastes of CAS 4:4:2, prepared with three variables: w/b ratio, dosage of $CaCl_2$, and curing days.

Table 3.3 summarizes the temperature ranges of substance decomposition in TG from earlier studies.

In the 0CSF samples in **Figure 3.8 (a)**, C-S-H, $Ca(OH)_2$, and calcite were identified at all days; strätlingite was only found at 28 days. The weight losses around 100 °C were mainly due to the presence of C-S-H. The DTG results illustrate that the weight of C-S-H at 3 days was considerably smaller than that at 28 days.

In the 1CSF samples in **Figure 3.8 (b)**, C-S-H and $Ca(OH)_2$ were also found; however, strätlingite almost disappeared, and hydrocalumite was newly formed. The DTG peaks near 100 °C, which were attributed to the losses of C-S-H and hydrocalumite, were notably stronger and sharper than those of the 0CSF samples at both 3 and 28 days. Compared to 0CSF, the 1CSF sample showed a much smaller difference in TG between 3 and 28 days, because C-S-H and hydrocalumite had already extensively formed before 3 days.

In the 2CSF and 3CSF samples in **Figure 3.8 (c)** and **(d)**, only C-S-H and hydrocalumite were identified; $Ca(OH)_2$ was no longer seen because of its high reactivity in the presence of $CaCl_2$ [52, 67].

Significantly stronger DTG peaks near 100 °C were found than those for 0CSF and 1CSF. Although it was difficult to quantitatively compare the quantities between these products because the peaks of C-S-H and hydrocalumite overlapped near 100 °C, considering that the second peak near 320 °C also indicated hydrocalumite, it was clear that more hydrocalumite formed as the $CaCl_2$ content increased.

Overall, the TG/DTG results were consistent with the XRD results. In each mixture, (1) more weight was lost at 28 days in TG compared to that at 3 days, regardless of the dosage of the $CaCl_2$ and the w/b value, but (2) as the $CaCl_2$ content increased, the difference in the weight loss (up to 1,000 °C) between 3 and 28 days substantially decreased. At each day of curing, the higher $CaCl_2$ dosage induced a higher weight loss of the sample up to 1,000 °C in TG; this indicates the increased formation of thermally decomposable reaction products. Therefore, the use of $CaCl_2$ caused the acceleration of the reaction, and it generated a greater quantity of reaction products. However, the influence of w/b on TG/DTG was not clear in this study.

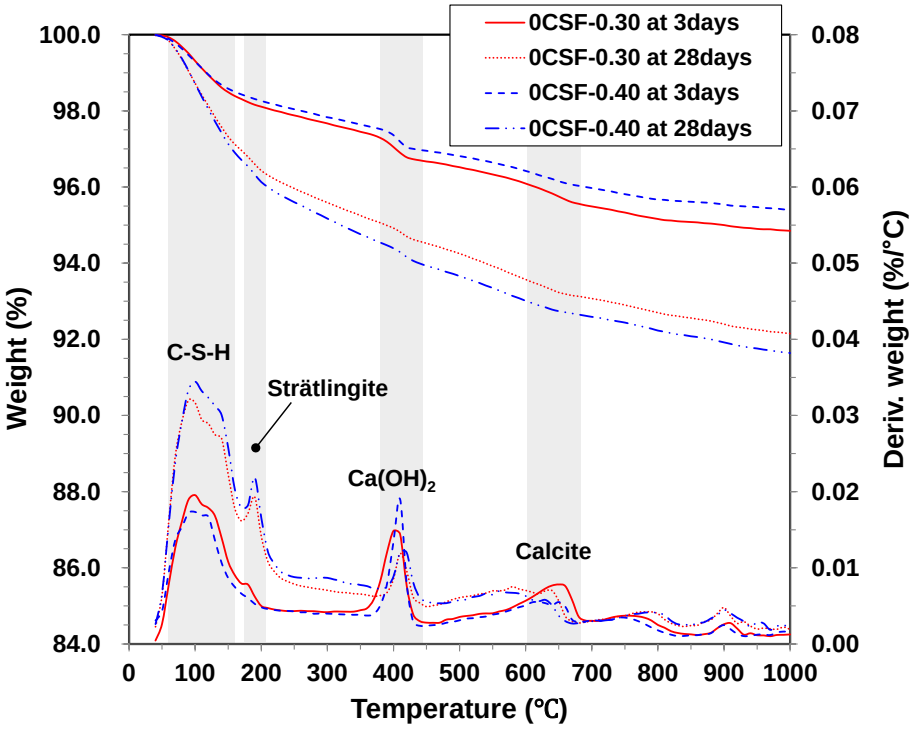

(a)

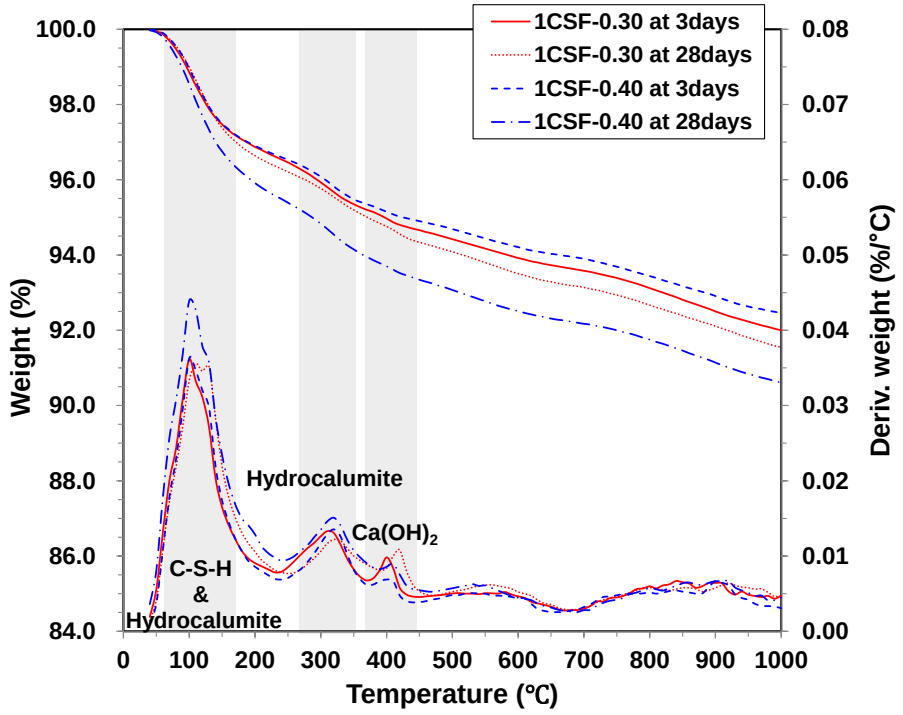

(b)

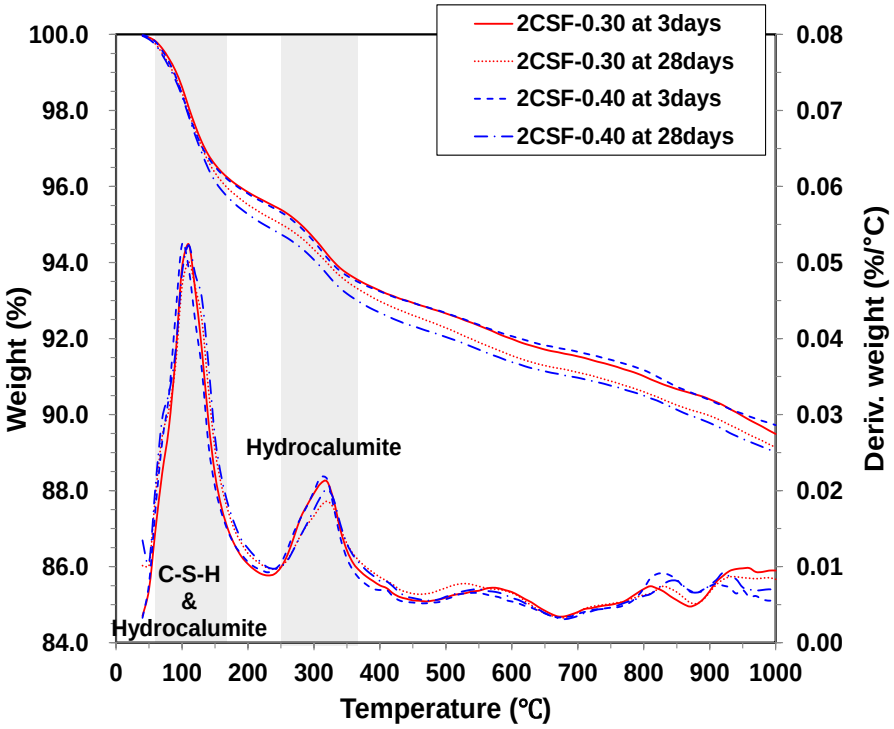

(c)

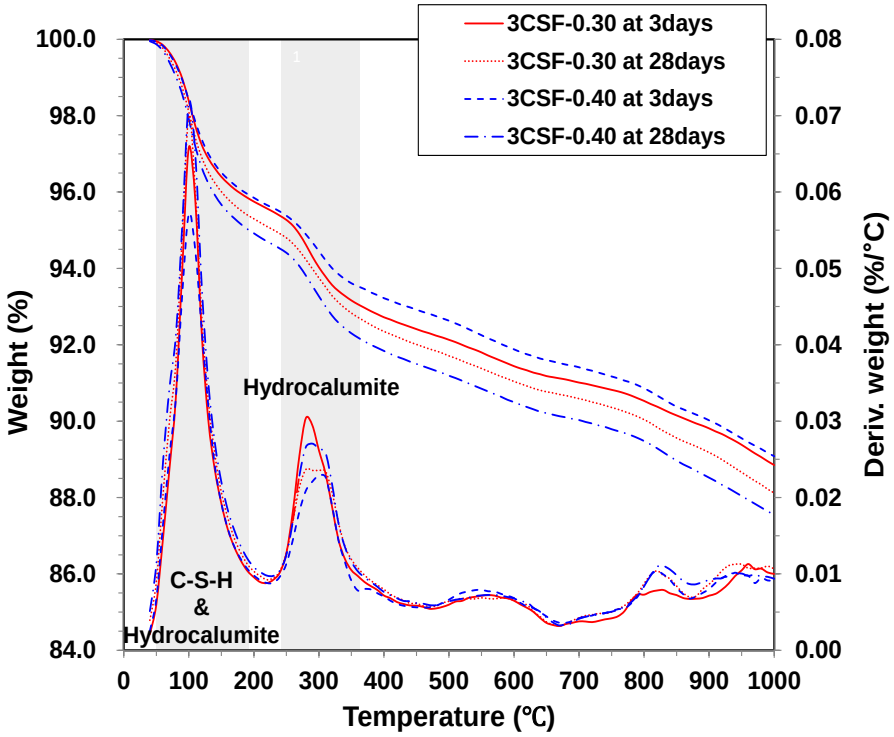

(d)

Figure 3.8 TG and DTG curves of hardened pastes of CAS 4:4:2 mixture samples with different w/b values (i.e., w/b = 0.30 and 0.40, Groups 1 and 3, respectively) and curing days (i.e., 3 and 28 days): (a) 0CSF, (b) 1CSF, (c) 2CSF, and (d) 3CSF

Table 3.3 Reference temperature ranges of weight loss in TG

Phase	Temperature ranges of weight change
C-S-H	▪ 106 ± 4 °C due to first loss of water [28] ▪ 129 ± 4 °C due to second loss of water [28] ▪ 120–145 °C [29]
Strätlingite	▪ 180–200 °C [29]
$Ca(OH)_2$	▪ 490–525 °C [29] ▪ 496 ± 4 °C [28] ▪ 400–450 °C [70] ▪ 480 °C, 530–550 °C, or 425–550 °C [32]
Calcite	▪ 665–800 °C [34] ▪ 750 °C [29]
Hydrocalumite	▪ 25–250 °C [71] ▪ 250–400 °C [71]

3.3.5 MIP

The pore-size distributions and total porosities are presented in **Figure3.9** for the samples from Groups 1 and 3. Note that in general, the strength of hardened paste is inversely proportional to its total porosity and overall capillary pore size [4].

In the samples without $CaCl_2$ (i.e., 0CSF-0.30 and -0.40), regardless of w/b, large sizes of capillary pores (~50 nm–1 μm) were clearly recognized at 3 days. After 28 days, these pores had completely disappeared, and small pores became smaller. Thus, in these samples, significant pore-size refinement [4] occurred after 3 days, resulting in notable strength at 28 days (see **Figure 3.9)**, whereas in the other samples with $CaCl_2$ addition (1CSF to 3CSF), little to no large capillary pores were present even at 3 days. In particular, at 3 days, as the content of $CaCl_2$ increased, the overall capillary pore size consistently decreased (see **Figure3.9 (a)** and **(c)**), although at 28 days, this tendency was much diminished. The TG/DTG results in **Figure 3.9** exhibit the fact that the greater quantity of $CaCl_2$ caused an increase in reaction products at 3 days. Thus, the increased quantity of reaction products might more effectively fill the capillary pores in the matrix, resulting in enhancement of the early compressive strength. Even though there has been no previous study demonstrating that the formation of hydrocalumite largely increases the compressive strength of cementitious binding materials, the MIP results in this study provide some indication that it might affect the strength by filling pores. Therefore, the use of $CaCl_2$ largely accelerated pore-size refinement at an early stage of curing, resulting in an increase in the early compressive strength.

It is clear that the addition of $CaCl_2$ not only accelerated the capillary pore-size refinement, but it also decreased the total porosity of the hardened sample; at each figure in **Figure3.9**, the largest total porosity was found only in the sample without $CaCl_2$ (i.e., 0CSF), which also showed the lowest strength.

However, when comparing total porosities among the samples with different $CaCl_2$ contents at a given day (i.e., 3 or 28 days), the $CaCl_2$ content inconsistently affected the total porosity of the sample. For instance, at 28 days, the sample with 2% $CaCl_2$ produced the largest total porosity at w/b = 0.30, as seen in **Figure 3.9 (c)**, despite having the highest strength; however, the same 2% $CaCl_2$ content resulted in the smallest total porosity at w/b = 0.40 in **Figure 3.9 (d)**.

Furthermore, in this study, every sample with $CaCl_2$ consistently showed an increase of total porosity from 3 to 28 days, despite the significant strength increase during that period. Two possible explanations may be suggested for these observations of the unclear trend in the influence of $CaCl_2$ content on the total porosity. First, it is worth noting that all the samples contained a substantial portion of air voids with sizes near 100 μm. Air voids (e.g., entrained or entrapped air) might be randomly incorporated during the mixing process. These air voids were also counted in calculating the total porosity, and thus, the total porosity values were likely to be randomly affected to some extent by these voids. These air voids are known to be much less influential on strength than capillary pores, which are pores smaller than 1 μm, because air voids are generally spherical [4]. Secondly, there were several samples (1CSF-0.40, 2CSF-0.30, and 3CSF-0.30) that showed a volume increase of very small-sized capillary pores (< 50 nm), resulting in an increase of total porosity, with curing time. However, the volume increase of these very small capillary pores is also known to have a minor impact on strength [4].

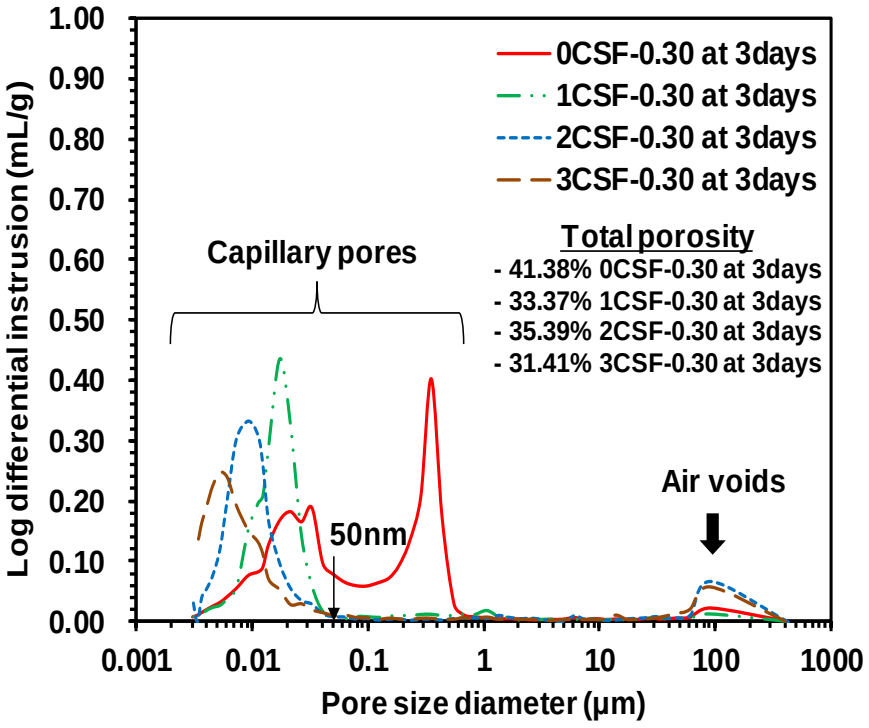

(a)

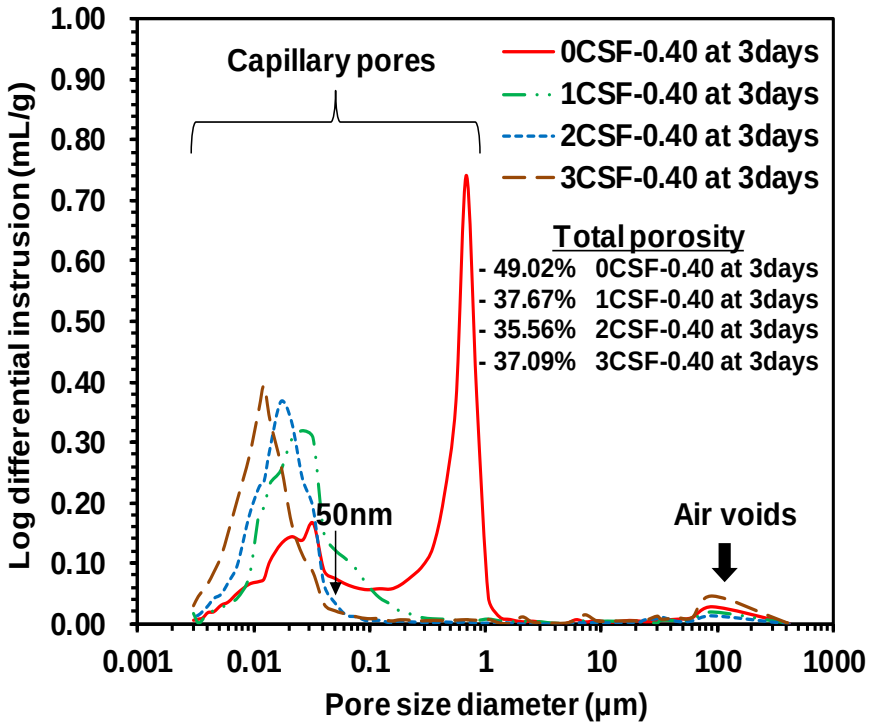

(b)

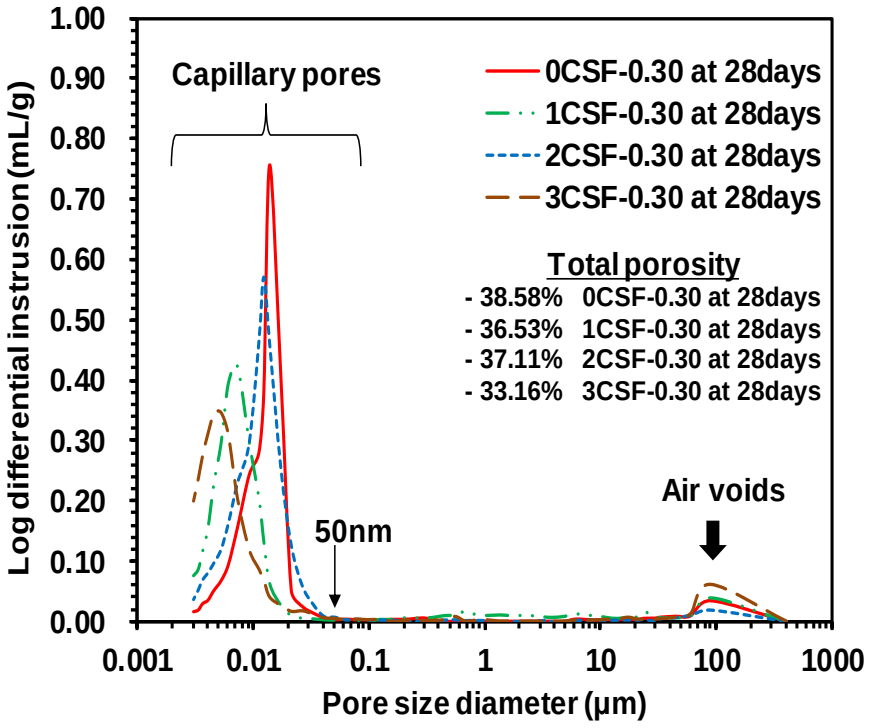

(c)

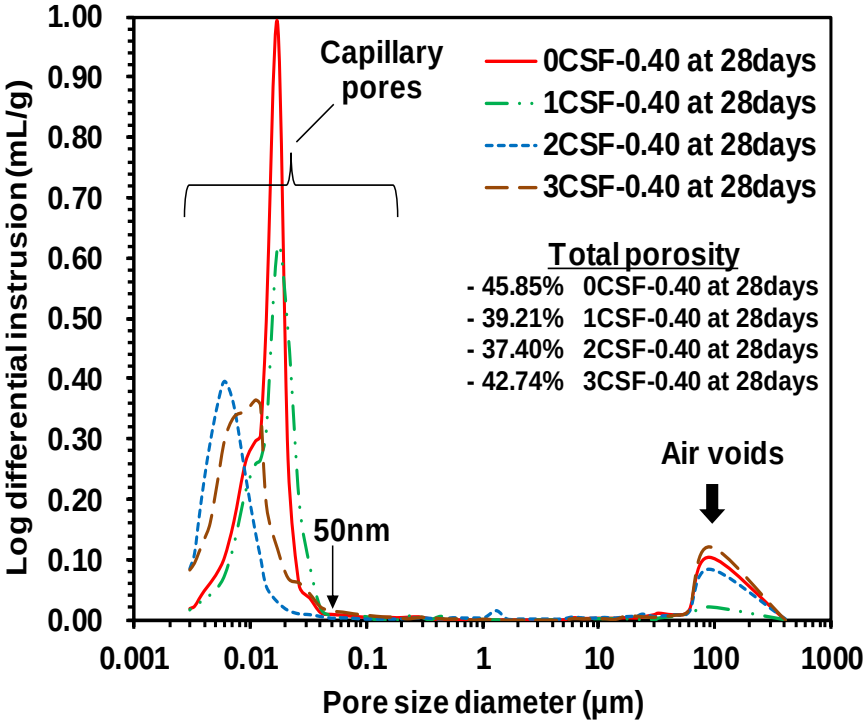

(d)

Figure 3.9 Pore-size distributions and total porosities of hardened pastes of CAS 4:4:2 binders: (a) w/b = 0.30 at 3 days, (b) w/b = 0.30 at 28 days, (c) w/b = 0.40 at 3 days, and (d) w/b = 0.40 at 28 days

3.3.6 Scanning electron microscopy

The backscattered electron (BSE) images at 28 days for the polished CAS 4:4:2 samples from Group 1 are shown in **Figure 3.10**. All samples showed large portions of unreacted particles of GGBFS (mainly angular shape) and fly ash (generally spherical form), similarly to earlier studies [30, 72, 73]. However, remarkable differences in microstructure were observed between the samples with $CaCl_2$ (i.e., 1 to 3CSF) and the sample without $CaCl_2$ (i.e. 0CSF). The paste matrices in the samples with $CaCl_2$, the areas apart from residual GGBFS and fly ash particles, showed rather higher brightness in the BSE images than those of 0CSF. This illustrates that their matrices were more densely filled with reaction products. Note that among the pores in the MIP result from Group 1 at 28 days (see **Figure3.9 (c)**), only the pores below ~50 nm affected the brightness of the BSE images; the air voids near 100 μm cannot be seen in the BSE images, as these pores were too big to be included in the images. Thus, this result is consistent with the results of XRD, TG, and MIP.

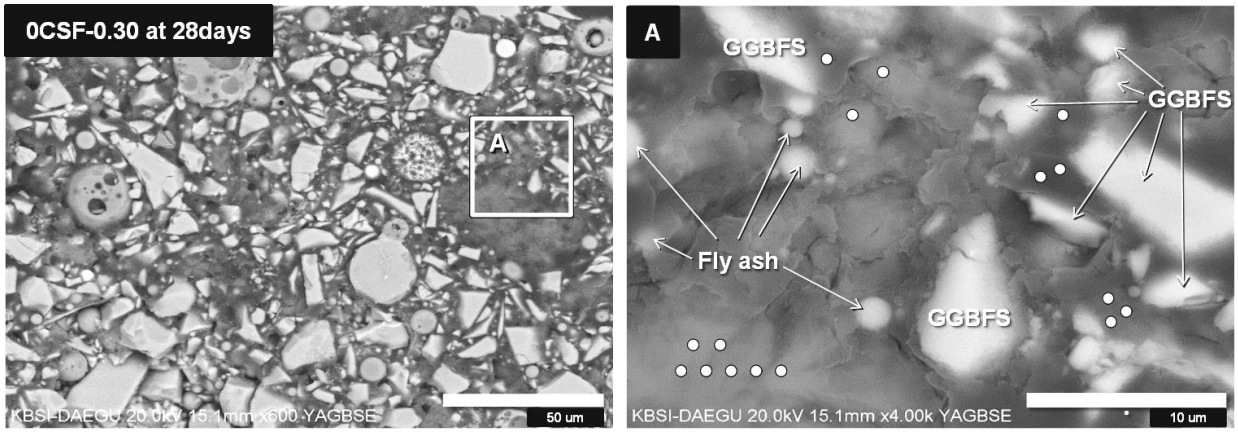

(a)

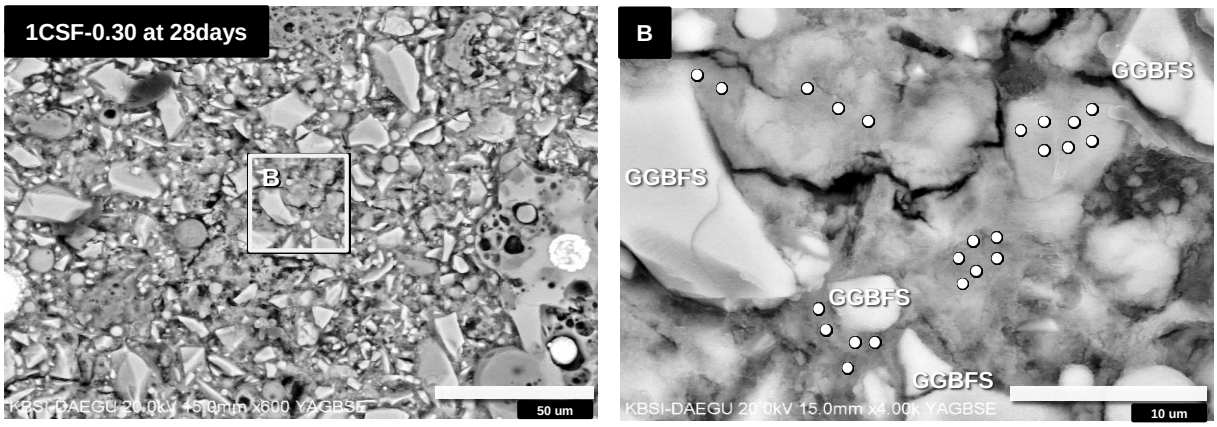

(b)

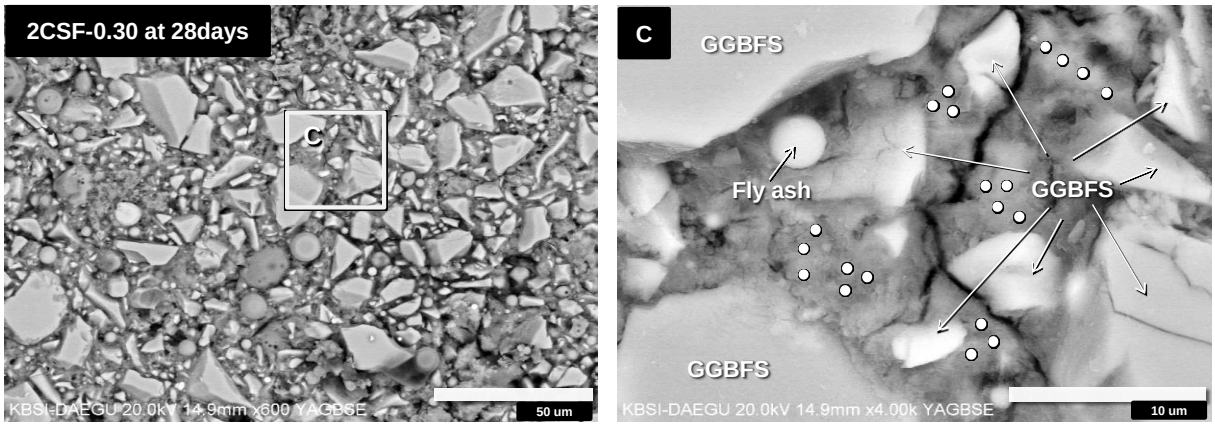

(c)

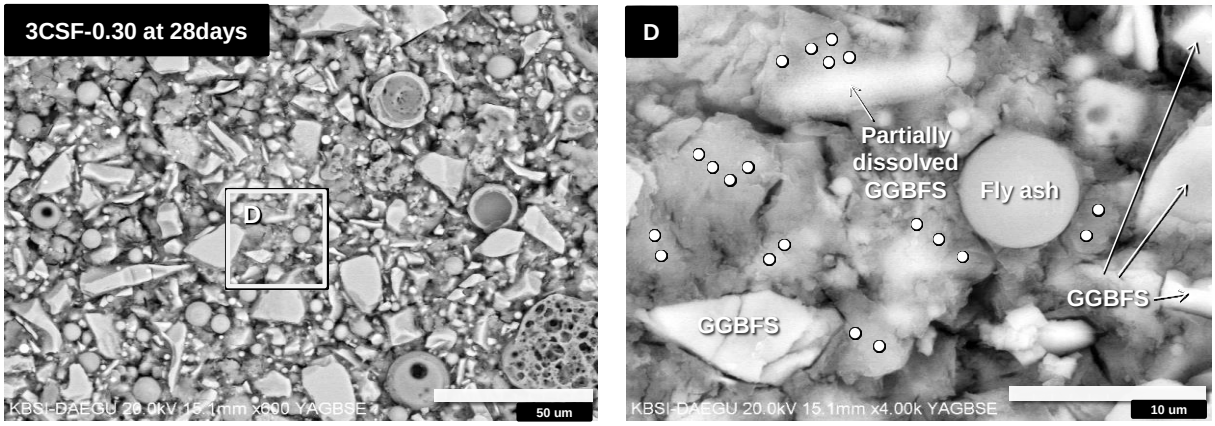

(d)

Figure 3.10 Back-scattered electron images of (a) 0CSF, (b) 1CSF, (c) 2CSF, and (d) 3CSF at w/b = 0.30 at 28 days. The solid circles indicate the locations of EDS spot analysis

Table 3.4 Average atomic ratios of raw materials from XRF and those from EDS results from the locations in **Figure 3.10**

Atomic ratio	EDS results from hardened samples				XRF results from raw materials	
	0CSF	1CSF	2CSF	3CSF	GGBFS	Fly ash
Na/Al	0.01	0.02	0.07	0.11	0.03	0.1
Ca/Al	2.7	6.8	4.8	2.2	5.6	0.5
Si/Al	3.1	3.1	2.7	2.6	2.27	1.1

Elemental spot analysis was performed at 50 locations in the solid matrix regions of all the hardened samples, which were chosen after excluding residual particles of raw materials (i.e., GGBFS and fly ash) and cracks, as indicated by the white solid circles in **Figure 3.10.** The averaged results of Na/Al, Ca/Al, and Si/Al are tabulated in **Table 3.4**. To aid in understanding, the atomic ratios of GGBFS and fly ash are also given.

The only Na sources in this study were GGBFS and fly ash. Even if one considers that the weight fraction of fly ash was much smaller than that of GGBFS in the mixture proportion (i.e., GGBFS:fly ash = 74.65:20.00 in wt%), because the original Na_2O content of raw fly ash was considerably higher than that of raw GGBFS, the GGBFS and fly ash had similar capacities to supply Na to the matrices. However, it should be noted that raw fly ash has a considerably higher Na/Al value than that of GGBFS. If the Na/Al ratio of a solid matrix was more similar to that of fly ash, then the matrix might consist of a greater portion of dissolved fly ash than of GGBFS. In **Table 3.4**, the Na/Al ratio of the samples increased with the increase in the $CaCl_2$ content, and it experienced a great leap above the addition of 2% $CaCl_2$ (i.e., 2CSF). This observation might suggest that the fly ash was not dissolved to a great

extent until the $CaCl_2$ content reached 2% and that the use of $CaCl_2$ over 2% markedly promoted the dissolution of the fly ash.

A significantly large portion of Ca in the matrices likely originated from the dissolution of GGBFS, because the entire summed Ca content from the other raw materials (i.e., raw fly ash, CaO, and $CaCl_2$) was much lower than that of raw GGBFS (see **Table 3.1** and **Table 3.2**); thus, in **Table 3.4**, the high value of Ca/Al at a 1% $CaCl_2$ addition shows that a considerable degree of GGBFS dissolution occurred even at this $CaCl_2$ addition. However, above a 2% $CaCl_2$ addition, the Ca/Al ratio largely decreased, and the Ca/Al value at 3% $CaCl_2$ was even lower than that of 0% $CaCl_2$. This observation suggests two possible situations above 2% $CaCl_2$: (1) a large increase in the dissolution of fly ash, resulting in more Al release and a greater strength, and (2) disturbance in GGBFS dissolution, leading to decreased Ca release and a lower strength. The former case was reasonably credible, given the earlier discussion, but the latter was also possible, because the strength started to decrease at the 3% $CaCl_2$ addition. However, it should be noted that the XRD results at 28 days in **Figure 3.7 (b)** showed seemingly similar amorphous humps at ~22-37° regardless of the $CaCl_2$ dosage; thus, the XRD results might appear inconsistent with the latter suggestion. However, a closer look at the patterns reveals that these humps at 28 days were slightly different to each other when compared to those of 3-day samples. Furthermore, these humps at ~22-37° at 28 days included not only the amorphous humps from GGBFS and fly ash, but also contained the humps of C-S-H. Therefore, it is difficult to use these patterns in **Figure 3.7** for distinguishing the dissolution degrees of raw materials (i.e., GGBFS vs. fly ash) at 28 days.

3.3.7 Electrical resistivity of prismatic mortar samples of CAS 4:4:2

The presence of $CaCl_2$ in binders can cause severe corrosion of embedded steel bars. Therefore, the American Concrete Institute (ACI) committee placed regulations on the maximum dosage of $CaCl_2$ in PC concretes. For plain concretes, the maximum $CaCl_2$ dosage is 2% of the weight according to ACI 212 [40]. For reinforced concretes, ACI 318 places limits on the maximum chloride content: up to 1.00% for reinforced concrete and 0.06% for prestressed concrete [41]. In the present study, the 2CSF sample, which showed the greatest improvement in strength, satisfies ACI 212 but not ACI 318. Therefore, the developed binder should be first applied to unreinforced concrete structures, such as unreinforced concrete pavement, concrete dams, breakwater concrete blocks, etc. There is a need for more information on the corrosion resistance properties of CAS 4:4:2 samples in applications to reinforced concrete with protected steel bars.

Figure 3.11 shows the measured electrical resistivity of the mortar samples at 3, 7, 14, 21, 28, and 56 days. Interestingly, a higher electrical resistivity was obtained in samples with larger additions of $CaCl_2$ because denser matrices result in lower electrical conduction in non-metallic solids. The MIP

results showed that the presence of $CaCl_2$ caused the formation of a denser matrix than in the benchmark sample without $CaCl_2$. This indicates that higher corrosion resistance can compensate for chloride content originating from $CaCl_2$. To validate this complex relationship between chloride contents and electrical resistivity, further research is required.

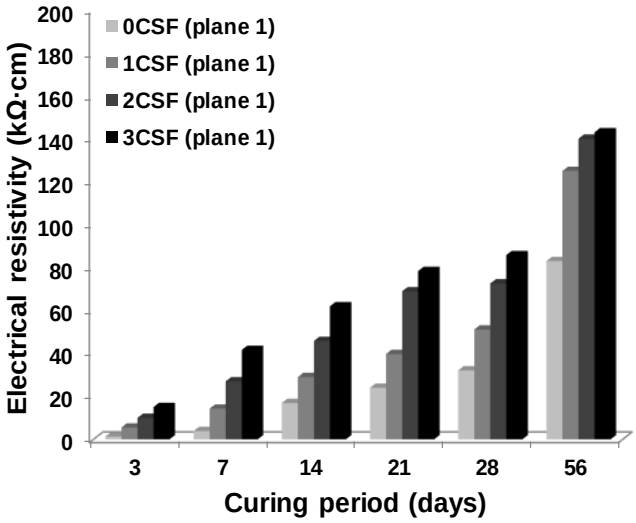

(a)

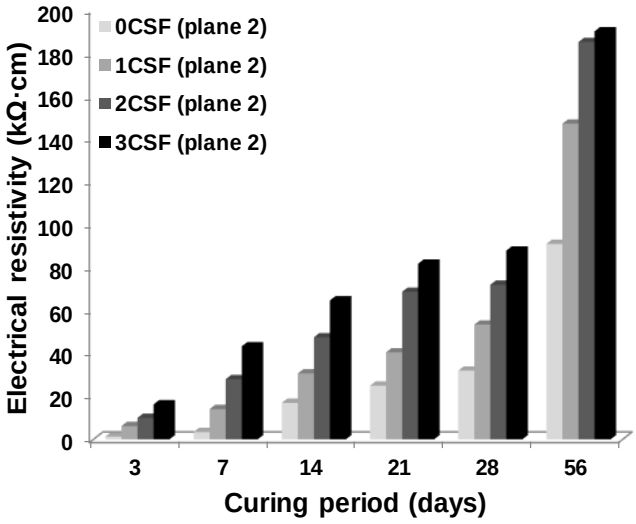

(b)

Figure 3.11 Electrical resistivity of hardened mortar samples of the CAS 4:4:2 mixture on (a) plane 1 and (b) plane 2

3.3.8 Further discussion

$CaCl_2$ is known as the most widely used accelerator in PC systems. Generally, the addition of $CaCl_2$ can shorten initial setting times and increase the early strength of PC concretes. Due to these effects, $CaCl_2$ has been used on construction sites in cold weather regions. The effect of $CaCl_2$ on the CAS 4:4:2 binder is similar to that of $CaCl_2$ on PC systems. The difference lies in the ultimate compressive strength. In PC systems, $CaCl_2$ only enhances early compressive strength; in the CAS 4:4:2 binder, $CaCl_2$ enhanced both early and ultimate compressive strengths.

The primary role of $CaCl_2$ in the CAS 4:4:2 binder is to increase the solubility of raw materials. Evidence of this role includes: (1) increase in the hydration heat; (2) increase in the reactivity of raw materials and decrease in the amorphous hump, as shown in the XRD results; and (3) higher solubility of raw materials with $CaCl_2$-containing samples in the EDS results. Shi et al. [52, 67] pointed out that the key role of $CaCl_2$ in GGBFS/fly ash-blended systems is to increase the solubility of $Ca(OH)_2$. An identical reaction was also observed in the present study. According to the XRD and TG results, as greater amounts of $CaCl_2$ were added, $Ca(OH)_2$ gradually reduced. The similarity in behavior of the CaO-activated fly ash/slag systems could be attributed to the influences of $CaCl_2$ on strength development.

3.4. Chapter summary

This present study reports the beneficial effects of $CaCl_2$ as an additive activator on the binder properties of CaO-activated GGBFS blended with fly ash. The influence of $CaCl_2$ was studied using a compressive strength test, conduction calorimetry, a material cost estimation, XRD, TG/DTG, MIP, and SEM with EDS. The detailed conclusions are as follows.

(1) Despite using no cement compound in this study, the addition of $CaCl_2$ produced both a significant effect of acceleration on CAS 4:4:2 binders and a much greater strength at all curing days. In particular, the 3-day strengths of the samples with $CaCl_2$ were four to five times higher than those of the samples without $CaCl_2$ at all w/b ratios.

(2) The dosage increase of $CaCl_2$ up to 2% had a positive effect on strength increase. However, when $CaCl_2$ was used at 3%, no distinct strength increase (and even a slight decrease) was obtained regardless of w/b values, compared to that at 2%.

(3) The reactions of CAS 4:4:2 binders generated significantly lower cumulative heats up to 72 h, although their initial heats up to 10 h were notably higher, compared to the cumulative and initial heats of PC hydration. These high initial heats of CAS 4:4:2 might be advantageous in gaining high early strength.

(4) The estimation of material costs showed that CAS 4:4:2 binders were probably 6–14% less expensive than that of PC 4:4:2. Thus, in this study, 2CSF was favorably suggested as a price-competitive and strong binder among the tested binders.

(5) In XRD, C-S-H and portlandite were commonly identified in all the hardened samples. The most distinct mineralogical changes due to $CaCl_2$ addition were the formation of hydrocalumite and the removal of hydrotalcite and strätlingite. The XRD analysis also illustrated that the presence of $CaCl_2$ largely accelerated the dissolution of the glass phase of GGBFS and fly ash at early days.

(6) In every mixture, in the total weight losses up to 1,000 °C in TG, more weight was lost at 28 days, compared to that of 3 days, regardless of the dosage of $CaCl_2$; however, as the $CaCl_2$ content increased, the difference in the total weight loss between 3 and 28 days substantially decreased. At each day of curing, in all the measured samples, a greater $CaCl_2$ dosage tended to induce a higher total weight loss of the sample up to 1,000 °C. Thus, the use of $CaCl_2$ not only caused the acceleration of the reaction, but it also generated a greater quantity of reaction products.

(7) The MIP results displayed an overall trend in which the use of $CaCl_2$ not only contributed to the acceleration of pore-size refinement at the early stage of curing, but it also decreased the total porosity of the hardened sample, resulting in higher early and final compressive strengths.

(8) In the BSE images, the samples with $CaCl_2$ showed rather higher brightness, due to more densely filled matrices, than that of the sample without $CaCl_2$.

The EDS analysis revealed that a considerable degree of GGBFS dissolution occurred even at a 1% addition of $CaCl_2$; however, above a 2% addition, the GGBFS dissolution seemed to be much reduced. The results also indicated that although fly ash was not noticeably dissolved until the $CaCl_2$ content reached 2%, the use of $CaCl_2$ above 2% markedly promoted the dissolution of fly ash.

4. INFLUENCE OF CALCIUM AND SODIUM NITRATE ON THE STRENGTH AND REACTION PRODUCTS OF THE CAO-ACTIVATED GGBFS SYSTEM

4.1. Introduction

A vast amount of carbon dioxide (CO_2) is produced during the Portland cement (PC) manufacturing process, and it has been pointed out as a serious cause for accelerating global warming. For this reason, cementless binders have been developed to replace PC [74-77]. Ground granulated blast-furnace slag (GGBFS) is an industrial waste by-product from producing steel and often used as the main precursor material to produce cementless binders. The developed strength, durability, and production cost of the GGBFS-based cementless binders considerably depend on the type of chemical activators [72, 74, 75, 78]. Alkaline activators (e.g., NaOH, KOH, sodium silicate, etc.) are chemical activators that have been extensively used to produce GGBFS-based cementless binders (alkali-activated GGBFS). However, although these activators yield relatively high strength binders, their material costs are high, resulting in a low economic competence of cementless binders. In addition, these activators produce a very high pH (over ~14) when dissolved, making it difficult to use them in construction fields due to safety concerns [79, 80]. To avoid these major drawbacks of alkaline activators, Kim et al. [16] developed a CaO-activated GGBFS cementless binder that uses CaO as the main activator. CaO is more advantageous as it yields a relatively low pH (~13) when dissolved and is less expensive than alkaline activators.

Nevertheless, there have been concerns that CaO-activated GGBFS binders tend to produce significantly lower early strength compared to alkali-activated GGBFS binders. For this reason, it is essential to find add-on chemicals to increase the early strength of CaO-activated GGBFS binders. As such, Yum et al. [81] explored the use of $CaCl_2$ as an addition for CaO to increase the early strength of this binder system. This study showed that the use of $CaCl_2$ dissolved more of the glass phase of GGBFS and significantly enhanced the compressive strength at 3 and 28 days of curing. However, because chloride ions released from dissolving $CaCl_2$ may cause severe corrosion problems in reinforced concrete structures, particular attention should be placed on its use [40, 41]. Therefore, it is desirable to find novel chemical additives without chloride to increase the early strength of CaO-activated GGBFS binders.

Calcium nitrate ($Ca(NO_3)_2$) and sodium nitrate ($NaNO_3$) are well-known accelerators along with $CaCl_2$ for the hydration of PC [82, 83]. Although the PC system is significantly different than the CaO-activated GGBFS system, the $Ca(NO_3)_2$ and $NaNO_3$ nitrate salts may have potentially a beneficial effect on this cementless binder system because the main reaction product of CaO-activated GGBFS is

also calcium silicate hydrate (C-S-H), which is similar to PC. Therefore, in this study, due to the potential beneficial effects, the nitrate salts $Ca(NO_3)_2$ and $NaNO_3$ were investigated as chemical additives to increase the early strength of CaO-activated GGBFS binders, using the compressive strength test, measurement of the pH, powder X-ray diffraction (XRD), thermogravimetry (TG), and mercury intrusion porosimetry (MIP).

4.2. Experimental procedure

Analytical grade $Ca(NO_3)_2$ (Sigma Aldrich, USA), $NaNO_3$ (Sigma Aldrich, USA), and commercial GGBFS were used in this study. To examine the characteristics of GGBFS, particle size distribution (HELOS (HI199) and RODOS, Sympatec, Clausthal-Zellerfeld, Germany), X-ray fluorescence (XRF, S8 Tiger wavelength dispersive WDXRF spectrometer, Bruker, Billerica, MA, USA), and XRD (Cu-Kα, λ = 1.5418Å, D/Max2500V/PC, Rigaku, Japan) were examined. **Figure 4.1** shows the particle size distribution of the GGBFS. The median particle size of the GGBFS was approximately 11 μm, which is similar to the normal GGBFS [4]. Then, the XRF and XRD measurements showed that the GGBFS consisted mostly out of CaO, SiO_2 (**Table 4.1**), and an amorphous phase (**Figure 4.2**). The loss of ignition (LOI) of GGBFS was examined up to 1,000°C using a thermal analyzer (SDT Q600, TA Instruments, New Castle, DE, USA) with alumina pans and reported a 0.8 weight percent (wt%) of LOI.

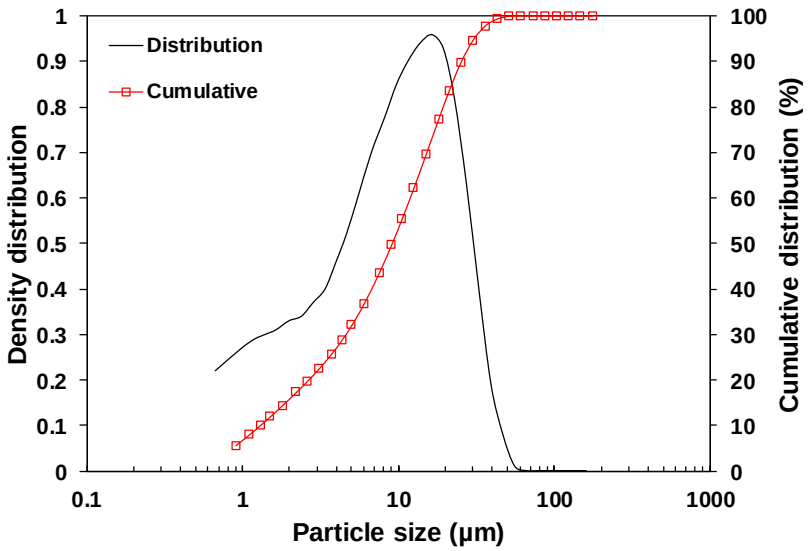

Figure 4.1 Particle size distribution of GGBFS

Table 4.1 Chemical oxide composition of GGBFS

Oxide	wt%
CaO	44.78
SiO_2	34.28
Al_2O_3	13.18
MgO	3.48
SO_3	1.75
TiO_2	0.67
Fe_2O_3	0.51
K_2O	0.48
MnO	0.34
Na_2O	0.29
Other	0.24

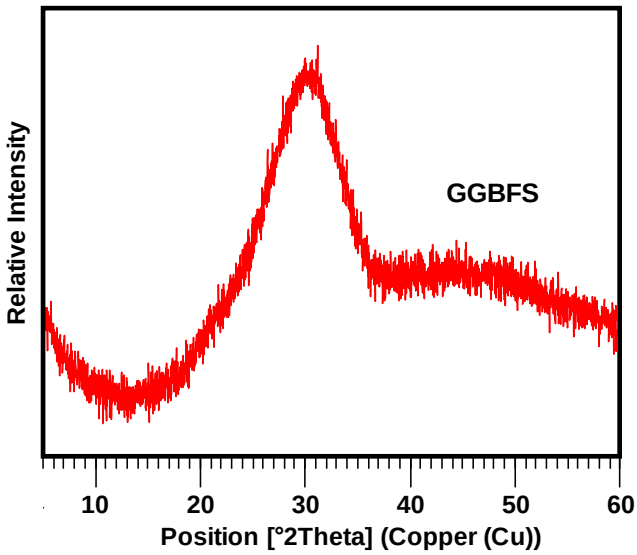

Figure 4.2 XRD pattern of GGBFS

After characterizing the commercial GGBFS, the mixture proportions of the paste samples with $Ca(NO_3)_2$ or $NaNO_3$ were prepared. The amount of main activator (CaO) was fixed at 4 wt%, and the $Ca(NO_3)_2$ or $NaNO_3$ were used as a 0.5, 1.3, or 5 wt% substitution of the GGBFS. All samples were prepared with a water-to-binder weight ratio (w/b) of 0.35 (**Table 4.2**).

Table 4.2 The mixture proportions and replacement percentage of each additional chemical of the paste samples (wt%)

Group label	Sample label	Binder					w/b
		GGBFS	CaO	Nitrate salts		Sum	
				$Ca(NO_3)_2$	$NaNO_3$		
Control	Control	96.0	4.0	0.0	0.0	100	0.35
CN	0.5CN	95.5	4.0	0.5	0.0	100	
	1CN	95.0		1.0		100	
	3CN	93.0		3.0		100	
	5CN	91.0		5.0		100	
SN	0.5SN	95.5		0.0	0.5	100	
	1SN	95.0			1.0	100	
	3SN	93.0			3.0	100	
	5SN	91.0			5.0	100	

Abbreviations: calcium nitrate (CN) and sodium nitrate (SN).

The raw powder materials GGBFS, CaO, $Ca(NO_3)_2$, and $NaNO_3$ were dry mixed for 5 min, followed by the addition of deionized water and further mixing. All mixing procedures followed the guidelines of the American Society for Testing and Materials (ASTM) C305 [84]. The fresh pastes were cast in cubic molds (5 × 5 × 5 cm) and cylindrical molds (φ2.54 cm × 2.54 cm) for compressive strength tests and MIP tests, respectively. All samples were cured at a constant temperature of ~23°C and a relative humidity of 99% until used for testing.

Compressive strength tests were conducted at days 3, 7, and 28 of curing, and the average values of triplicate samples determined. After the compressive strength tests, fractured samples were collected and finely ground for the TG and XRD tests. A hydration-stop procedure was carried out using a solvent-exchange method with isopropanol and vacuum drying to prevent further hydration [21].

Diluted paste samples were prepared to measure their pH values using the same mixture proportions of the control, 1CN (sample containing $Ca(NO_3)_2$), and 1SN (samples containing $NaNO_3$) as shown in **Table 4.2**—with the exception that the w/b ratio was increased to 3. A pH meter (HI 3320, Hanna Instruments INC., Italy) was used to measure the pH of the diluted paste samples. The pH values were measured every 24 hours for the first 3 days after making the binder mixture. The diluted pastes were agitated with magnetic stirrers until the end of the experiment to prevent solidification.

The XRD patterns of the hardened samples were obtained using a high-power powder X-ray diffractometer (D/Max2500V/PC, Rigaku, Japan) with Cu-Kα radiation (λ = 1.5418Å) within a range of 5–60° at 2θ. The measured XRD patterns were analyzed using the X'pert HighScore Plus software [57] with the International Centre for Diffraction Data (ICDD) PDF-2 database [85] and the Inorganic Crystal Structure Database (ICSD) [58].

The TG measurement was performed using a thermal analyzer (SDT Q600, TA Instruments, New Castle, DE, USA) with alumina pans. The range of the heating temperature was set from 30°C to 1,000°C with a heating rate of 10°C/min in a nitrogen gas environment.

The pore size distributions of hardened samples were measured with the mercury intrusion porosimetry (MIP (Auto pore IV 9500, Micrometrics Instrument Co., GA, USA)). A sample volume of 125 mm^3 (5 × 5 × 5 mm) was used. Five identical samples were used to increase the reliability of the results and were immersed in isopropanol until testing.

4.3. Results and discussion

4.3.1. Compressive strength

The compressive strength results are shown with the inset tables in **Figure 4.3**. All samples containing $Ca(NO_3)_2$ (CN group) showed an increase of strength for all days compared to the control ones (**Figure 4.3 (a)**). The 28-day curing samples showed an increase of 8.4–20% in strength depending on the amount of $Ca(NO_3)_2$ added. For the strength measurements on 3 days of curing, the strength was almost doubled for all samples compared to the control. When using only 0.5 wt% $Ca(NO_3)_2$, the resulting strength on day 3 was nearly twice that of the control. It is worth noting that despite the absence of dicalcium silicate and tricalcium aluminate [86], which are necessary in triggering the accelerating action of nitrate salts for PC, the use of $Ca(NO_3)_2$ still accelerated the strength gain in the CaO-activated GGBFS binder.

In addition, the addition of $NaNO_3$ (SN group) was evaluated for its strength changing properties (**Figure 4.3 (b)**). The results showed that $NaNO_3$ behaved with a more complex tendency compared to $Ca(NO_3)_2$ as an additive. For instance, while $NaNO_3$ also acted as an accelerator—given that the strength of the samples on 3 days was largely increased after its addition—similar to $Ca(NO_3)_2$, its increasing effect started to decline when used at 1 wt% or higher. However, on 28 days of curing, all samples with $NaNO_3$ produced lower strengths than the control. This effect was in proportion to the weight of $NaNO_3$. Thus, the effect of nitrate salts on the CaO-activated GGBFS system was significantly dependent on the type of cation ($Ca(NO_3)_2$ vs. $NaNO_3$). Thus, the use of $Ca(NO_3)_2$ seemed to be more advantageous in the CaO-activated GGBFS system for improving the strength of the binder at all days compared to the addition of $NaNO_3$.

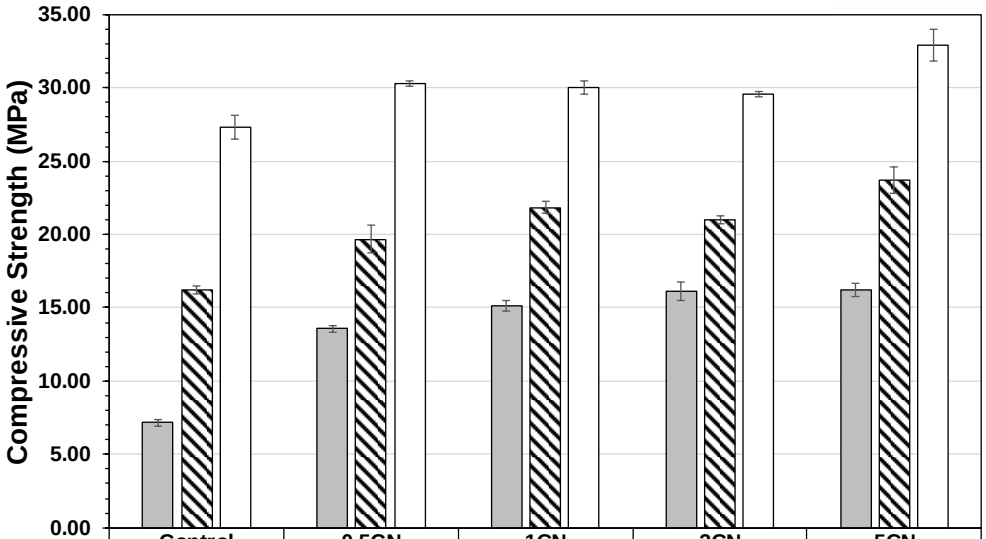

	Control	0.5CN	1CN	3CN	5CN
3 days	7.15	13.57	15.12	16.14	16.19
7 days	16.25	19.69	21.84	21.00	23.72
28 days	27.30	30.31	30.02	29.58	32.92

(a)

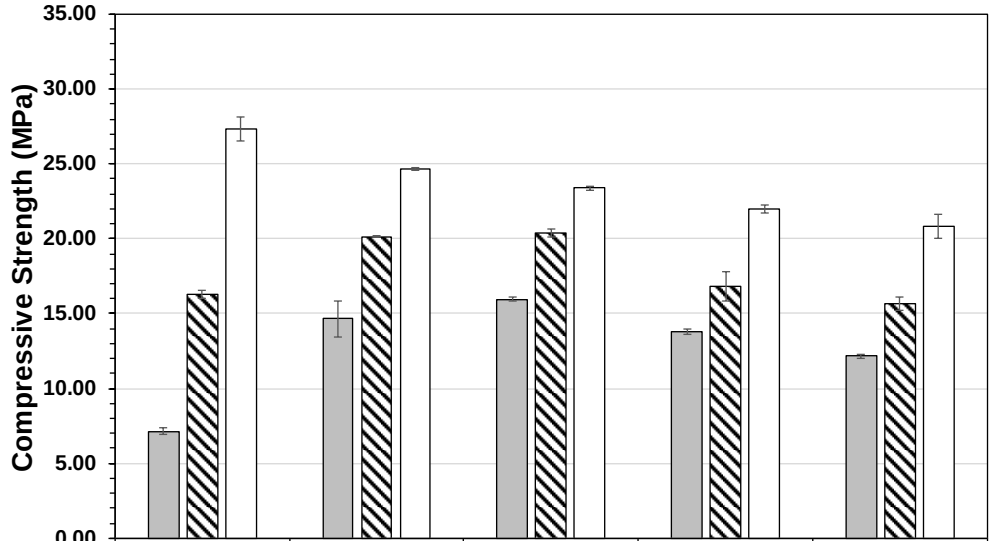

	Control	0.5SN	1SN	3SN	5SN
3 days	7.15	14.65	15.95	13.78	12.14
7 days	16.25	20.15	20.36	16.81	15.67
28 days	27.30	24.68	23.37	21.97	20.87

(b)

Figure 4.3 Compressive strength analysis of various binder mixtures with $Ca(NO_3)_2$ and $NaNO_3$ additions. (a) Represents the $Ca(NO_3)_2$ (CN) group against the control one. (b) Represents the $NaNO_3$ (SN) group against the control one

4.3.2. Measurement results of the pH levels

The pH is closely related to the development of strength in cementless binder systems (e.g., alkali- or CaO-activated GGBFSs). A higher pH dissolves more of the glass phase of raw materials (e.g., GGBFS and fly ash), resulting in the generation of more Ca, Si, or Al ions, which are necessary for developing strength by forming the reaction products such as C-S-H [69, 87]. As such, the pH values of the control, 1CN, and 1SN were measured during the first 3 days using diluted paste samples (**Figure 4.4**). From these results, the highest pH was found with the 1SN mixture. Considering that when $NaNO_3$ is present, which generally increases the solubility of $Ca(OH)_2$ in aqueous salt solutions [88], the higher pH of 1SN was likely obtained due to the increased amount of dissolving the $Ca(OH)_2$. As such, it is likely that the glass phase of GGBFS was more dissolved in 1SN samples within those 3 days due to the high pH. This results in the production of more reaction products, and consequently, the greater strength among samples.

For the 1CN samples, the additional supply of calcium ions from the added $Ca(NO_3)_2$ probably induced a common ion effect [89], which suppressed the solubility of $Ca(OH)_2$, and thus, slightly reduced the pH. While in general, a high pH is helpful to gain a high strength in cementless binders, this effect was not seen for the 1CN samples compared to the control. However, even though 1CN showed the lowest pH value for all 3 days, it produced a significantly higher strength than the control. To support this effect, it is worth noting that Bellman et al. [47] demonstrated that GGBFS was still effectively activated at a lower pH (~12) by simply increasing the concentration of calcium ions in the pore solutions by adding a small amount of soluble calcium salts (e.g., 3 wt% of $Ca(NO_3)_2$), which resulted in a significant improvement in strength development. Therefore, the strength improvement of 1CN was likely achieved similarly compared to the study of Bellman et al. [47].

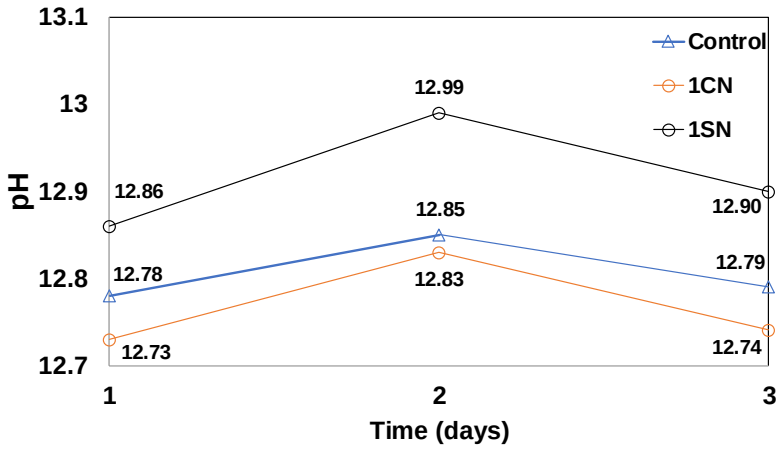

Figure 4.4 The change of pH of diluted paste samples during the first 3 days

4.3.3. XRD analysis

The XRD patterns of hardened samples are provided with the reference patterns of the identified phases in **Figure 4.5.** The type of reaction products analyzed with the XRD was very similar between the CN and SN group when the same weight of salts was used, although their compressive strengths were significantly different. Additionally, there was no difference in the type of reaction products for all samples between 3 and 28 days of curing.

C-S-H [90] and akermanite ($Ca_2Mg(Si_2O_7)$) were identified in all samples. Portlandite ($Ca(OH)_2$) was observed in all samples with less than 3–5 wt% of $Ca(NO_3)_2$. In a few samples containing more than 3 wt% of $Ca(NO_3)_2$ or $NaNO_3$ (e.g., 3CN at 3 days of curing or 5SN at 28 days of curing), calcite ($CaCO_3$) was formed, possibly due to the carbonation of portlandite with the atmospheric CO_2 during the curing process [15, 91, 92]. An Al_2O_3-Fe_2O_3-mono (AFm) phase was also clearly identified in the samples containing any type of nitrate salts with more than 3 wt%. This seemed to occur mainly when the quantity of salts was at 5 wt%, causing the XRD peaks of this phase to increase significantly. The ICDD PDF-2 database indicates that this AFm phase in our study was nitrate (NO_3) AFm ($Ca_4Al_2(OH)_{12}(NO_3)_2{\cdot}4H_2O$) [93]. According to other previous studies [94, 95], this phase could also be a nitrite (NO_2) AFm ($Ca_4Al_2(OH)_{12}(NO_2)_2{\cdot}4H_2O$) phase or a mixture of NO_3- and NO_2-AFm phases. This could be possible because when NO_3-AFm loses water during the drying processes (e.g., using a vacuum desiccator for sample preparation in this study), the XRD pattern dried, and the NO_3-AFm phase may become similar to that of the NO_2-AFm one [94].

In the CN group, regardless of curing days, weaker peaks of portlandite were identified when more $Ca(NO_3)_2$ was used as a substitution. Indeed, portlandite was not identified in the 3CN and 5CN samples. However, unlike the CN group, portlandite was clearly identified in all SN group samples during all days of curing.

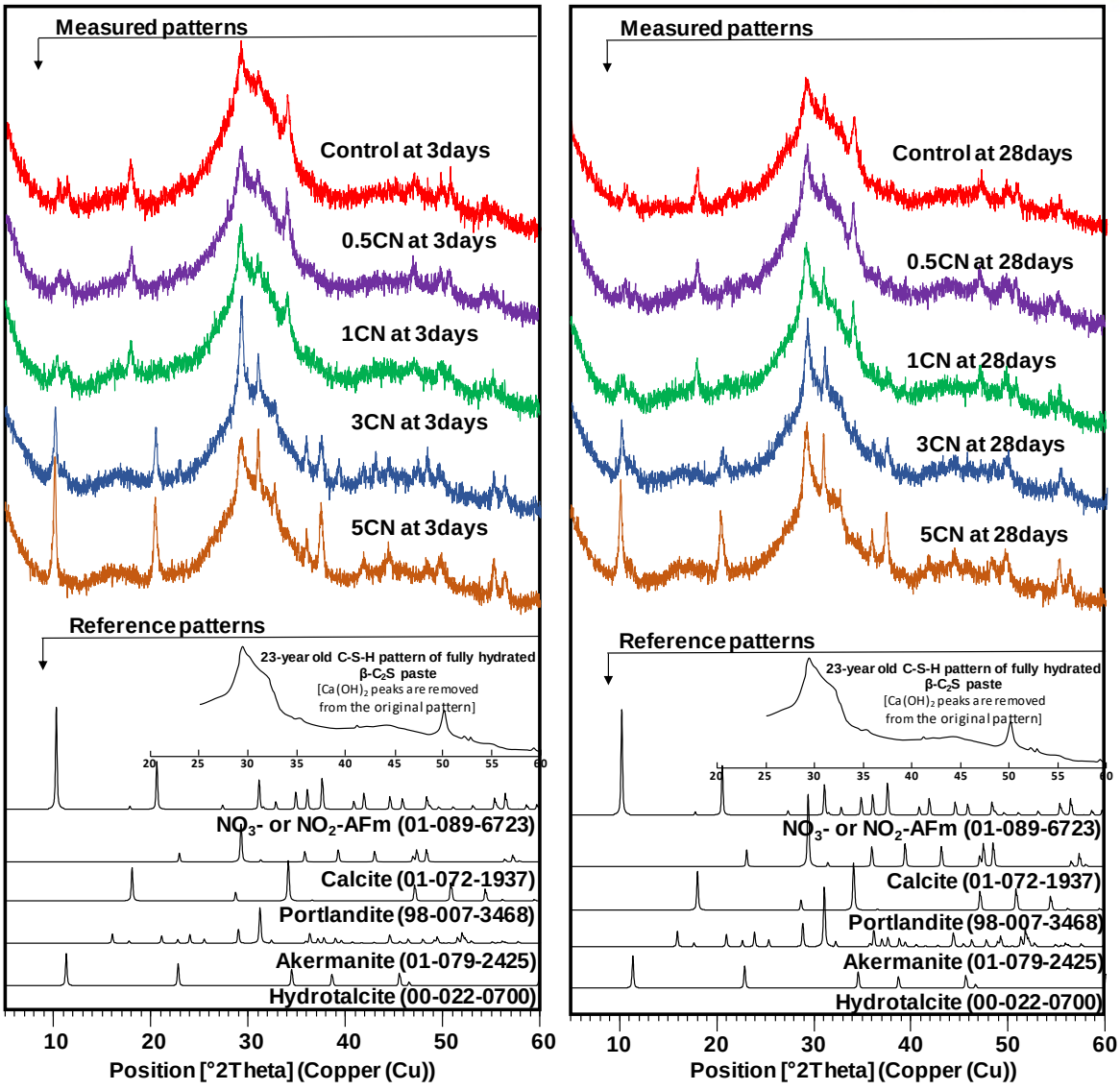

(a) (b)

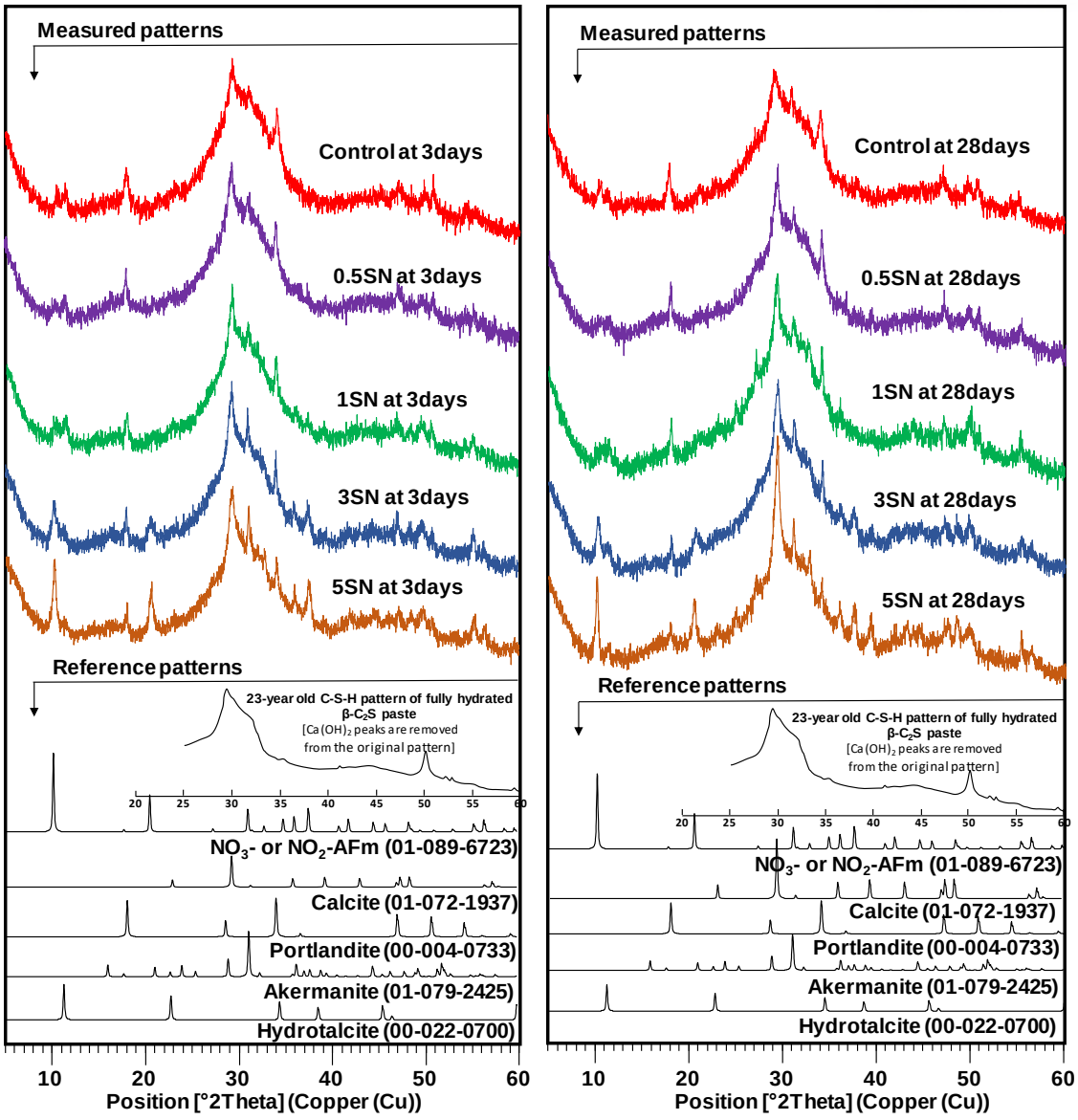

(c) (d)

Figure 4.5 XRD patterns of hardened samples. The investigated samples were as follows: (a) the CN group on day 3, (b) the CN group on day 28, (c) the SN group on day 3, and (d) the SN group on day 28. The numbers in brackets indicate the reference numbers of identified phases in the ICDD PDF-2 database. Note that the reference pattern of C-S-H was obtained from [96] after removing the reflections of calcium hydroxide

4.3.4. TG/DTG

The results from the TG/DTG tests are illustrated in **Figure 4.6**. For all samples, the decomposition of C-S-H, NO_3- and/or NO_2-AFm, $Ca(OH)_2$, and calcite was identified [27, 95]. Overall, the TG/DTG results were consistent with the XRD results regarding the phase identification of reaction products. In **Figure 4.6**, each figure illustrates that for each group (CN or SN) on the same day of curing, the total weight loss until 1,000°C was noticeably increased with TG. This occurred because a higher amount of nitrate salts was used. Additionally, given that the raw GGBFS in this study barely showed a weight loss until 1,000°C with the TG (i.e., LOI = ~0.8 wt%), the increase of the total weight loss indirectly suggests that more nitrate salts resulted in more GGBFS due to an increase of it dissolving. This occurred because the formation of more reaction products required a larger supply of vital elements (e.g., Si, Al), which are generated only from GGBFS in this study.

In both the CN and SN groups (**Figure 4.6)**, the weight losses below 200°C were mainly due to thermal decompositions of C-S-H, which is a core phase to develop strength, and AFm phases (NO_3- and/or NO_2-AFm). However, given that very little or no NO_3/NO_2-AFm phases were found in XRD for all days, when $Ca(NO_3)_2$ or $NaNO_3$ was replaced up to 1 wt%, in the samples with 0–1 wt% of nitrate salts (i.e., 0.5CN, 1CN, 0.5SN, and 1SN), the DTG peaks below 200°C were mainly due to the dehydration of C-S-H. At 3 days of curing, the weight loss of C-S-H in the samples of both groups clearly increased as the quantity of nitrate salts increased. These results support that the use of nitrate salts—regardless of the type of cation of the salts—was clearly beneficial to produce C-S-H (up to 1 wt%). Then, at 28 days, the quantity of nitrate salts increased (up to 1 wt%). Here, the CN group samples did not show any decrease of the DTG peak that indicates C-S-H levels; however, the SN group samples did clearly display a reduction of C-S-H based on the DTG peak (see the area with the shading lines in the enlarged figure in **Figure 4.6 (d)**). Thus, the effect of using $NaNO_3$ was changed from being advantageous (at 3 days) to detrimental (at 28 days) for developing strength as the curing process progressed.

In general, NO_3- and NO_2-AFm phases have their thermal decompositions in similar temperature ranges of 0–150°C, 200–300°C, 400–600°C, and near 700°C in TG [94, 95]; the weight losses occur through the progressive reduction of water (H_2O), hydroxyl (OH) groups, nitrate (NO_3), and nitrite (NO_2) or combination of these reductions.

In this study, the DTG peak was around 250°C, which was an isolated DTG peak of NO_3- and NO_2-AFm phases from the DTG peaks of other reaction products, and gradually increased as more nitrate salts were used. For this reason, the substitution of nitrate salts was likely the main cause for the formation of NO_3- and/or NO_2-AFm phases.

With temperatures of 400–600°C during the TG, along with dehydroxylation of the OH groups, the reduction of NO_2 was the main cause of weight loss for the NO_3- and NO_2-AFm phases [94, 95]. To

be more exact, the major weight loss of NO_2-AFm occurred near 450°C (see the ● in **Figure 4.6**) and near 580°C for NO_3-AFm (see the ♦ in **Figure 4.6**), which was found previously as well [94]. Additionally, unlike the samples with nitrate salts of up to 3 wt%, the 5 wt% samples showed a significant increase of the DTG peak near 450°C, regardless of the nitrate salt type or days of curing. This was especially the case for 5SN on day 28 of curing, showing a large DTG peak (the gray area in the 400–580°C range, (see **Figure 4.6 (d)**). Next, three identically repeated samples were executed to rule out a potential experimental error to confirm this large DTG peak; however, all the repeated samples further confirmed the initial result. Therefore, it is more likely that the use of nitrate salts with more than 5 wt% increased the formation of the NO_2-AFm—with a higher intensive especially for the SN group—rather than the NO_3-AFm.

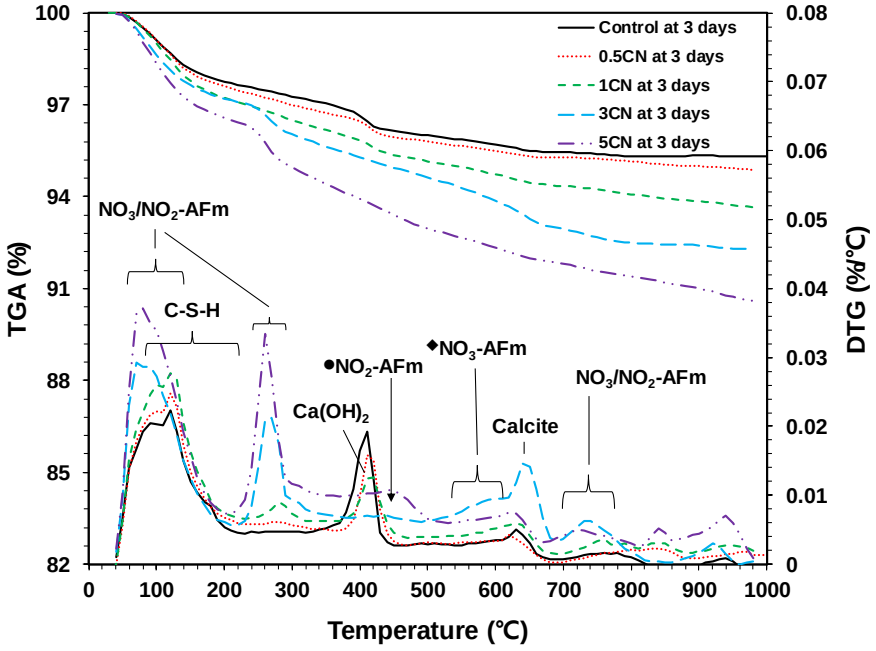

(a)

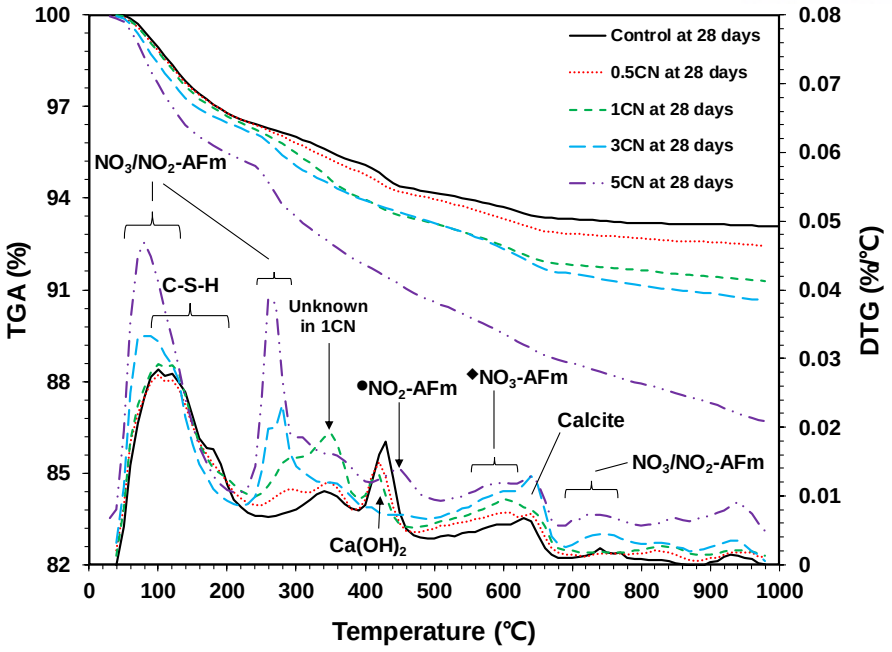

(b)

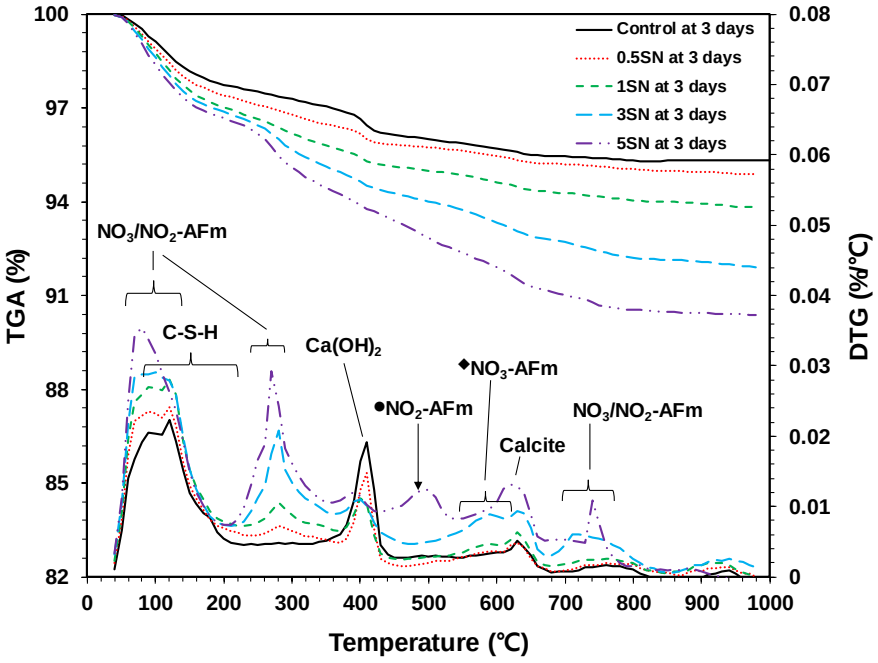

(c)

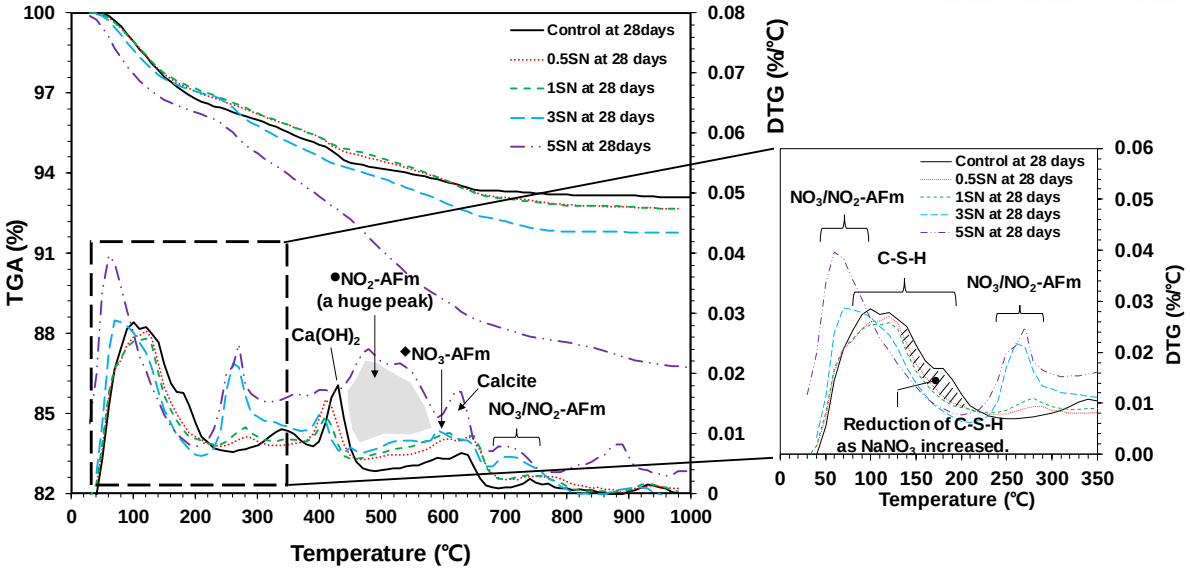

(d)

Figure 4.6 TG/DTG results of hardened samples during various curing days. The following conditions were investigated: (a) the CN group on day 3, (b) the CN group on day 28, (c) the SN group on day 3, and (d) the SN group that shows an enlarged window of the 0–350°C range on day 28

4.3.5. MIP

The MIP results of hardened samples with the total porosities are shown in **Table 4.3** and **Figure 4.7**. In general, the strength of a hardened cementitious paste is inversely proportional to its total porosity and overall pore size. More importantly, pores larger than 0.05 μm are generally much less detrimental to the binder strength than pores smaller than 0.05 μm [4]. In this study, as curing days passed, all samples in each group largely lost their pores larger than 0.05 μm, resulting in the reduction of the average pore size, from 3 to 28 days. As a result, the strength of all samples was largely improved with additional curing days.

Further investigation of the pore size distribution showed that it was significantly dependent on the cation type of the nitrate salts. For instance, in the CN group, regardless of the curing days, the shape of the distribution curves were roughly grouped in two curve forms, depending on the amount of $Ca(NO_3)_2$ present (see the inset figures in **Figure 4.7 (a)**). These results show that when $Ca(NO_3)_2$ increased from 0 to 1 wt%, the curve gradually contracted in a similar form of the curve shape. When the dosage was over 3 to 5 wt%, the distribution curve was significantly altered due to the considerable reduction of pores smaller than 0.05 μm. As opposed to the CN group, the curve shape of the SN group was not significantly changed by the dosage of $NaNO_3$, and changes of the overall pore size and total porosity were minimal. Taken together, it was not appropriate to simply compare the values of total porosity or average pore size between the CN and SN groups to explain the different strengths of them.

In the CN group, although the curve shape of the pore size distribution was largely affected by the quantity of $Ca(NO_3)_2$, the total porosity was not notably affected during all curing days (except 0.5CN). For example, the 1CN and 3CN samples showed similar values for the total porosity on all days of curing but noticeably different ones for their size distributions. Consequently, given that the strength values were very similar between all samples at every same day of the curing, the relationship between strength and pore size distribution in the CN group was difficult to interpret accurately.

In the SN group, at 3 days of curing, the 1SN sample showed the lowest level of porosity with an average pore size among samples. This was in accordance with its results concerning the strength, which was the strongest among the SN group. Nonetheless, at 28 days of curing, the strengths of the SN group samples were contradictorily lower than that of the control, despite showing a smaller value for the total porosities. This cause can be seen in the curves by the shift in distribution to the right, which represents a smaller pore size, with higher weights of $NaNO_3$. In sum, these results show that the average pore size was more important than the total porosity in determining the strength of the SN group at 28 days of curing.

Table 4.3 Total porosity and average pore size of hardened samples

Group label	Sample label	Curing days (3 days)		Curing days (28 days)	
		Total porosity (%)	Average pore size (nm)	Total porosity (%)	Average pore size (nm)
CN	Control	39.45	27.5	38.51	16.2
	0.5CN	39.29	26.6	34.23	17.0
	1CN	34.62	23.9	34.54	15.9
	3CN	34.86	23.3	33.06	15.8
	5CN	34.73	19.8	32.58	14.4
SN	Control	39.45	27.5	38.51	16.2
	0.5SN	34.41	29.1	36.58	19.5
	1SN	33.84	23.9	33.87	20.7
	3SN	35.75	24.0	34.25	21.6
	5SN	36.48	24.9	37.88	20.0

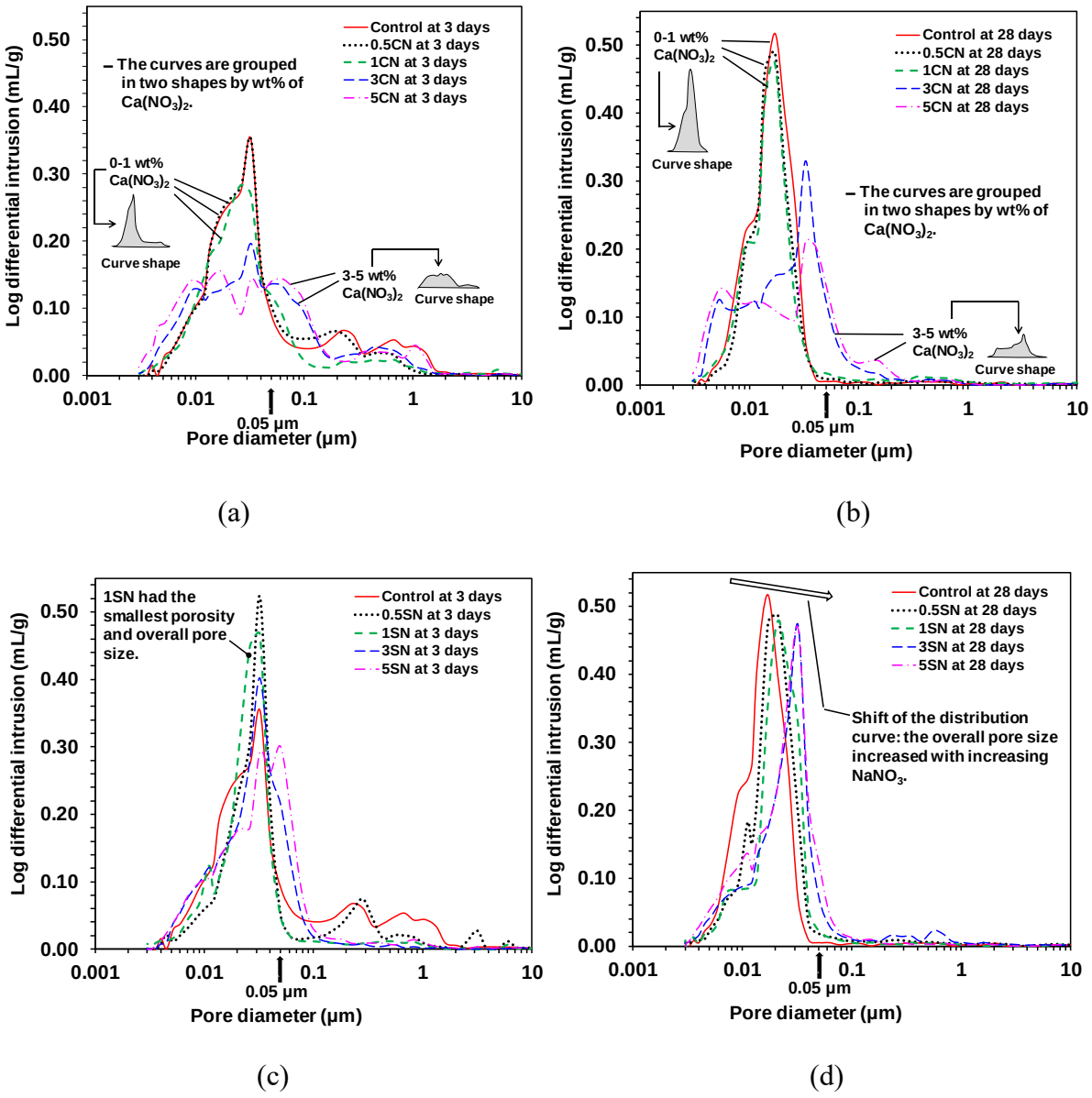

Figure 4.7 The MIP results of hardened during various curing days. The following conditions were investigated: (a) the CN group on day 3, (b) the CN group on day 28, (c) the SN group on day 3, and (d) the SN group on day 28

4.4. Chapter summary

In this study, the influence of the nitrate salts $Ca(NO_3)_2$ and $NaNO_3$ on the CaO-activated GGBFS system were investigated. The addition of each nitrate salt was found clearly beneficial in developing strength during the early days of curing. The results showed that on day 3 of curing, the strengths were almost doubled for all samples, regardless of the cation type of the nitrate salts. However, a difference between the nitrate salts was seen on day 28 of curing, where the added $Ca(NO_3)_2$ was still

effective in increasing the cementless binder's strength compared to the control (without any nitrate salts), the added $NaNO_3$ was not anymore.

The analysis of pH showed that the use of $NaNO_3$ increased the pH of the paste samples, resulting in the increase of strength due to the increase of dissolving GGBFS, which increases the solubility of $Ca(OH)_2$ in the pore solution during the early days (e.g., before 3 days). In turn, the additional solubility of $Ca(OH)_2$ caused a decrease in the sample's pH due to the common ion effect. For the $Ca(NO_3)_2$ samples, the addition of $Ca(NO_3)_2$ also provided an additional supply of calcium ions, causing a pH decrease. However, $Ca(NO_3)_2$ still improved the strength of the samples during the early days of curing.

The types of reaction products were very similar in all samples when the same weight of salts was used, regardless of the type of nitrate salt or days of curing.

C-S-H was the main phase that improved the binder's strength development in this study. On day 3 of curing, the use of nitrate salts was clearly beneficial to produce C-S-H, regardless of the cation type in the salts. On day 28 of curing, however, the samples with $NaNO_3$ clearly displayed a reduction of C-S-H when the weight of the salt increased, which was not the case for the $Ca(NO_3)_2$ samples. This changed the advantageous use of $NaNO_3$ on day 3 of curing for the developing strength during the curing process into a detrimental one on day 28.

The NO_3- and/or NO_2-AFm phases were significantly generated when nitrate salts replaced 3–5 wt% of the total mixture weight. At 3 wt% for both nitrate salts, the NO_3-AFm phase was most likely more produced, while at 5 wt%, the NO_2-AFm phase seemed to be more produced.

In this study, all samples mostly lost their pores larger than 0.05 μm as curing days passed (from 3 to 28 days), resulting in the reduction of the average pore size and the improvement of their strength. However, the pore size distribution was significantly dependent on the cation type of nitrate salts. The shape of the distribution curves of the samples with $Ca(NO_3)_2$ were roughly grouped in two curve shapes depending on the quantity of $Ca(NO_3)_2$, while those of the $NaNO_3$ samples were not significantly changed by the dosage of $NaNO_3$.

5. STRENGTH ENHANCEMENT OF CAO-ACTIVATED GGBFS BINDER THROUGH ADDITION OF CALCIUM FORMATE AS A NEW AUXILIARY ACTIVATOR

5.1. Introduction

Ground granulated blast furnace slag (GGBFS) is an industrial waste by-product of the steel manufacturing process. GGBFS is commonly used as a supplementary cementitious material in the production of Portland cement (PC) concrete, as it provides many benefits for concrete production, such as reducing production cost, lowering hydration heat generation, and enhancing long-term strength and durability [97]. More importantly, GGBFS has been actively investigated as a precursor material for producing alternative structural cementless binders through activation using alkaline activators (e.g., NaOH, Na_2SiO_3) [31, 47, 75, 98], or $Ca(OH)_2$ [69, 72, 99].

The mechanical properties (e.g., compressive strength) of GGBFS-based cementless binders are significantly influenced by the type of activators. Various types of activators have been studied; however, (1) their toxicity due to high pH (> 14) (e.g., NaOH, Na_2SiO_3), (2) low early strength (e.g., $Ca(OH)_2$, $Ba(OH)_2$), and (3) high material costs (e.g., NaOH, Na_2SiO_3, $Ba(OH)_2$) have been pointed out as difficult problems to overcome for their practical application.

Recently, the use of CaO was investigated for GGBFS activation to produce a strong cementless binder [16]. It is an affordable activator (e.g., 1/3 to 1/7 of the material cost of NaOH) with a relatively low pH (= ~12.5) in its saturated solution and produces a comparable mechanical strength to that of PC at 28 days.

However, the low early strength of CaO-activated GGBFS has been considered to be an obstacle in field applications. Yum et al. [81] studied the addition of $CaCl_2$ as an auxiliary activator to enhance the early strength of the CaO-activated GGBFS. In the study, the addition of $CaCl_2$ significantly increased the early and 28-day strengths of the CaO-activated GGBFS. However, although the use of $CaCl_2$ was considerably beneficial in increasing the strength of the CaO-activated GGBFS system, special attention must be paid to its use because chloride ions generally have caused serious corrosion problems in concrete. Due to corrosion problems, the American Concrete Institute (ACI) has specified the maximum allowable quantity of $CaCl_2$ for different types of concrete structures [41]. Thus, for a wider range of applications of CaO-activated GGBFS, it is necessary to find a new type of auxiliary activator to replace $CaCl_2$ for boosting strength without any corrosion problems.

Calcium formate ($Ca(HCOO)_2$) (CF) is a well-known accelerator for cement hydration along with $CaCl_2$ [64, 90, 100]. However, CF has less efficient acceleration because its solubility in water is much lower than that of $CaCl_2$, and thus, a considerably higher dosage of CF, compared to $CaCl_2$, is

required for cement. Nevertheless, as no chloride is included in CF, the use of CF is more desirable than $CaCl_2$ when corrosion problems are significant in the concrete.

Therefore, in this study, CF was introduced as a new auxiliary activator in the CaO-activated GGBFS system to verify its effect on strength development and microstructure. To this end, compressive strength testing, powder X-ray diffraction (XRD), thermogravimetry (TG), and mercury intrusion porosimetry (MIP) were conducted.

5.2. Experimental procedures

Commercial GGBFS and analytical grade CaO (Daejung chemicals, Korea) along with $Ca(OOCH)_2$ (Aladdin, China) were used in this study. Particle size distributions (HELOS (HI199) and RODOS, Sympatec, Clausthal-Zellerfeld, Germany), XRD (D/Max2500V/PC, Rigaku, Japan) with Cu-Kα radiation (λ = 1.5418 Å), and X-ray fluorescence (XRF) (S8 Tiger wavelength dispersive WDXRF spectrometer, Bruker, Billerica, Ma, USA) were performed to examine the characteristics of the GGFBS. **Figure 5.1** shows the particle size distributions of GGBFS, and its median particle size was about 15 μm.

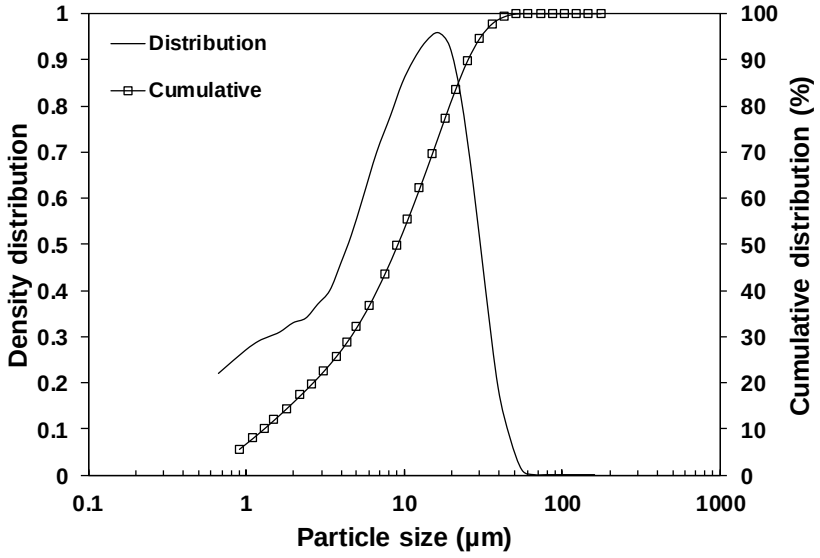

Figure 5.1 Particle distribution of GGBFS

The results of the XRF and XRD of the raw GGBFS are shown in **Table 5.1** and **Figure 5.2**, respectively. As a result of XRD analysis, akermanite ($Ca_2Mg(Si_2O_7)$) was identified, and it was determined that GGBFS was mostly composed of the amorphous phase (see the hump at ~24–35° in **Figure 5.2**). XRF analysis found that the major chemical composition of GGBFS consisted of CaO, SiO_2, and Al_2O_3.

Table 5.1 Chemical composition of GGBFS

Oxide	wt%
CaO	44.78
SiO_2	34.28
Al_2O_3	13.18
MgO	3.48
SO_3	1.75
TiO_2	0.67
Fe_2O_3	0.51
K_2O	0.48
MnO	0.34
Na_2O	0.29
Other	0.24

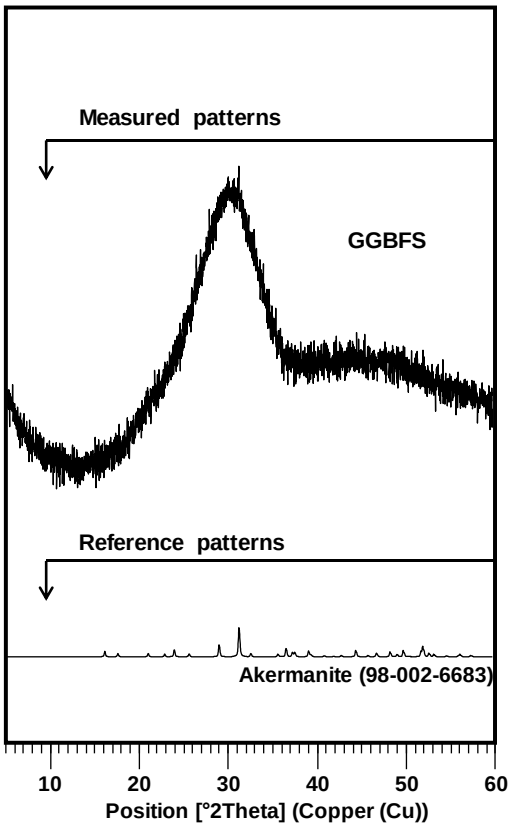

Figure 5.2 XRD pattern of GGBFS

Mixture proportions are given in **Table 5.2.** The quantity of the main activator (i.e., CaO) was fixed at 4 wt%, and GGBFS was replaced with an additional activator (i.e., CF) at 0, 1, 3, and 5 wt%. The number given in the sample label represents the replacement ratio of CF; for instance, 3CFCS

indicates that 3% CF was substituted. All the samples were prepared at a water-to-binder weight ratio (w/b) of 0.35.

Table 5.2 Mixture proportions (wt%)

Sample label	GGBFS	CaO	CF	w/b
0CFCS	96	4	0	0.35
1CFCS	95		1	
3CFCS	93		3	
5CFCS	91		5	

* Abbreviations: GGBFS = ground granulated blast furnace slag; CF = calcium formate; w/b = water-to-binder-weight ratio

GGBFS, CaO, and CF were dry mixed for 5 min and then additionally mixed with deionized water. All mixing procedures followed American Society for Testing and Material (ASTM) C 305 [84]. The fresh pastes were cast in cubic molds (5 × 5 × 5 cm) for compressive strength tests and in cylindrical molds (φ2.54 cm × 2.54 cm) for MIP tests. To remove entrapped air voids, the cast paste samples were manually compacted and then cured at a constant temperature, ~23°C, and 99% relative humidity until testing days. Compressive strength tests were carried out at 3, 7, and 28 days, and the average values for triplicate samples were used.

After compressive strength tests, fractured samples were collected and finely ground for the TG and XRD tests. A hydration-stop procedure was carried out using a solvent-exchange method with isopropanol and vacuum drying to prevent further hydration reactions [21].

To analyze the pore size distributions of hardened samples at 3 and 28 days, MIP (AutoPore IV 9500, Micrometrics Instrument Co., Georgia, USA) was used. A sample volume of 125 mm^3 (5 × 5 × 5 mm) was used, and the samples were immersed in isopropanol until tested.

The XRD patterns of the hardened samples were taken using a high-power powder X-ray diffractometer (D/Max2500V/PC, Rigaku, Japan) with Cu-Kα radiation (λ = 1.5418Å) within a range of 5–60° in 2θ. The measured XRD patterns were analyzed using the X'pert HighScore Plus software [57] with the International Centre for Diffraction Data (ICDD) PDF-2 database [58] and the Inorganic Crystal Structure Database (ICSD) [85].

The TG experiments were conducted for the 3-day and 28-day cured samples to investigate the reaction products using a SDT Q600 (TA Instruments, New Castle, DE, USA) with a heating rate of 30°C/min from 30°C to 1,000°C under a nitrogen atmosphere with an alumina pan.

5.3. Results and discussions

5.3.1. Compressive strength

Figure 5.3 shows the compressive strength results of hardened paste samples. Similar to the use of $CaCl_2$ [81], the presence of CF significantly increased the strength of CaO-activated GGBFS binder when compared to the sample without CF (e.g., 1.3–2 times at 3 days and 1.1–1.4 times at 28 days), and the extent of CF's strength enhancement was comparable to that of $CaCl_2$. Among the samples with CF, the highest compressive strength was achieved at 3 wt% of CF (i.e., 3CFCS), which will be discussed further in the later sections. Thus, CF played the role of accelerator as well as that of strength enhancer.

It is worth noting that, for strength enhancement, although the effect of CF in this study was similar to that of CF in the cement system, the mechanisms of CF action seem to be completely different because there was no $3CaO{\cdot}Al_2O_3$ (C_3A) in this study, which is generally required for CF to accelerate PC hydration [100].

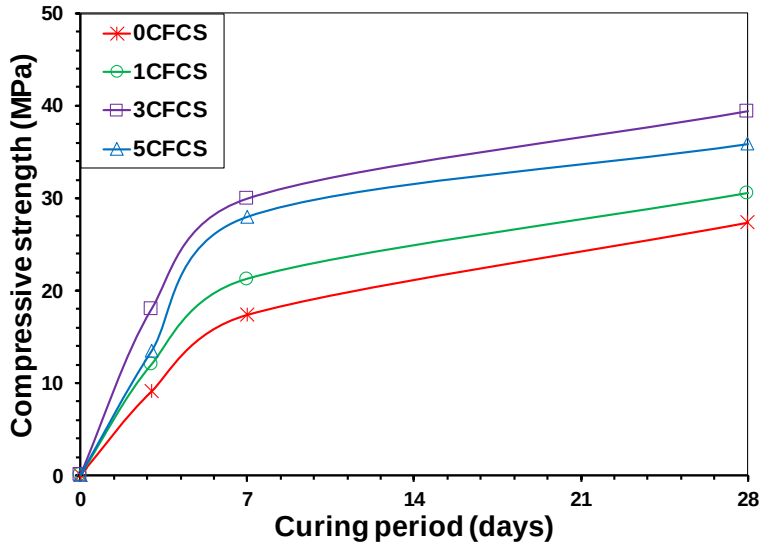

Figure 5.3 Compressive strength results of the hardened paste samples

5.3.2. Mercury intrusion porosimetry (MIP)

The results of the pore structure analysis of the hardened samples are shown in **Figure 5.4** and **Table 5.3**. The total porosity and average pore diameter tended to decrease as the quantity of CF increased at 3 days, and thus, the use of CF clearly induced pore-size refinement [4] in all the samples. However, the average pore diameter of 5CFCS was larger than that of 3CFCS because the 5CFCS sample contained a greater number of large-sized (0.03–0.10 μm) pores, which had newly appeared, compared to the 3CFCS sample (see the shaded area of **Figure 5.4 (a)**). This observation is likely related

to the lower strength of 5CFCS compared to that of 3CFCS at 3 days. Generally, the strength of a solid has an inverse relationship to its total porosity; however, more importantly, the portion of pores larger than 50 nm in the total porosity has a considerably greater influence on the strength than the value of its porosity [25]. Given that, unlike 3CFCS, 5CFCS contained a considerable volume of large pores over 50 nm, the presence of these pores might have lowered the compressive strength of the hardened samples, while 3CFCS hardly showed any pores of this size.

Table 5.3 Total porosities and average pore diameters of hardened samples

Sample label	3 days		28 days	
	Total porosity (%)	Average pore diameter (nm)	Total porosity (%)	Average pore diameter (nm)
0CFCS	36.2	31.4	36.8	17.9
1CFCS	29.9	26.1	34.4	16.5
3CFCS	24.6	17.5	17.3	15.9
5CFCS	21.6	19.9	25.6	11.8

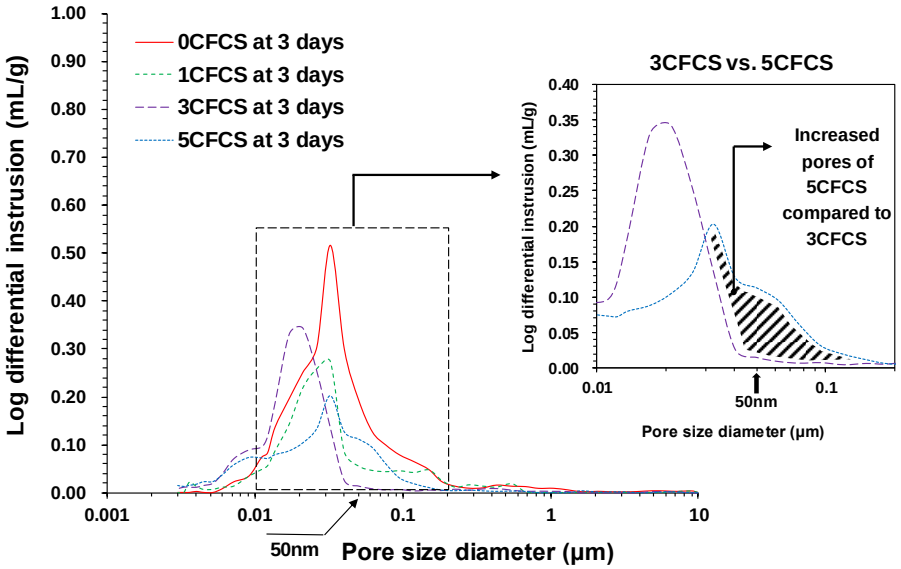

(a)

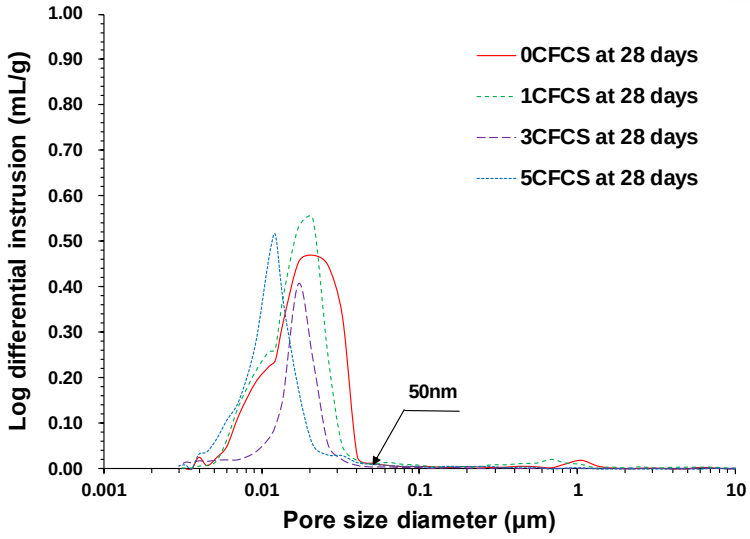

(b)

Figure 5.4 Pore-size distributions of hardened samples: (a) at 3 days and (b) at 28 days

In general, with the progress of curing, the average pore diameter and total porosity of hardened cementitious samples decrease together when their strength increases [42]. In this study, at 28 days, when compared to the 3-day samples, all samples only contained pores smaller than 50 nm (see **Figure 5.4**), and their average pore diameter became smaller (see **Table 5.3**); this indicates that the pore sizes were clearly reduced in all the samples during curing. However, in the samples with CF, except the 3CFCS, the total porosities at 28 days were higher than those of the 3-day samples (see **Table 5.3**). Thus, the use of CF might have the potential to generate nanometer-sized pores, but the sizes of theses pores were mostly smaller than 50 nm. Given that all samples with CF did not show any strength reduction during curing days, the influential degree of the pore formation on the strength seemed not to be significant in this study.

In **Table 5.3**, only in 3CFCS was the total porosity also reduced along with the average pore size from 3 days to 28 days, and thus, as also seen in **Figure 5.4**, there was no indication of nanometer-sized pore generation in 3CFCS during curing days.

At 28 days, the 5CFCS sample showed the smallest value of average pore size among all samples, but its total porosity was higher than that of 3CFCS. In this study, given that the strength of 5CFCS was slightly lower (~9%) than that of 3CFCS at 28 days, the detrimental effect of higher total porosity seemed to be more significant than the advantageous influence of the smaller value of average pore size in determining strength when most pores were smaller than 50 nm.

5.3.3. X-ray diffraction (XRD)

The XRD patterns of the hardened samples with phase analysis are presented in **Figure 5.5**. Calcium silicate hydrate (C-S-H; in the cement notation, C = CaO, S = SiO_2, and H = H_2O), akermanite ($Ca_2Mg(Si_2O_7)$), and hydrotalcite ($MgAl_2CO_3(OH)_{16}\cdot 4(H_2O)$) were found in all samples. Portlandite ($Ca(OH_2)$) was only identified in 0CFCS and 1CFCS. In 3CFCS and 5CFCS, strong XRD peaks of dicalcium aluminate hydrate (C_2AH_8; in the cement notation, A = Al_2O_3) were identified. C_2AH_8 is known as a dominant phase of calcium aluminate cement (CAC) when CAC hydrates over 25°C [101].

At 3 days, the XRD patterns of samples can be divided into two groups; 0CFCS and 1CFCS demonstrated relatively strong peaks of $Ca(OH_2)$ without C_2AH_8, while 3CFCS and 5CFCS showed strong C_2AH_8 peaks but no $Ca(OH_2)$. This suggests that at least more than 3 wt% of CF is necessary to significantly change the types of reaction products for the CaO-activated GGBFS system.

At 28 days, relatively smaller $Ca(OH_2)$ peaks were identified in 0CFCS and 1CFCS, compared to the 3-day patterns, implying that $Ca(OH_2)$ was likely consumed in the pozzolanic reaction to produce C-S-H.

It is well known that C_2AH_8 is one of main reaction products of calcium alumina cement (CAC), and it is a strength-contributing phase [101, 102]. Given that, in XRD, as a greater quantity of CF was substituted, a greater amount of C_2AH_8 was produced, the presence of CF was likely the main cause of the C_2AH_8 generation. Thus, the formation of C_2AH_8 might have contributed to the enhanced strength after the addition of CF at 3 days. However, it is also worth noting that C_2AH_8 is a metastable phase that can easily be converted over time [90, 100, 103-105]; C_2AH_8 in CAC pastes often quickly converts to tricalcium aluminate hydrate (C_3AH_6) and AH gel within a short period (e.g., 28 days [100]), and this conversion accompanies a significant increase in porosity that results in strength reduction [90]. In this study, note that the intensities of C_2AH_8 peaks also decreased in 3CFCS and 5CFCS at 28 days, compared to 3 days, and thus, a portion of C_2AH_8 was removed. Given that a significant increase in total porosities was observed in the samples with CF, except for 3CFCS, from 3 days to 28 days, it is possible that this conversion occurred, although not all the testing results of strength, MIP, and XRD were fully consistent with each other in this regard. However, since C_3AH_6 was not detected in XRD at any days, only AH gel, which is invisible to XRD, could have been generated in this study. More detailed explanation on C_2AH_8 will be given in the TG section.

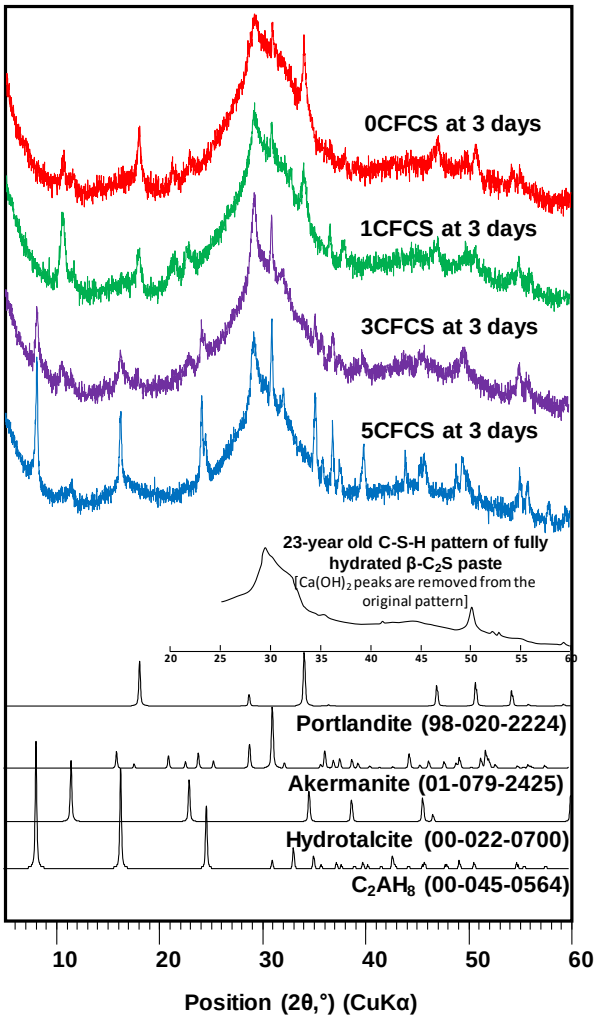

(a)

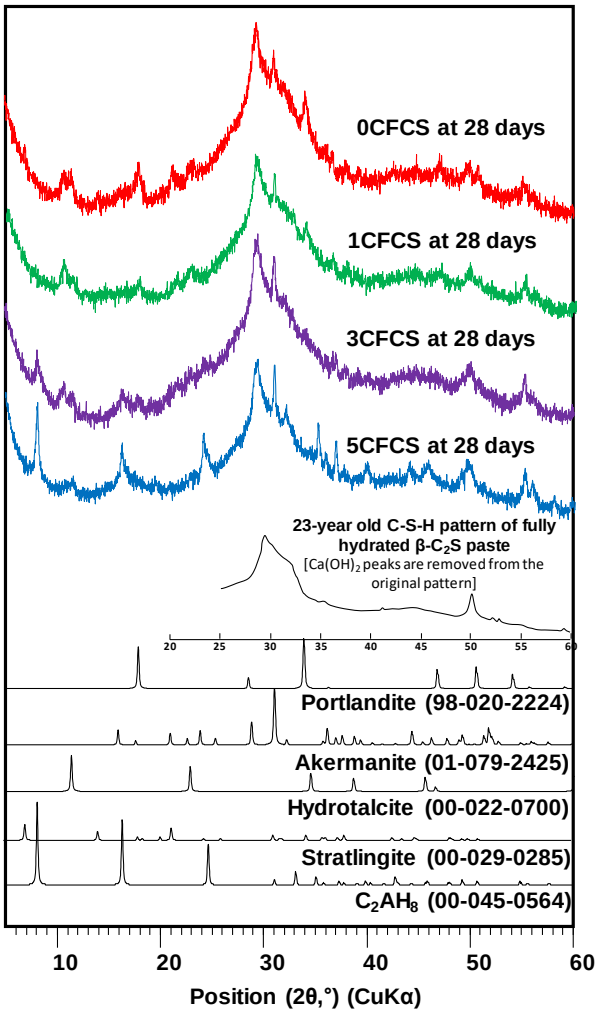

(b)

Figure 5.5 XRD patterns of hardened samples: (a) at 3 days and (b) at 28 days

5.3.4. Thermogravimetry (TG)

The TG results of the hardened samples are shown with a differential form of thermogravimetry (DTG) in **Figure 5.6**. As the CF wt% and curing days increased, the more mass reduction was observed. This indicates that more reaction products were generated and more weight of GGBFS was dissolved because GGBFS was the only source of Si and Al in the formation of the reaction products (e.g., C-S-H, C_2AH_8).

In the literature, there has been a wide variation in the decomposition temperature range of C_2AH_8 in CAC paste [90, 103, 105-107]. However, Ukrainczyk et al. [103] likely presented more accurate values for C_2AH_8 because they synthesized a pure C_2AH_8 and conducted TG along with high temperature XRD. Thus, the DTG peaks in this study were assigned based on the previous studies, but

with more consideration toward the study of Ukrainczyk et al. [103] (see **Figure 5.6)**. In this study, when CF was used, the weight losses of C_2AH_8 occurred near 80°C, 200°C, and 350°C, and that of AH gel appeared around 55°C at all days.

Overall, the TG/DTG results agreed with the XRD analysis. For instance, at 3 days, $Ca(OH_2)$ was clearly identified near 400–430°C in 0CFCS and 1CFCS but was not detected in 3CFCS and 5CFCS, whereas C_2AH_8 was only identified in 3CFCS and 5CFCS. Similar to the XRD results, the quantities of C_2AH_8 in 3CFCS and 5CFCS also tended to be reduced in TG from 3 days to 28 days.

The peak of C_2AH_8 near 80°C overlapped with the peak of C-S-H, making it difficult to be quantitatively analyzed. However, the second peak of C_2AH_8 at ~200°C was independently present. Given that the peak at ~200°C more grew when more CF was used, it was quantitatively confirmed that a greater amount of C_2AH_8 was produced as more quantity of CF was used. Thus, the presence of CF was the main cause for the formation of C_2AH_8.

In 0CFCS and 1CFCS, as there was little (or no) formation of C_2AH_8 in these samples at all days, most weight losses below 200°C were due to the dehydration of C-S-H. Thus, two distinct DTG peaks of C-S-H (i.e., at ~90°C and ~120°C) were identified. At 3 days, given that these C-S-H peaks in 1CFCS were fairly larger than those in 0CFCS at 3 days, the 1 wt% of CF likely induced clearly greater formation of C-S-H at early days (i.e., 3 days); however, at 28 days, this effect of greater formation of C-S-H largely disappeared as these peaks of 0CFCS and 1CFCS became very similar.

At all days, the DTG peaks of C-S-H at ~120°C in 3CFCS and 5CFCS (i.e., samples with more than 3 wt% CF) may appear to have been similar in size to those of 1CFCS. However, as these samples had strong C_2AH_8 peaks at ~80°C that were close to the C-S-H peaks, the C-S-H peaks might have been exaggerated by overlapping with C_2AH_8; thus, these C-S-H peaks were likely smaller than those of 1CFCS. Therefore, the use of CF over 1 wt% did not likely result in further C-S-H formation in this study. However, it should be noted that 3CFCS and 5CFCS generally showed greater strengths than 1CFCS; thus, their greater strengths were likely due to the significant formation of C_2AH_8.

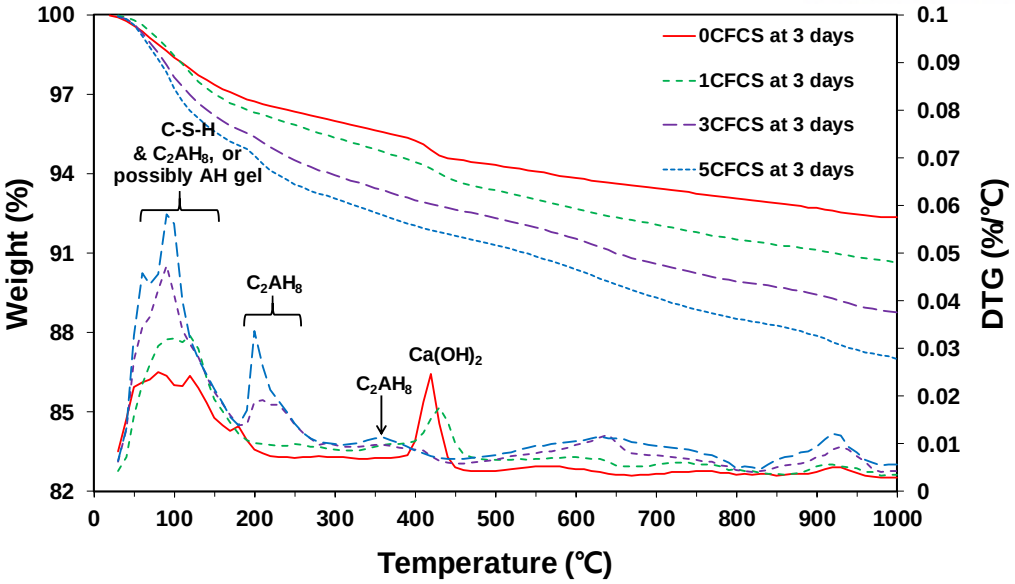

(a)

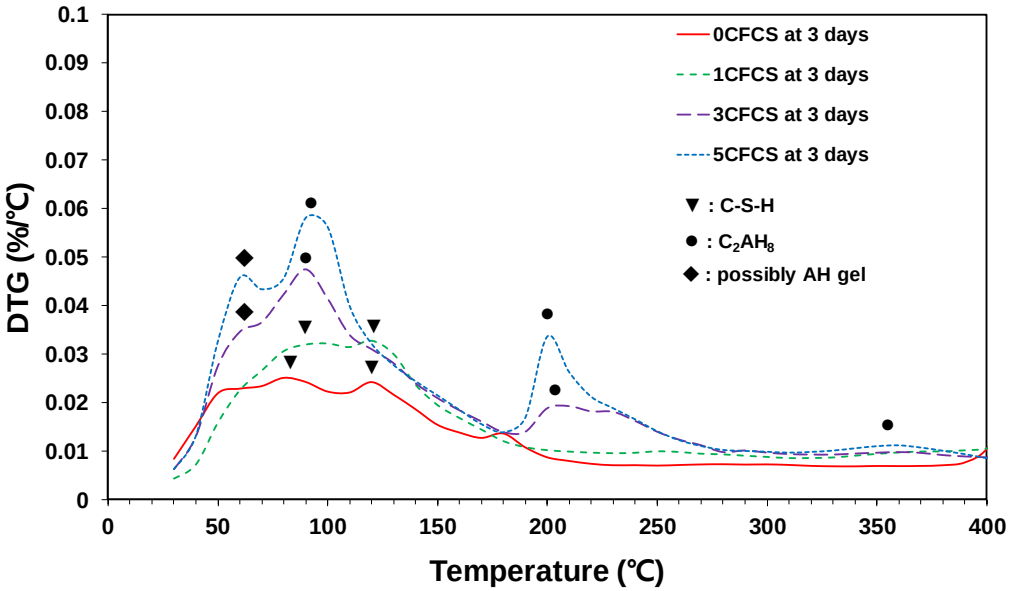

(b)

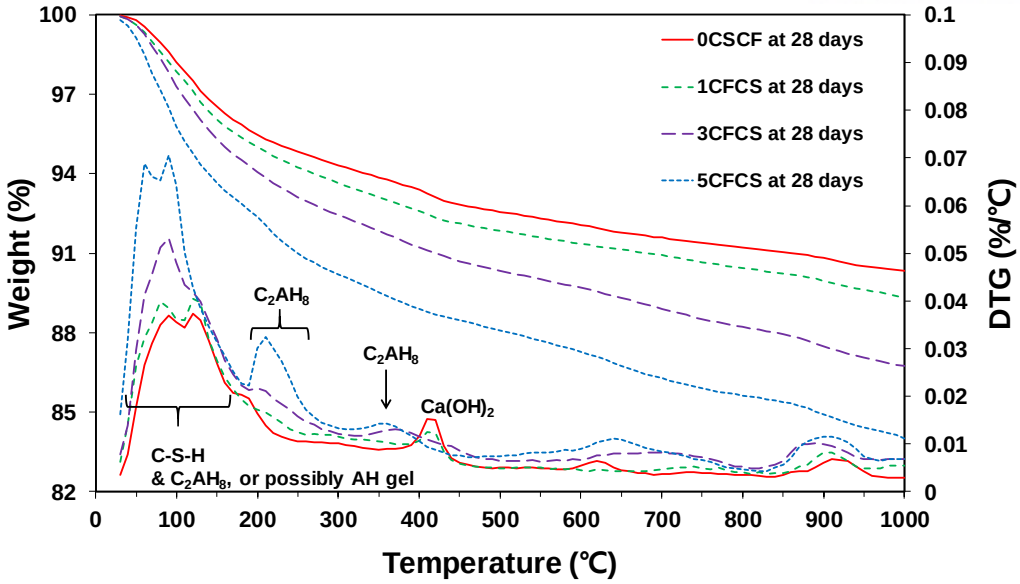

(c)

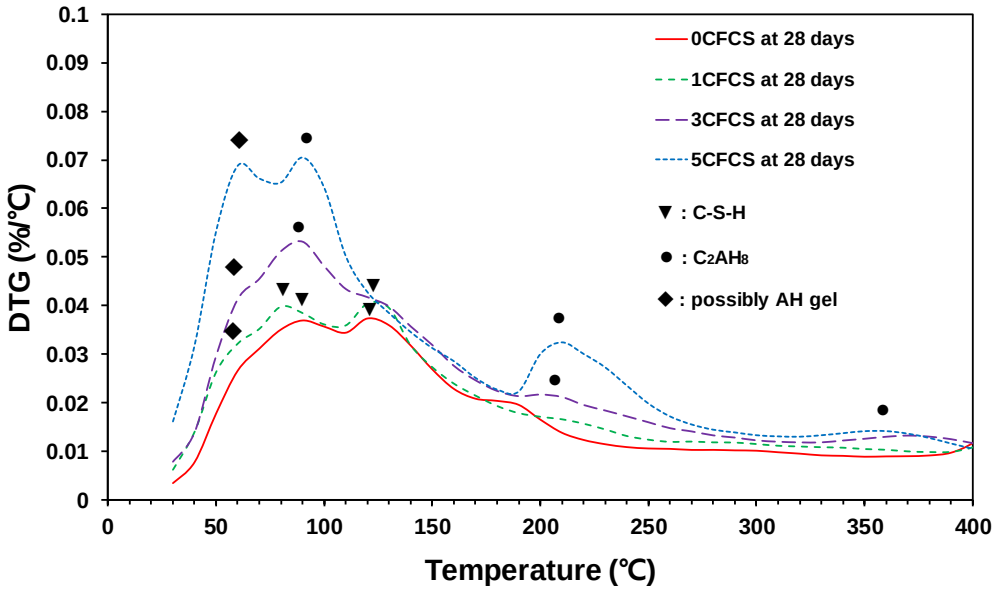

(d)

Figure 5.6 TG/DTG results of hardened samples: (a) 3 days; (b) enlarged view of figure (a) up to 400°C; (c) 28 days; and (d) enlarged view of figure (c) up to 400°C

In **Figure 5.7**, the DTG peaks of AH gel significantly grew in 1CFCS and 5CFCS from 3 days to 28 days, while those in 3CFCS barely increased. Thus, given that the formation of AH gel generally increases porosity and reduces strength in CAC [90, 100, 102], the trend of AH gel formation in the TG

results also seems to be in agreement with the testing results of strength and porosity in this study, as 3CFCS showed the greatest strength with no porosity increase from 3 days to 28 days.

As stated earlier, C_2AH_8 in CAC pastes often converts to C_3AH_6 and AH gel. However, in this study, there was no detection of C_3AH_6 in all samples at 28 days. In particular, in 1CFCS, although C_2AH_8 was hardly detected in XRD and TG at 3 days, an increase of AH gel was clearly observed. Thus, all the experimental results are not fully consistent with each other. However, it should be noted that the samples in this study were not prepared using CAC but were made using the CaO-activation of GGBFS; thus, it is not strange that all the reactions in this study were not exactly the same as the reactions of CAC. Therefore, the formation of AH gel appears to have been due to the conversion of C_2AH_8, which seems to have adversely affected the strength. Nevertheless, although it is still difficult to explain why 3CFCS had the smallest increase in AH gel among the samples from 3 days to 28 days, and further studies are needed on this matter, the smallest increase of 3CFCS in porosity surely helped enhance the strength more than in the other samples.

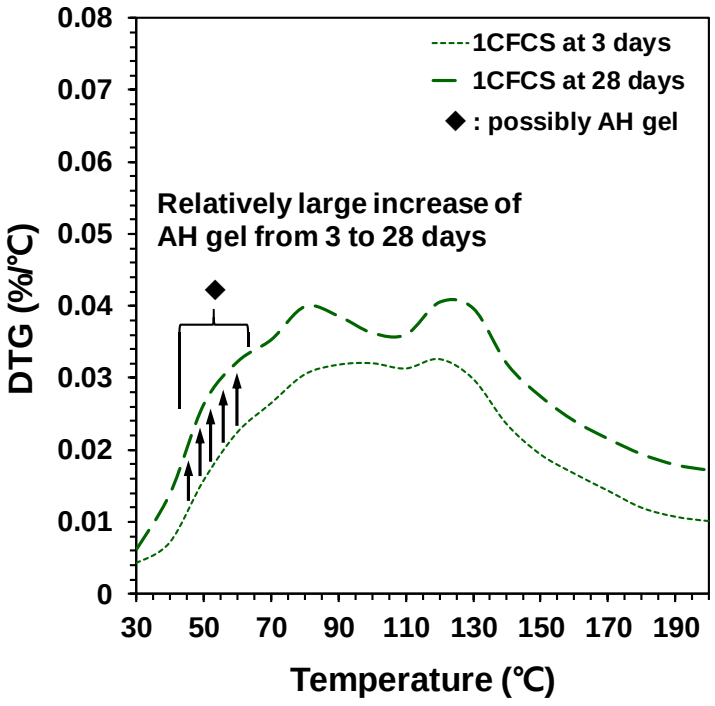

(a)

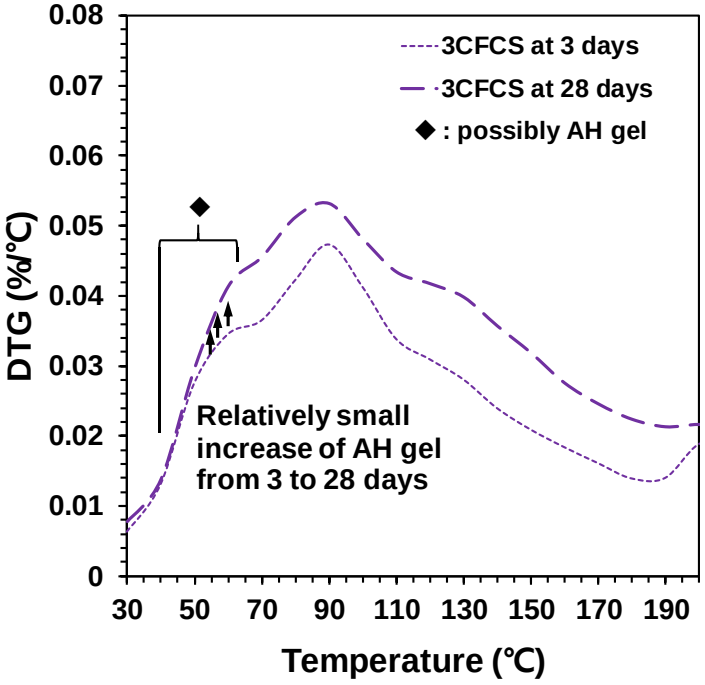

(b)

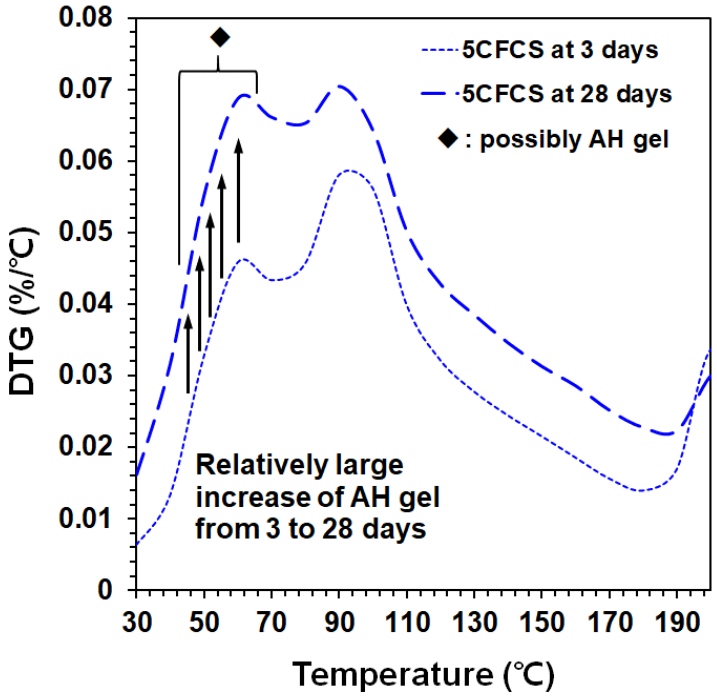

(c)

Figure 5.7 Temporal change of AH gel in DTG from 3 days to 28 days: (a) 1CFCS; (b) 3CFCS; and (c) 5CFCS

5.4. Chapter summary

The present study reported the influence of CF on the CaO-activated GGBFS system regarding strength and reaction products. The presence of CF significantly increased the early and 28-day strengths of CaO-activated GGBFS binder up to 3 wt% addition; however, the use of 5 wt% produced rather lower strengths than those of 3 wt%.

The main causes for the increase in strength due to the use of CF are summarized as follows: (1) more dissolution of GGBFS, (2) more C-S-H formation, and most importantly, (3) an increase in C_2AH_8 formation. However, when the amount of CF was used over a certain limit (e.g., 3 wt%, in this study), the formation of C-S-H began to be disturbed, although more C_2AH_8 was formed.

In this study, although the greater formation of C_2AH_8 was the main cause of the strength enhancement, the C_2AH_8 phase was metastable and likely converted to AH gel, resulting in the effect of the porosity increase and strength reduction. Thus, as the amount of CF increased, the C_2AH_8 formation's strength increasing effect and the C_2AH_8 conversion's strength reducing effect offset each other; when the former was more dominant, the strength was enhanced (e.g., up to 3 wt% of CF), but when the latter was larger, the strength enhancement decreased (e.g., at 5 wt% of CF).

6. SUMMARY

Mechanical and microstructural characteristics of various types of CaO-activated cementless binders were investigated using various experimental method.

To investigate the effect of $CaCl_2$ on CaO-activated GGBFS/fly ash binder, various amounts of $CaCl_2$ were incorporated. The samples with $CaCl_2$ generated much higher compressive strength than the sample without $CaCl_2$ at all curing period. In terms of compressive strength, substitution of 2wt% $CaCl_2$ was considered to be the best mixture proportion. Interestingly, despite having no cement compound in this binder, $CaCl_2$ had a very similar acceleration effect on the cementless binder.

The reactions of binders generated significantly lower cumulative heats up to 72 h, although their initial heats up to 10 h were notably higher, compared to the cumulative and initial heats of Portland cement hydration. These high initial heats of binder might be advantageous in dissolving raw materials.

XRD and TG/DTG results showed that the amorphous phase of the raw material was dissolved more by the addition of $CaCl_2$, and which seemed to generate more quantity of reaction product, resulting in the denser cementitious matrix. The most distinct mineralogical changes due to $CaCl_2$ addition were the formation of hydrocalumite and the removal of hydrotalcite and strätlingite.

From MIP results, the addition of $CaCl_2$ induced pore-size refinement effect from the early stage of curing. In addition overall total porosity was reduced as more amount of $CaCl_2$ substituted, resulting in higher early and final compressive strength.

In the BSE images, the particle size of raw materials became smaller as $CaCl_2$ was replaced, which seems to be due to the $CaCl_2$ dissolving raw materials actively. As a result of EDS analysis, much higher Ca/Al and Na/Al ratios were measured as $CaCl_2$ was added, which indicates that Ca and Na ions were produced more by dissolving the raw materials.

As mentioned earlier, $CaCl_2$ is used as an accelerator in Portland cement. However, the used of $CaCl_2$ can cause the steel corrosion, ACI regulated the maximum dosage of $CaCl_2$ varying with the structures. Therefore, in this study, the electrical resistivity of the binder was measured using four Wenner method to verify the possibility of steel corrosion. The higher electrical resistivity was measured as $CaCl_2$ was added, which indicates that the possibility of corrosion of the steel bar is low even with the addition of $CaCl_2$. The reason for this result seems to be that a denser matrix was generated as $CaCl_2$ was added.

When $CaCl_2$ was applied to CaO-activated GGBFS/fly ash binder, satisfactory levels of mechanical properties were measured, but further experiment is required for commercialization due to concerns about steel corrosion. Therefore, other types of accelerator such as $Ca(NO_3)_2$ and $NANO_3$ was applied to CaO- activated GGBFS binder.

In the compressive strength, the addition of each nitrate salt ($Ca(NO_3)_2$ and $NaNO_3$) was clearly beneficial in developing strength during the early days of curing. The results showed that on day

3 of curing, the strengths were almost doubled for all samples, regardless of the cation type of the nitrate salts. However, a difference between the nitrate salts was seen on day 28 of curing, where the added $Ca(NO_3)_2$ was still effective in increasing the cementless binder's strength compared to the control (without any nitrate salts), the added $NaNO_3$ was not anymore.

A pH meter measurement was conducted to verify the cation effect of each nitrate salts. In the presence of $NaNO_3$, which generally increases the solubility of $Ca(OH)_2$ in aqueous salt solutions, the higher pH of $NaNO_3$ containing samples was obtained due to the increased amount of dissolving the $Ca(OH)_2$. These higher pH seems to generate more reaction products and higher early strength measurements. In the samples with $Ca(NO_3)_2$, an additional supply Ca ion from $Ca(NO_3)_2$ resulted in a common ion effect, which seems to have a relatively low pH measured by lowering the solubility of $Ca(OH)_2$. Although a lower pH was measured, higher compressive strength seem to be measured due to the supply of stable Ca ions.

The type of reaction products analyzed with the XRD was very similar between the $Ca(NO_3)_2$ and $NaNO_3$ group when the same weight of salts was used, although their compressive strength were significantly different. C-S-H and akermanite were identified in all samples. An Al_2O_3-Fe_2O_3-mono (AFm) phase was clearly identified in the samples containing any type of nitrate salts with more than 3wt%. This seemed to occur mainly when the quantity of salts was at 5wt%, causing the XRD peaks of this phase to increase significantly. AFm phase in our study was nitrate AFm or nitrite AFm or a mixture of NO_3-and NO_2 AFm phases. In the samples with $Ca(NO_3)_2$, weaker peaks of portlandite were identified and portlandite was not identified in the $3Ca(NO_3)_2$ and $5Ca(NO_3)_2$ samples. However, portlandite was clearly identified in the samples with $NaNO_3$.

The more amount of nitrate salts were substituted, the more total weight loss until 1,000C occurred. This weight loss indirectly suggests that more nitrates salts resulted in more GGBFS due to an increase of it dissolving. Overall TG results were consistent with XRD results. At 3 days of curing, the use of nitrate salts was clearly beneficial to produce C-S-H, regardless of the cation type in the salts. However, at 28 days of curing, the samples with $NANO_3$ clearly displayed a reduction of C-S-H when weight of the salt increased. The NO_3-and/or NO_2-AFm phase were significantly generated when nitrate salts replaced 3-5wt of the total mixture weight.

The pore size distribution was significantly dependent on the cation type of nitrate salts. The shape of the distribution curves of the samples with $Ca(NO_3)_2$ were roughly grouped in two curve shapes depending on the quantity of $Ca(NO_3)_2$, while those of the $NaNO_3$ samples were not significantly changed by the dosage of $NaNO_3$.

In order to develop a cementless binder with satisfactory mechanical properties without concern about steel corrosion, calcium formate ($Ca(HCOO_2)$) was applied as an auxiliary activator to CaO-activated GGBFS binder and its effect was verified using various experiments.

The addition of $Ca(HCOO_2)$, such as $CaCl_2$, $Ca(NO_3)_2$, and $NaNO_3$, acted as an accelerator and 1.3-2 times higher compressive strength was measured at 3 days of curing and 1.1-1.4 times higher compressive strength measured at 28 days of curing compared to samples without $Ca(HCOO_2)$. The extent of $Ca(HCOO_2)$`s strength enhancement was comparable to that of samples with $CaCl_2$. The highest compressive strength was achieved at 3wt% of $Ca(HCOO_2)$.

As a result of MIP measurement, the pore-size refinement effect occurred as $Ca(HCOO_2)$ was replaced, and which seemed to be the main reason of increasing the compressive strength of the binder. Interestingly, in all other samples except samples with 3wt% $Ca(HCOO_2)$, a greater amount of total porosity was measured at 28 days compared to 3 days, suggesting the possibility of nanometer-sized pores. However, all samples with $Ca(HCOO_2)$ did not show any strength reduction during curing days, the influential degree of the pore formation on the strength seemed not to be significant in this study.

The XRD patterns of samples can be divided into two groups; samples with 0-1wt% $Ca(HCOO_2)$ demonstrated relatively strong peaks of $Ca(OH)_2$ without C_2AH_8, while samples with 3-5wt% CF showed strength C_2AH_7 peaks but no $Ca(OH)_2$. This suggests that at least more than 3wt% of $Ca(HCOO_2)$ is necessary to significantly change the types of reaction products for the CaO-activated GGBFS system. C_2AH_8 is one of main reaction products of calcium alumina cement, and it is strength-contribution phase. As a greater quantity of $Ca(HCOO_2)$ was substituted, a greater amount of C_2AH_8 was produced, the presence of $Ca(HCOO_2)$ was likely the main cause of the C_2AH_8 generation. Thus, the formation of C_2AH_8 might have contributed to the enhanced strength. However, it is well known that C_2AH_8 is a metastable phase that can easily converted over time, and this conversion accompanies a significantly increase in porosity that results in strength reduction. In this study, the intensities of C_2AH_8 peaks also decreased at 28 days, compared to 3 days, and thus a portion of C_2AH_8 was removed.

In the TG/DTG results, as the $Ca(HCOO_2)$ wt% and curing days increased, the more mass reduction was observed. This indicates that more reaction products were generated and more weight of GGBFS was dissolved because GGBFS was the only source of Si and Al in the formation of the reaction products (e.g., C-S-H, C_2AH_8). The second peaks of C_2AH_8 at ~200°C showed that more amount of $Ca(HCOO_2)$ replacement generated more amount of C_2AH_8. The DTG peaks of AH gel significantly grew in 1 and 5wt% contained samples from 3 days to 28 days, while those in 3wt% contained sample barely increased. The formation of AH gel generally increases porosity and reduces strength in calcium alumina cement, the trend of AH gel formation in the TG results also seems to be in agreement with the testing results of strength and porosity in this study.

Through this study, the influence of various auxiliary chemical activators on CaO-activated cementless binders were investigated. Depending on the auxiliary chemical activators, the effect of mechanical and microstructural characteristics were varies. To apply the developed binders on actual construction site, further research such as mechanical properties of cementless concrete and durability tests will be conducted.

REFERENCES

1. Maddalena, R., J.J. Roberts, and A. Hamilton, *Can Portland cement be replaced by low-carbon alternative materials? A study on the thermal properties and carbon emissions of innovative cements.* Journal of Cleaner Production, 2018. **186**: p. 933-942.
2. Team, C.W., *Climate change 2014: synthesis report*. 2014, IPCC Geneva, Switzerland. p. 151.
3. IPCC, *Climate change: The IPCC scientific assessment*. 1990, Australian Government Publishing Service Caniberra, Australia.
4. Mehta, P.K. and P.J. Monteiro, *CONCRETE Microstructure, Properties and Materials*. 2017.
5. Rubin, E. and H. De Coninck, *IPCC special report on carbon dioxide capture and storage.* UK: Cambridge University Press. TNO (2004): Cost Curves for CO2 Storage, Part, 2005. **2**.
6. Pera, J. and J. Ambroise, *New applications of calcium sulfoaluminate cement.* Cement and concrete research, 2004. **34**(4): p. 671-676.
7. Sharp, J., C. Lawrence, and R. Yang, *Calcium sulfoaluminate cements—low-energy cements, special cements or what?* Advances in Cement Research, 1999. **11**(1): p. 3-13.
8. da Costa, E.B., et al., *Production and hydration of calcium sulfoaluminate-belite cements derived from aluminium anodising sludge.* Construction and Building Materials, 2016. **122**: p. 373-383.
9. Quillin, K., *Performance of belite–sulfoaluminate cements.* Cement and Concrete Research, 2001. **31**(9): p. 1341-1349.
10. Gartner, E., *CSA and belite-rich clinkers and cements.*
11. Chen, I.A. and M.C. Juenger, *Synthesis and hydration of calcium sulfoaluminate-belite cements with varied phase compositions.* Journal of Materials Science, 2011. **46**(8): p. 2568-2577.
12. Bullerjahn, F., D. Schmitt, and M.B. Haha, *Effect of raw mix design and of clinkering process on the formation and mineralogical composition of (ternesite) belite calcium sulphoaluminate ferrite clinker.* Cement and concrete research, 2014. **59**: p. 87-95.
13. Davidovits, J. *Properties of geopolymer cements*. in *First international conference on alkaline cements and concretes*. 1994. Scientific Research Institute on Binders and Materials Kiev State Technical University, Ukraine.
14. Wang, S.-D., et al., *Alkali-activated slag cement and concrete: a review of properties and problems.* Advances in cement research, 1995. **7**(27): p. 93-102.
15. Shi, C., D. Roy, and P. Krivenko, *Alkali-activated cements and concretes*. 2003: CRC press.
16. Kim, M.S., et al., *Use of CaO as an activator for producing a price-competitive non-cement structural binder using ground granulated blast furnace slag.* Cement and Concrete Research, 2013. **54**: p. 208-214.
17. Aligizaki, K.K., *Pore structure of cement-based materials: testing, interpretation and requirements*. 2014: CRC Press.
18. Powers, T.C. and T.L. Brownyard. *Studies of the physical properties of hardened Portland cement paste*. in *Journal Proceedings*. 1946.
19. Copeland, L.E. and J.C. Hayes, *The determination of non-evaporable water in hardened portland cement paste*. 1953.
20. Day, R.L. and B.K. Marsh, *Measurement of porosity in blended cement pastes.* Cement and Concrete Research, 1988. **18**(1): p. 63-73.
21. Zhang, J. and G.W. Scherer, *Comparison of methods for arresting hydration of cement.* Cement and Concrete Research, 2011. **41**(10): p. 1024-1036.
22. Gallé, C., *Effect of drying on cement-based materials pore structure as identified by mercury intrusion porosimetry: a comparative study between oven-, vacuum-, and freeze-drying.* Cement and Concrete Research, 2001. **31**(10): p. 1467-1477.

23. Detwiler, R.J., et al., *Preparing specimens for microscopy.* Concrete International, 2001. **23**(11): p. 50-58.
24. Zhang, L. and F. Glasser, *Critical examination of drying damage to cement pastes.* Advances in cement research, 2000. **12**(2): p. 79-88.
25. Gran, H.C. and E.W. Hansen, *Exchange rates of ethanol with water in water-saturated cement pastes probed by NMR.* Advanced Cement Based Materials, 1998. **8**(3-4): p. 108-117.
26. Beaudoin, J.J., et al., *Solvent exchange in partially saturated and saturated microporous systems: length change anomalies.* Cement and concrete research, 2000. **30**(3): p. 359-370.
27. Song, H., et al., *A study of thermal decomposition of phases in cementitious systems using HT-XRD and TG.* Construction and Building Materials, 2018. **169**: p. 648-661.
28. Sha, W. and G. Pereira, *Differential scanning calorimetry study of hydrated ground granulated blast-furnace slag.* Cement and concrete research, 2001. **31**(2): p. 327-329.
29. Bakolas, A., et al., *Evaluation of pozzolanic activity and physicomechanical characteristics in metakaolin-lime pastes.* Journal of Thermal Analysis and Calorimetry, 2006. **84**(1): p. 157-163.
30. Haha, M.B., et al., *Influence of activator type on hydration kinetics, hydrate assemblage and microstructural development of alkali activated blast-furnace slags.* Cement and Concrete Research, 2011. **41**(3): p. 301-310.
31. Wang, S.-D. and K.L. Scrivener, *Hydration products of alkali activated slag cement.* Cement and Concrete Research, 1995. **25**(3): p. 561-571.
32. Taylor, H., *W.(1997). Cement chemistry*. 1997, Thomas Telford.
33. Q. Yu, H.B., H,, *Gypsum: an investigation of microstcuture and mechanical properties, in: Proceedings 8th fib International PhD Symposium in Civil Enginerring*. 2010.
34. Vassileva, C.G. and S.V. Vassilev, *Behaviour of inorganic matter during heating of Bulgarian coals: 1. Lignites.* Fuel Processing Technology, 2005. **86**(12-13): p. 1297-1333.
35. Schöler, A., et al., *Hydration of quaternary Portland cement blends containing blast-furnace slag, siliceous fly ash and limestone powder.* Cement and Concrete Composites, 2015. **55**: p. 374-382.
36. Jeon, D., et al., *Microstructural and strength improvements through the use of Na2CO3 in a cementless Ca (OH) 2-activated Class F fly ash system.* Cement and Concrete Research, 2015. **67**: p. 215-225.
37. Alahrache, S., et al., *Chemical activation of hybrid binders based on siliceous fly ash and Portland cement.* Cement and Concrete Composites, 2016. **66**: p. 10-23.
38. Murat, M., *Hydration reaction and hardening of calcined clays and related minerals. I. Preliminary investigation on metakaolinite.* Cement and Concrete Research, 1983. **13**(2): p. 259-266.
39. Scrivener, K., R. Snellings, and B. Lothenbach, *A practical guide to microstructural analysis of cementitious materials*. 2016: Crc Press.
40. Committee, A., *Admixtures for concrete.* American Concrete Inst. ACI, 1986.
41. ACI, *Building code requirements for reinforced concrete*. 2014.
42. Layssi, H., et al., *Electrical resistivity of concrete.* Concrete International, 2015. **37**(5): p. 41-46.
43. Liu, W., J. Yang, and B. Xiao, *Review on treatment and utilization of bauxite residues in China.* International Journal of Mineral Processing, 2009. **93**(3-4): p. 220-231.
44. Malhotra, V., *Introduction: sustainable development and concrete technology.* Concrete International, 2002. **24**(7).
45. Arora, A., G. Sant, and N. Neithalath, *Ternary blends containing slag and interground/blended limestone: Hydration, strength, and pore structure.* Construction and Building Materials, 2016. **102**: p. 113-124.
46. Pacheco-Torgal, F., *Introduction to handbook of alkali-activated cements, mortars and concretes*, in *Handbook of alkali-activated cements, mortars and concretes*. 2015, Elsevier. p. 1-16.

47. Bellmann, F. and J. Stark, *Activation of blast furnace slag by a new method.* Cement and Concrete Research, 2009. **39**(8): p. 644-650.
48. Lee, S.-J., *The Kwang Ahn Bridges, Pusan.* Structural engineering international, 2001. **11**(1): p. 23-24.
49. Jeong, Y., et al., *Microstructural verification of the strength performance of ternary blended cement systems with high volumes of fly ash and GGBFS.* Construction and Building Materials, 2015. **95**: p. 96-107.
50. Lee, N.K., et al., *Alkali-activated, cementless, controlled low-strength materials (CLSM) utilizing industrial by-products.* Construction and Building Materials, 2013. **49**: p. 738-746.
51. Aldea, C.-M., et al., *Effects of curing conditions on properties of concrete using slag replacement.* Cement and Concrete Research, 2000. **30**(3): p. 465-472.
52. Shi, C. and R.L. Day, *Chemical activation of lime-slag blends.* Special Publication, 1995. **153**: p. 1165-1178.
53. Shi, C., *Pozzolanic reaction and microstructure of chemical activated lime-fly ash pastes.* Materials Journal, 1998. **95**(5): p. 537-545.
54. Shi, C. and R.L. Day, *Acceleration of the reactivity of fly ash by chemical activation.* Cement and Concrete Research, 1995. **25**(1): p. 15-21.
55. Shi, C. and R.L. Day, *Pozzolanic reaction in the presence of chemical activators: Part I. Reaction kinetics.* Cement and Concrete Research, 2000. **30**(1): p. 51-58.
56. Shi, C. and R.L. Day, *Pozzolanic reaction in the presence of chemical activators: Part II—Reaction products and mechanism.* Cement and Concrete Research, 2000. **30**(4): p. 607-613.
57. PANalytical, B., *'Pert HighScore Plus software, version 3.0 e.* Almelo: Netherlands, 2012.
58. ICDD, *PDF-2 Database Sets*. 2007.
59. Allmann, R. and R. Hinek, *The introduction of structure types into the Inorganic Crystal Structure Database ICSD.* Acta Crystallographica Section A: Foundations of Crystallography, 2007. **63**(5): p. 412-417.
60. Polder, R.B., *Test methods for on site measurement of resistivity of concrete—a RILEM TC-154 technical recommendation.* Construction and building materials, 2001. **15**(2-3): p. 125-131.
61. KS, A., *KS L ISO 670 Methods of Testing Cements-Determination of Strength*. 2006.
62. Chen, C.-T., J.-J. Chang, and W.-c. Yeih, *The effects of specimen parameters on the resistivity of concrete.* Construction and Building Materials, 2014. **71**: p. 35-43.
63. Rapp, P. *Effect of calcium chloride on Portland cements and concretes*. in *Proceedings*. 1935.
64. Lea, F., *The Chemistry of Cement and Concrete. 3rd edn, E.* Arnold, London, 1970.
65. Rosenberg, A.M. *Study of the mechanism through which calcium chloride accelerates the set of portland cement*. in *Journal Proceedings*. 1964.
66. Ramachandran, V.S., *Possible states of chloride in the hydration of tricalcium silicate in the presence of calcium chloride.* Matériaux et Construction, 1971. **4**(1): p. 3-12.
67. Shi, C. and R.L. Day, *Chemical activation of blended cements made with lime and natural pozzolans.* Cement and Concrete Research, 1993. **23**(6): p. 1389-1396.
68. Kolani, B., et al., *Hydration of slag-blended cements.* Cement and Concrete Composites, 2012. **34**(9): p. 1009-1018.
69. Park, H., et al., *Strength development and hydration behavior of self-activation of commercial ground granulated blast-furnace slag mixed with purified water.* Materials, 2016. **9**(3): p. 185.
70. Wei, Y., et al., *Quantitative evaluation of hydrated cement modified by silica fume using QXRD, 27Al MAS NMR, TG–DSC and selective dissolution techniques.* Construction and Building Materials, 2012. **36**: p. 925-932.
71. Vieille, L., et al., *Hydrocalumite and its polymer derivatives. 1. Reversible thermal behavior of Friedel's salt: a direct observation by means of high-temperature in situ powder X-ray diffraction.* Chemistry of materials, 2003. **15**(23): p. 4361-4368.
72. Jeong, Y., et al., *Strength development and microstructural characteristics of barium hydroxide-activated ground granulated blast furnace slag.* Cement and Concrete Composites, 2017. **79**: p. 34-44.

73. Park, H., et al., *Strength enhancement and pore-size refinement in clinker-free CaO-activated GGBFS systems through substitution with gypsum.* Cement and Concrete Composites, 2016. **68**: p. 57-65.
74. Jiang, W., *Alkali-activated cementitious materials: mechanisms, microstructure and properties*. 1997.
75. Bakharev, T., J.G. Sanjayan, and Y.-B. Cheng, *Alkali activation of Australian slag cements.* Cement and Concrete Research, 1999. **29**(1): p. 113-120.
76. Li, D., et al., *The influence of alkalinity on activation and microstructure of fly ash.* Cement and Concrete Research, 2000. **30**(6): p. 881-886.
77. Alonso, S. and A. Palomo, *Alkaline activation of metakaolin and calcium hydroxide mixtures: influence of temperature, activator concentration and solids ratio.* Materials Letters, 2001. **47**(1-2): p. 55-62.
78. Altan, E. and S.T. Erdoğan, *Alkali activation of a slag at ambient and elevated temperatures.* Cement and Concrete Composites, 2012. **34**(2): p. 131-139.
79. Ravikumar, D. and N. Neithalath, *Effects of activator characteristics on the reaction product formation in slag binders activated using alkali silicate powder and NaOH.* Cement and Concrete Composites, 2012. **34**(7): p. 809-818.
80. Yang, K.-H., et al., *Hydration products and strength development of calcium hydroxide-based alkali-activated slag mortars.* construction and Building Materials, 2012. **29**: p. 410-419.
81. Yum, W.S., et al., *Effects of CaCl2 on hydration and properties of lime (CaO)-activated slag/fly ash binder.* Cement and Concrete Composites, 2017. **84**: p. 111-123.
82. Adamu, M., L.E. Umoru, and O.O. Ige, *Effect of Calcium Nitrate and Sodium Nitrite on the Rebar Corrosion of Medium Carbon Steel in Seawater and Cassava Fluid.* Journal of Minerals and Materials Characterization and Engineering, 2014. **2**(3): p. 223-229.
83. Paillère, A.-M., *Application of admixtures in concrete*. Vol. 10. 1994: CRC Press.
84. ASTM, C., *305, Standard Practice for Mechanical Mixing of Hydraulic Cement Pastes and Mortars of Plastic Consistency.* ASTM International, 1999.
85. Belsky, A., et al., *New developments in the Inorganic Crystal Structure Database (ICSD): accessibility in support of materials research and design.* Acta Crystallographica Section B: Structural Science, 2002. **58**(3): p. 364-369.
86. Justnes, H. and E.C. Nygaard, *Technical calcium nitrate as set accelerator for cement at low temperatures.* Cement and Concrete Research, 1995. **25**(8): p. 1766-1774.
87. Song, S. and H.M. Jennings, *Pore solution chemistry of alkali-activated ground granulated blast-furnace slag1.* Cement and Concrete Research, 1999. **29**(2): p. 159-170.
88. Johnston, J. and C. Grove, *The solubility of calcium hydroxide in aqueous salt solutions.* Journal of the American Chemical Society, 1931. **53**(11): p. 3976-3991.
89. Oxtoby, D.W., H.P. Gillis, and L.J. Butler, *Principles of modern chemistry*. 2015: Cengage learning.
90. Taylor, H.F., *Cement chemistry*. 1997: Thomas Telford.
91. Gu, K., et al., *Mechanical and hydration properties of ground granulated blastfurnace slag pastes activated with MgO–CaO mixtures.* Construction and Building Materials, 2014. **69**: p. 101-108.
92. Burciaga-Díaz, O. and I. Betancourt-Castillo, *Characterization of novel blast-furnace slag cement pastes and mortars activated with a reactive mixture of MgO-NaOH.* Cement and Concrete Research, 2018. **105**: p. 54-63.
93. Renaudin, G. and M. Francois, *The lamellar double-hydroxide (LDH) compound with composition 3CaO. Al2O3. Ca (NO3) 2.10 H2O.* Acta Crystallographica Section C, 1999. **55**(6): p. 835-838.
94. Balonis, M., M. Medala, and F.P. Glasser, *Influence of calcium nitrate and nitrite on the constitution of AFm and AFt cement hydrates.* Advances in Cement research, 2011. **23**(3): p. 129-143.

95. Renaudin, G., et al., *Thermal behaviour of the nitrated AFm phase Ca4Al2 (OH) 12 (NO3) 2• 4H2O and structure determination of the intermediate hydrate Ca4Al2 (OH) 12 (NO3) 2• 2H2O.* Cement and Concrete Research, 2000. **30**(2): p. 307-314.
96. Mohan, K. and H. Taylor, *Analytical Electron Microscopy of Cement Pastes: IV, β-Dicalcium Silicate Pastes.* Journal of the American Ceramic Society, 1981. **64**(12): p. 717-719.
97. Osborne, G., *Durability of Portland blast-furnace slag cement concrete.* Cement and Concrete Composites, 1999. **21**(1): p. 11-21.
98. Brough, A. and A. Atkinson, *Sodium silicate-based, alkali-activated slag mortars: Part I. Strength, hydration and microstructure.* Cement and concrete research, 2002. **32**(6): p. 865-879.
99. Jeong, Y., et al., *Influence of slag characteristics on strength development and reaction products in a CaO-activated slag system.* Cement and Concrete Composites, 2016. **72**: p. 155-167.
100. Neville, A.M., *Properties of concrete*. Vol. 4. 1995: Longman London.
101. Bensted, J., *Calcium aluminate cements.* Structure and performance of cements, 2002. **2**: p. 114-138.
102. Barnes, P. and J. Bensted, *Structure and performance of cements*. 2014: CRC Press.
103. Ukrainczyk, N., et al., *Dehydration of a layered double hydroxide—C2AH8.* Thermochimica Acta, 2007. **464**(1-2): p. 7-15.
104. Jensen, T.R., A.N. Christensen, and J.C. Hanson, *Hydrothermal transformation of the calcium aluminum oxide hydrates CaAl2O4· 10H2O and Ca2Al2O5· 8H2O to Ca3Al2 (OH) 12 investigated by in situ synchrotron X-ray powder diffraction.* Cement and concrete research, 2005. **35**(12): p. 2300-2309.
105. Gosselin, C. and K. Scrivener. *Microstructure development of calcium aluminate cements accelerated by lithium sulphate*. in *Calcium Aluminate Cements Proceeding of the Centenary Conference*. 2008.
106. Cardoso, F.A., et al., *Effect of curing time on the properties of CAC bonded refractory castables.* Journal of the European Ceramic Society, 2004. **24**(7): p. 2073-2078.
107. Luz, A. and V. Pandolfelli, *Halting the calcium aluminate cement hydration process.* Ceramics International, 2011. **37**(8): p. 3789-3793.